A STUDY OF THE DISPROPORTIONATION OF CARBON MONOXIDE ON ALUMINA

by

Lawrence J. Samson

B. S., Kansas State University, 1982

A MASTER'S THESIS

Submitted in partial fulfillment of the

requirements for the degree

MASTER OF SCIENCE

Department of Chemical Engineering

KANSAS STATE UNIVERSITY
Manhattan, Kansas

1985

Approved by

John C. Matthews
Major Professor

TABLE OF CONTENTS

LIST OF FIGURES

LIST OF TABLES

CHAPTER 1

INTRODUCTION

Alumina has been used extensively for adsorbents, active catalysts, and catalyst supports for many years. As early as 1797, Dutch chemists discovered that alumina catalyzed the dehydration of ethanol to ether. Since that time, the applications of alumina have increased many fold with a recent annual production of high surface area alumina of over 50 million pounds (1). In industrial catalytic processes aluminas are used mostly as supports for oxides, mixed oxides and transition metals. One of the most important and widespread uses for alumina is the support of noble metals in catalytic reforming of petroleum. Alumina alone has been found to catalyze several reactions, some of which are listed in Table 1.1. These reactions show that alumina is able to activate hydrogen-hydrogen, carbon-carbon, and carbon-hydrogen bonds but with varying efficiencies.

Alumina has been found to exist in many different structures and hydration states, each with different properties. A schematic representation showing how all of the different phases of alumina are related can be seen in Figure 1.1. The most common phases used for catalyst and catalyst supports are eta and gamma. In this work, eta and gamma alumina were found to convert carbon monoxide to carbon dioxide at temperatures from 450 to 700°C. The overall stoichiometry of the reaction is believed to be

Table 1.1

Reactions Catalyzed by Aluminas (2)

Reaction	Temperature (K)
o-H_2 → p-H_2	78
H_2 + D_2 → 2HD	150
CH_4/CD_4 isotopic scrambling	300
Alkene + D_2 → Alkene-D + HD	300
Benzene + D_2 → Benzene-D + HD	300
Double-bond isomerization of alkenes	300
Cis/trans isomerization of alkenes	300
Cyclopropane → propene	375
Alcohols → alkenes + H_2O	350
2 Alcohols → ether + H_2O	400
Skeletal isomerization of alkenes	600
o-Xylene isomerization	770

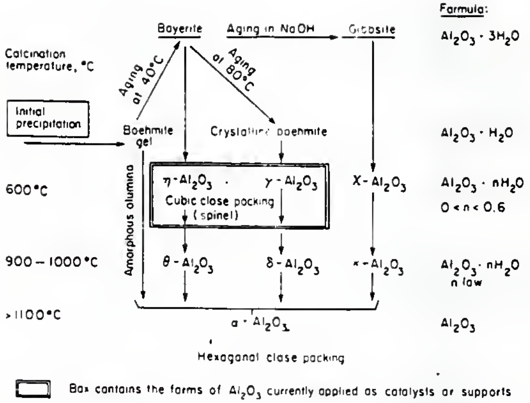

Figure 1.1. A Schematic Representation of formation of various Al_2O_3 hydrates. (3)

$$2CO = CO_2 + C.$$

The carbon that is left by the reaction is believed to be deposited on the surface of the alumina. This is based on the visual observation that after the reaction had occured for a few hours, the alumina had turned from its initial white to gray or black. The rate of the reaction was found to decrease initially as the reaction proceeded. This initial decrease was investigated using techniques developed by Froment and Bischoff (4).

CHAPTER 2

STRUCTURE OF ALUMINA

2.1 Introduction

Alumina can exist in many different structural phases, each having different properties. The phases have been divided into 3 groups. The first group is called the stable low temperature aluminas, sometimes called alumina hydroxides. This group includes bayerite, boehmite, gibbsite, diaspore, and norstrandite. The second group is called the transition phases and include eta, gamma, theta, delta, kappa, and chi aluminas. Finally there is an alpha phase which is often called corundum. All other phases of alumina will transform to the alpha phase on heating to 1200°C. The transition aluminas are formed by heating the different low temperature alumina phases. A figure showing the relationship between the phases can be seen in Figure 1.1. The transition of the aluminas only occur in one direction. That is, once a phase has been obtained by heating of an earlier phase, the alumina will remain in the new phase even after the temperature is lowered.

In all of the phases except alpha, water is present in the structure as hydroxyl groups. As the aluminas are heated some of these hydroxyl groups combine, releasing water and leaving an oxygen. No hydroxyl groups are found in the alpha phase. The amount of water that is present in the different phases can also be seen in Figure 1.1.

In this chapter the structures of the aluminas are described.

2.2 Alpha Alumina (Corundum)

Alpha alumina, also referred to as corundum, is a very crystalline substance giving rise to very sharp x-ray diffraction lines. All of the other forms of alumina transform to the alpha phase upon heating above 1200°C. Alpha alumina is widely used as an abrasive.

To describe the structure of alpha alumina, we must start with the positioning of the oxygen atoms. Alpha alumina has its oxygen atoms in a hexagonal close packed arrangement. This can be visualized by starting with a single layer of close packed spheres, which will represent the oxygen atoms. The layer will have trigonal symmetry with each oxygen atom on the bottom layer represented by an open circle in Figure 2.1. Next, a second layer of oxygen atoms is placed on the first layer. Each of the oxygens in the second layer is placed in a hole that was made by the first layer. This is also shown in Figure 2.1. The third layer of oxygens is then placed in positions directly above the first layer, and the stacking sequence of layers 1,2,1,2,1 etc. is repeated. See Figure 2.2.

The aluminum cations (Al^{3+}) are located in the interstices between the close packed oxygen layers. They are placed just above the triangularly formed holes seen in Figure 2.1. The next oxygen layer is placed over the aluminum cations. The Al^{3+} ions are then located in what is called an octahedral site, because of the eight sided figure that

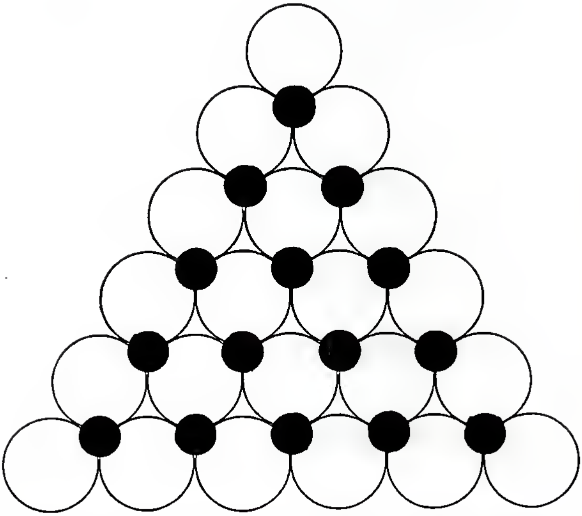

Figure 2.1. A representation of the close packed oxygen atoms that are needed to form α alumina. The large circles represent the oxygen atoms in the bottom layer and the dark circles, the positions of the oxygen atoms in the second layer.

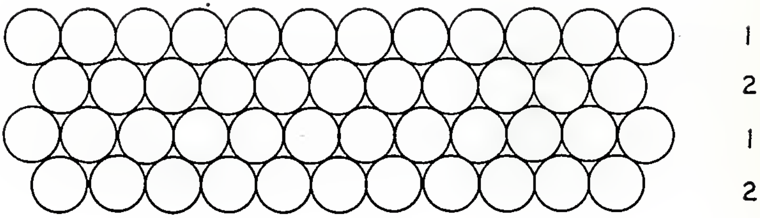

Figure 2.2. The stacking sequence of close packed oxygen layers that make up a hexagonal close packed arrangement that is seen in α alumina. The layers are viewed from the side.

is produced by the six oxygen atoms nearest to the Al^{3+} cations. An octahedral site is pictured in Figure 2.3.

If an aluminum cation was to occupy every available octahedral site, there would be the same number of aluminum and oxygen atoms in the structure and it would not meet the requirement of electrical neutrality. To make the crystal electrically neutral, one out of every three Al^{3+} sites must remain vacant. This vacancy leads to several possibilities for symmetry for the Al^{3+} cations. The configuration is usually taken to be that shown in Figure 2.4.

The structure of alpha alumina is completed by subsequent stacking of the layers of oxygen and aluminum ions (3,5,6,7,8).

2.3 Gibbsite (Hydrargillite)

Gibbsite is described as being an aluminum trihydroxide or alumina trihydrate because it can be written in the following forms: $Al_2(OH)_3$ and $Al_2O_3 \cdot 3H_2O$. Gibbsite is also often referred to as hydrargillite in German and French studies. Gibbsite occurs naturally and is the principle component in the bauxites of North America (6). It is also used as an intermediate in the production of aluminum metal by the Bayer Process (6).

Gibbsite has always been found to contain .2 - .3% Na_2O. Washing with dillute or concentrated HCl does not decrease the sodium content. It has been stated that the alkali oxide must be present in order to form gibbsite, but this has not been strictly proven. Ginsber and Koster in 1952 showed that the sodium that is present is atomically

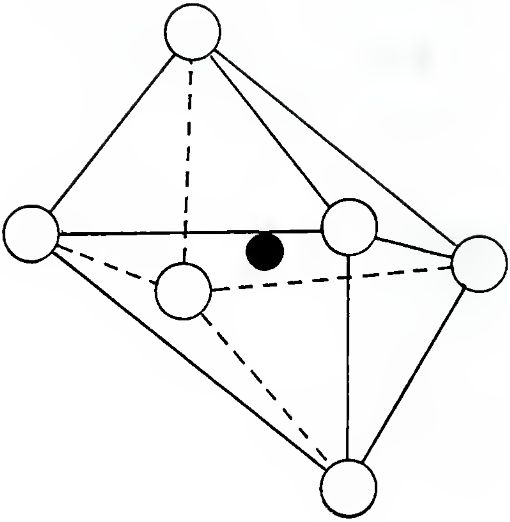

Figure 2.3. The dark circle shows the position of an octahedral site formed by the surrounding atoms. The lines illistrate the eight sided solid figure formed by the surrounding atoms.

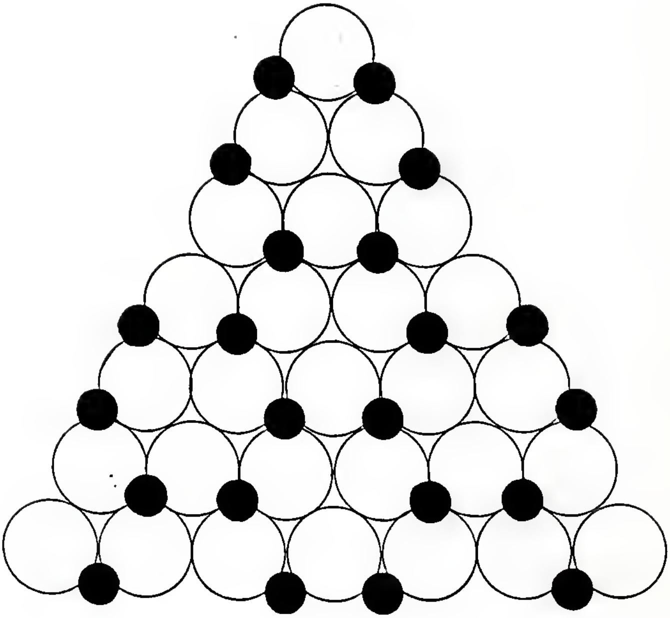

Figure 2.4. ● Al^{3+} ○ O^{2-}
The arrangement of aluminum cations on a close packed layer of oxygen atoms found in alpha alumina. (3,8)

dispersed in the crystal lattice of gibbsite (9).

The structure of gibbsite is based on a double layer unit of close packed hydroxyl ions (OH^-). The second layer of hydroxyl ions are placed in the holes made by the first layer, just as the second layer of oxygen ions were placed on the first layer for alpha alumina. The Al^{3+} cations are then placed in the interstitial octahedral sites between the layers of hydroxyl ions. Only two-thirds of the possible Al^{3+} sites are filled to ensure that the crystal structure remains electically neutral. The unfilled octahedral sites are larger than the filled sites causing the lattice to be deformed as shown in Figure 2.5.

The stacking of the double layer units can be represented by 1,2,2,1,1,2, etc. where the 1 and 2 are hydroxyl layer of a double layer unit. Stacking in this manner places the OH^- ions in one double layer unit directly across from the OH^- ions in the next double layer unit. See Figure 2.6. The double layers are held together by hydrogen bonds. The distance between two adjacent 1 or 2 layers in different double layer units is 2.81Å, compared to 2.03Å for the distance between 1 and 2 layers of the same double layer unit (5).

2.4 Bayerite

Bayerite is also a trihydroxide but unlike gibbsite, it does not occur naturally, however it can be readily produced in the laboratory. A simple method for the preparation of crystallographically pure bayerite has been given by Schmah

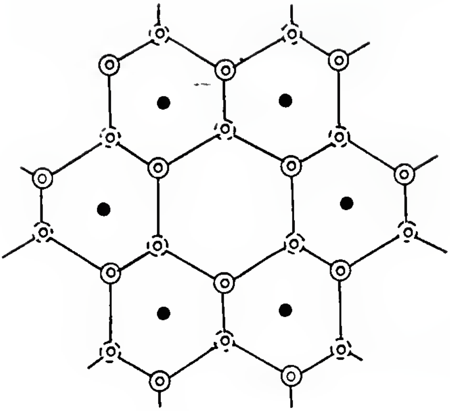

◌ OH^- ions in a plane below the paper.

◎ OH^- ions in a plane ablove the paper.

● Al^{3+} ions in the plane of the paper.

Figure 2.5. The deformation in the gibbsite structure caused by the vacant octahedral sites and the interaction between the Al^{3+} and OH^- ions. (9)

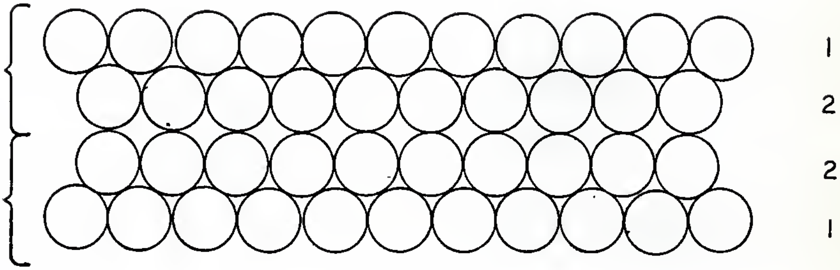

Figure 2.6. The stacking sequence of the OH^- ion layers that is present in gibbsite. The stacking sequence is 1,2,2,1,1,2... .

in 1946 (9). In this procedure amalgamated aluminum is oxidized by water at room temperature, more will be said about this later. Bayerite is also different from gibbsite in that bayerite can be made without any substantial amount of alkali (5).

The exact structure of bayerite is not known because single crystals large enough to be used for structural analysis are not available. The crystal size of the best crystallized bayerite observed so far is less than 10 microns across (6). Powder x-ray diffraction patterns cannot be used to precisely determine the structure because of the low symmetry of bayerite and many of the overlapping diffraction lines cannot be resolved. The case is made worse with bayerite because cyrstallinity is difficult to control and stacking faults in the crystal lattices are common.

Despite all of the problems associated with determining the structure, there is little doubt that the structure of bayerite is much like that of gibbsite. Bayerite, like gibbsite, is composed of double layer units of close packed hydroxyl ions with two-thirds of the octahedral sites filled with Al^{3+} cations. However, in bayerite, the double layer units are stacked so that they can be represented as 1,2,1,2, etc. like that of aplha alumina seen in Figure 2.2. This means that the hydroxyl ions in the third layer of the structure are directly above those of the first layer.

The double layer units are again held together by hydrogen bonds. The distance between layers 1 and 2 in a single double layer unit is 2.64Å, and the smallest distance between adjacent double layers is 3.13Å. The distance between adjacent double layers is larger in bayerite than in gibbsite because of the stacking faults in bayerite.

2.5 Boehmite

Boehmite is known as an alumina monohydrate ($Al_2O_3 \cdot H_2O$) and is found in nature in the European bauxites (7). When discussing boehmite a clear distinction should be made between well crystallized boehmite and gelatinous boehmite which is sometimes called pseudoboehmite. Pseudoboehmite gives x-ray diffraction patterns of broad bands with spacings similar to the most intense lines of well crystallized boehmite. Pseudoboehmite also has a very extensive surface area (approximately 400 m^2/g) and has a water content of 1.3 to 1.8 moles per mole of Al_2O_3. This is slightly higher than well crystallized boehmite (9). The notation used in this work will be boehmite to refer to well crystallized boehmite and pseudoboehmite to refer to the gelatinous form of boehmite.

Just as for bayerite, no single crystals of sufficient size for structural analysis of boehmite are available. It has been found that the iron compound lepidocrocite is isomorphous with boehmite. That is, it has the same structure as boehmite (9). This fact has been used to help estimate the structure of boehmite.

Van Oosterhout in 1960, produced an easy way to describe the structure of lepidocrocite, which in turn, can be used to describe boehmite (9). First, long chains of the type shown in Figure 2.7a must be constructed. The chains are then viewed from the side and represented by Figure 2.7b. Next, two of the chains are placed antiparallel to each other. See Figure 2.7c. Now the oxygen atoms in the second chain are on the same level as the aluminum atoms of the first chain. The chains are then connected together as shown in Figure 2.8. Each of the antiparallel units are held in place by hydrogen bonding. As is evident from Figure 2.8, the structure involves a packing of the double chains parallel to each other. The close packed anion planes are mixed and contain O^{2-} and OH^- ions. The Al^{3+} cations are found in the octahedral sites in rows parallel to the chain row, with every other row being vacant. The cleavage planes are given by the position of the hydrogen bonds and are indicated in Figure 2.8.

2.6 Diaspore

Diaspore is also an alumina monohydrate, like boehmite, and is found naturally in the high alumina clays of east Missouri and central Pennsylvania. The main use of diaspore has been in refractory brick (7). The structure of diaspore has been determined by using natural single crystals. It has also been found that diaspore, like boehmite, has an iron compound that is isomorphous. The iron compound is goethite (9).

To visualize the structure of diaspore, one must first

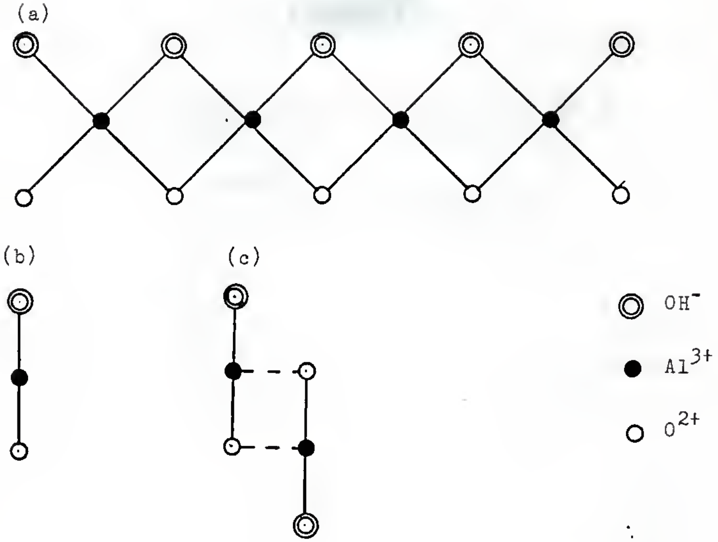

Figure 2.7. (a) Planer chains that are used to build the boehmite structure. (b) A representation of the chains extending into the plane of the paper. (c) The positioning of chains that are antiparallel to one another. (9)

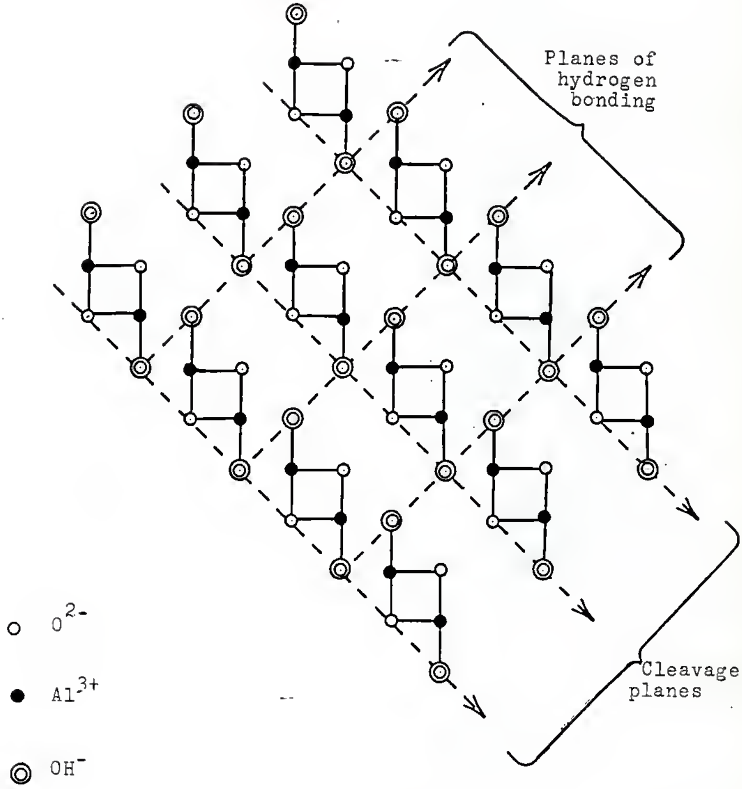

Figure 2.8. Arrangement of the antiparallel units needed to make the layered structure of boehmite. (9)

construct the double chain units as was done with boehmite. Then the double layer units are connected together as shown in Figure 2.9 (5,9). Again, the units are held in place by hydrogen bonds which also determine the cleavage planes.

2.7 Norstrandite

In 1956 Van Norstrand, Hettenger and Keith published an x-ray diffraction diagram of an aluminum trihydroxide that was different from gibbsite or bayerite (7). These workers referred to this new structure as bayerite II. European scientists, once this new structure was discovered, started to call it norstrandite in honor of Van Norstrand, which has become the accepted name. Since its discovery, norstrandite has been found to occur naturally as a compound of tropical red soils (terra rossa) in west Sarawak and on the island of Guam (6).

Lippens (9) stated that the lattice of norstrandite must strongly resemble those of the other trihydroxides, gibbsite and bayerite. With the aid of powder x-ray diffraction, and electron diffraction of single crystals, Lippens was able to assume that the lattice of norstrandite was based on a stacking of the same neutral double layer of alumina that were used in both bayerite and gibbsite. That is, he thought of norstrandite as built with double layer units of the bayerite stacking sequence along with double layer units of the gibbsite stacking sequence.

The stacking of the layers of the different sequences was possible in two different ways. See Figure 2.10.

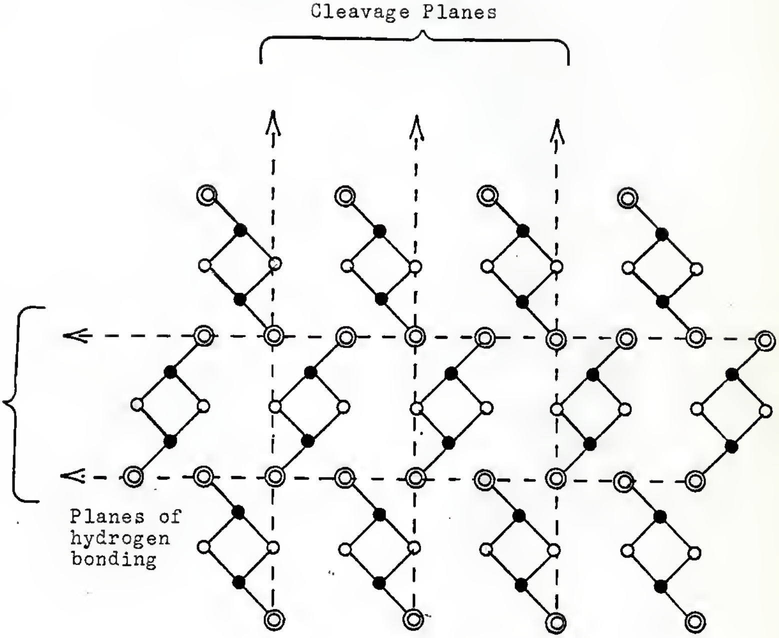

Figure 2.9. The arrangement of the antiparallel units for diaspore. (9)

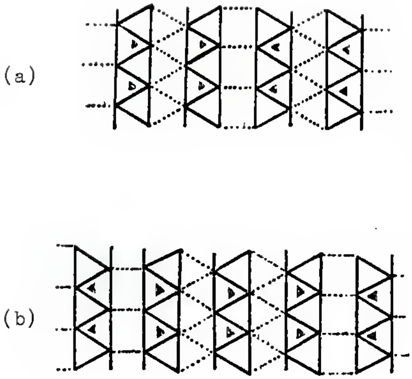

Figure 2.10. The two possible arrangements for the stacking sequence of norstrandite. The full lines represent the ionic bonds, while the ditted lines represent hydrogen bonds. The structure shown in (b) is more consistant with observed x-ray diffraction patterns of norstrandite. (9)

Electron diffraction of synthetic single crystals helped to eliminate the sequence shown in Figure 2.10a, thereby choosing the sequence shown in Figure 2.10b because it was in good agreement with the observed diffraction pattern. Hauschild in 1963 found that the layers of norstrandite were held together by hydrogen bridges (6).

Saalfeld and Jarchow also studied the structure of norstrandite (5). They postulated that the sequence of layers is 1,2,1,2, etc. as in bayerite, but that the OH^- ions of adjacent double layers are located opposite each other. This places the lattice of norstrandite between those of bayerite and gibbsite.

2.8 Eta and Gamma Alumina

Eta and gamma alumina are widely used as supports for dispersed metal catalysts. Eta is obtained by dehydrating bayerite while gamma is formed by dehydrating boehmite. Despite coming from different phases, eta and gamma alumina have very similar structures in which the oxygen atoms are arranged similar to the mineral spinel, $MgAl_2O_4$ (3). Therefore, eta and gamma are often said to have a spinel or defect spinel structure. The oxygen ions in the spinel structure form a cubic close packed system. This can be imagined by starting with the first two layers of oxygen atoms as described for alpha alumina, but this time the third layer of oxygen atoms is placed above another set of holes in the first layer that were not filled by the second layer. The stacking sequence is then 1,2,3,1,2,3, etc.. See Figure 2.11.

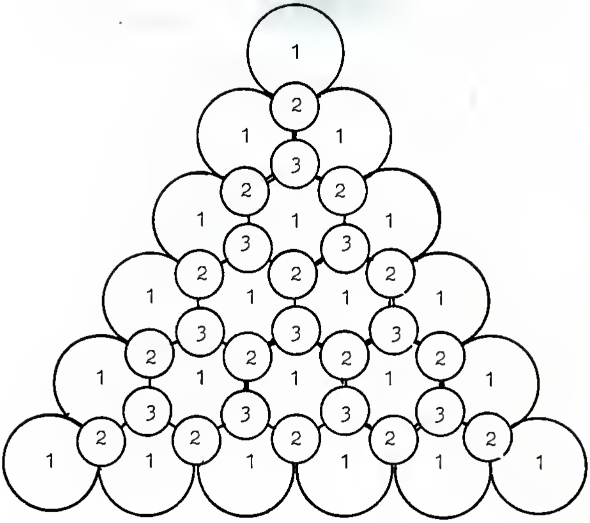

Figure 2.11. This is a representation of the position of the oxygen atoms for a cubic close packed system. The numbers indicate the layer in which the oxygen atoms are positioned.

In spinel, $MgAl_2O_4$, the Mg^{2+} ions occupy the tetrahedral positions and the Al^{3+} cations are located in the octahedral positions. The structure of spinel can be seen in Figure 2.12. The unit cell contains 32 O^{2-} ions, with 16 octahedral sites all occupied by Al^{3+} ions, and 64 tetrahedral sites, only 8 of which are filled with Mg^{2+} ions. In order to make the comparison between eta, gamma and spinel, the alumina's formulas must by written as $(H_{\frac{1}{2}}Al_{\frac{1}{2}})Al_2O_4$ or $Al(H_{\frac{1}{4}}Al_{\frac{3}{4}})_2O_4$ (3). It is now seen that some of the Al^{3+} ions as well as the hydrogens must be located in the tetrahedral sites. See Figure 2.13. The hydrogens in the structure are probably connected to an adjacent oxygen atom to form an hydroxyl group.

The differences between the eta and gamma structures are very subtle but have a distinctive bearing on the properties of the two aluminas. In gamma alumina the oxygen lattice is fairly well organized, while in eta alumina stacking faults are relatively frequent. Thus deviations from the regular stacking arrangement of oxygen atoms can occur such as 1,2,3,1,3,1,2,1,2,3,2,3, etc.. Leonard et al. (10) proposed that eta and gamma should be distinguished from the standpoint of their oxygen packings. The oxygen lattice for gamma is more densely packed than eta. This was thought to be a direct consequence of the higher amount of stacking faults in eta. This is also in agreement with the higher surface area that is seen for eta. Eta has a maximum surface area of about 250 m^2/g, while gamma's

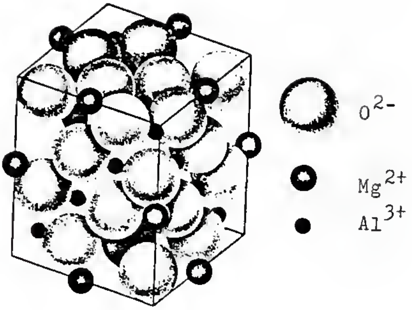

Figure 2.12. The unit cell of spinel ($MgAl_2O_4$). (3)

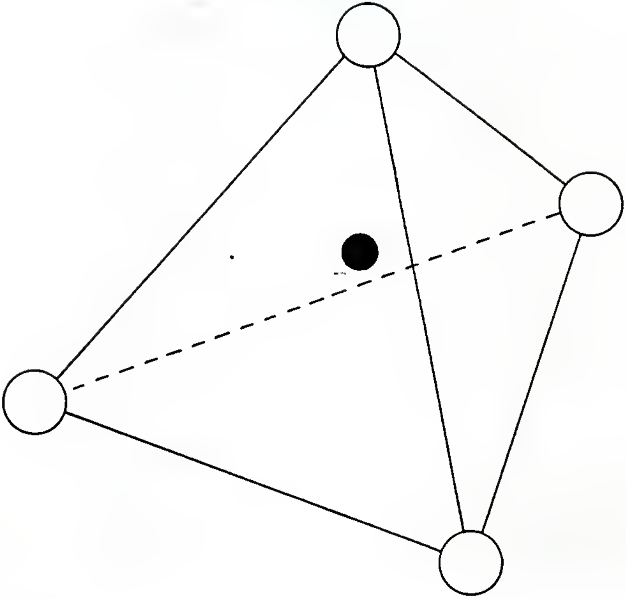

Figure 2.13. The black sphere in the center represents a tetrahedral sites produced by the surrounding atoms.

maximum was found to be about 200 m^2/g.

It has also been found that the fraction of tetrahedral sites that are filled with Al^{3+} ions is slightly higher for eta than for gamma, but that the octahedral sites are still preferentially occupied. Because of this higher content of Al^{3+} ions in the tetrahedral sites, eta is found to be more acidic than gamma. This increased acidity is because the oxygen and hydroxyl groups connected to a Al^{3+} ion in the tetrahedral positions have their electrons pulled close to the Al^{3+} ion because it is surrounded by only 4 oxygens or hydroxyl groups, instead of the six for an octahedral site.

2.9 Theta Alumina

Theta alumina has been found to be isomorphous with β-Ga_2O_3 by many authors (11,12) who have shown that these two compounds form complete solid solutions. Single crystals of theta alumina large enough for structural determination have not been available, but can be obtained for β-Ga_2O_3. Because of this, the structure of theta alumina has been largely determined by examining the isomorph.

The structure of theta alumina can be described as a deformed spinel lattice or a distorted cubic close packed lattice, in which three-quarters of the Al^{3+} cations are located in the octahedral positions and the remaining are in the tetrahedral positions. A view of the structure can be seen in Figures 2.14 and 2.15.

It is curious to note that the next structure obtained

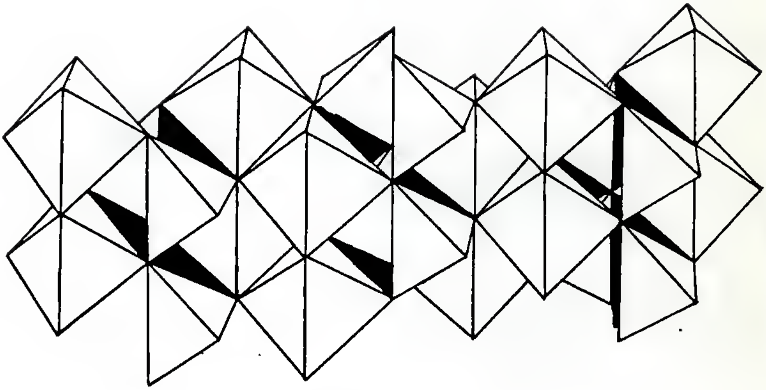

Figure 2.14. A geometric representation of the structure of theta alumina. It is helpful to view this figure in conjunction with figure 2.15. (11)

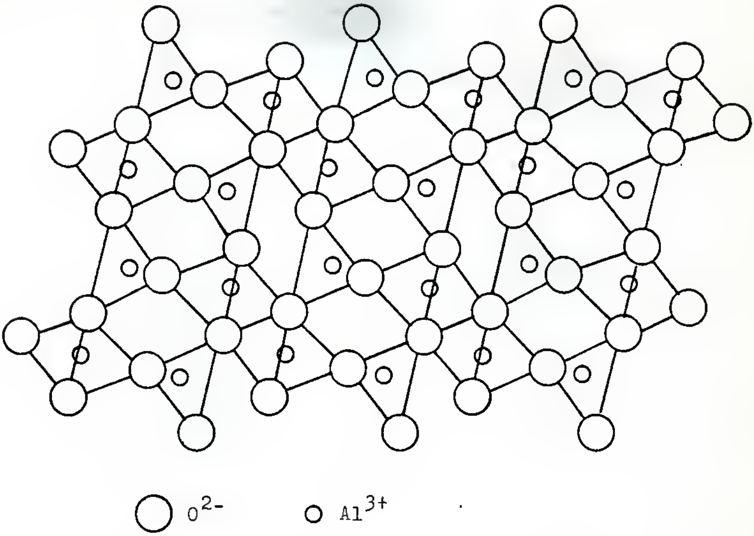

Figure 2.15. A representation of theta alumina indicating the relative positions of the atoms in the structure. Lines connecting the atoms indicate the manner in which the octahedra and tetrahedra are constructed from and joined by the oxygen atoms in the three consecutive symmetry planes. Only the upper faces of the polyhedra are depicted. For increased clarity, this figure should by studied simultaneously with figure 2.14. (11)

by dehydrating theta alumina is alpha alumina in which the Al^{3+} cations are located in octahedral sites only. Also in alpha alumina, the oxygen lattice has a stacking sequence of 1,2,1,2, etc. and this sequence gives a hexagonal close packed structure to the oxygens. Therefore, in order for alpha alumina to be formed there must be some reorientation of the oxygen atoms. It seems that the Al^{3+} ions in the tetrahedral positions promote this reorientation that occurs at temperatures greater than 1200° C (9). However, theta and alpha alumina phases are stable at room temperature, that is, at room temperature the reorientation proceeds infinitely slow (11,13).

2.10 Kappa Alumina

Kappa alumina, like theta, has a gallium isomorph ε-Ga_2O_3. Kappa alumina is formed by dehydrating gibbsite at temperatures between 800 and 1200°C (14). Little is known about the structure of kappa and there is some disagreement between authors about the structure. Saalfeld and Brindley and Choe (15,16) agree that between 800 and 1200°C, more than one structure may exist. However, Saalfeld only reported one structure.

According to Saalfeld, in 1960, kappa alumina has a layered sequence of 1212-2121 etc., with the aluminum atoms occupying both the octahedral and tetrahedral positions (7,15).

2.11 Chi Alumina

Chi alumina is the lowest transition phase obtained from gibbsite and is obtained by heating gibbsite in air or nitrogen at 300°C. It has a diffuse x-ray diffraction pattern but can be distinquished from other low temperature aluminas by an x-ray diffraction line corresponding to a spacing of 2.11 Å (7).

Both Saalfeld and Brindley and Choe state that chi alumina is built with a stacking sequence of oxygen layers that follows the pattern 1,2,1,2, etc.. That is, it has a hexagonal close packed oxygen structure (7,16). Saalfeld also stated that the aluminum ions occupy the octahedral positions and that the stacking sequence of the layers is strongly disordered (6).

2.12 Delta Alumina

Delta alumina can be prepared by heating pure boehmite for one to two hours at 1000°C and, according to Stumpf has an orthorombic structure. Rooksby obtained a more crystalline material by prolonged heating or by addition of mineralizers. Rooymans found a relationship between the interplaner spacing and those found by Von Oosterhout and Rooymans for gamma ferric oxide, regarded as a defect spinel. The unit cell contains three spinel unit cells, therefore it contains a whole number of Al_2O_3 molecules. A fourfold screw axis parallel to the c-axis was also found by Lippens. Saalfeld, on the other hand denied the existence of deta alumina (7).

CHAPTER 3

SURFACE MODELS FOR ETA AND GAMMA ALUMINA

3.1 Introduction

Ideal surface places can be expected if the bulk structure is extended regularly to the surface to that well defined crystallographic planes will terminate the lattice and therefore be present on the surface (2). The simplest case is then obtained when only one crystallographic plane is preferentially exposed at the surface. Catalytic and surface chemists concluded that the preferentially exposed faces may be the {111} face for eta and the {110}, {100} faces for gamma. (The numbers given are the Miller indicies for specific planes of a crystal.) In reality the {111} and {110} planes are thought to form the surface layers of eta and gamma respectively. Because eta and gamma are the most frequently used forms of alumina, most of the surface models have dealt with these two forms and they will be the only ones discussed in this work.

3.2 Surface Models of Eta and Gamma by Knozinger and Ratnesamy (2)

Lippens proposed the models for the idealized planes of eta and gamma (2,3,7). For eta, start with a close packed oxygen layer which was described before. The easiest way to visualize the {111} ideal surface for eta is to consider two types of arrangements of the Al^{3+} ions on two different close packed oxygen planes. These are referred to as the A and B layers in Figure 3.1. The B

Figure 3.1.

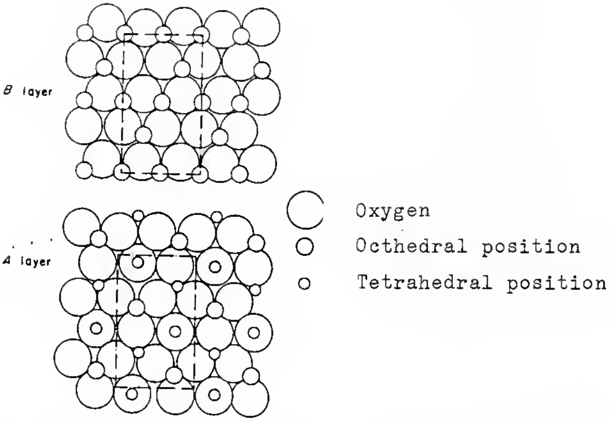

Structure of η alumina showing tetrahedral and octahedral Al^{3+} ion positions. (2)

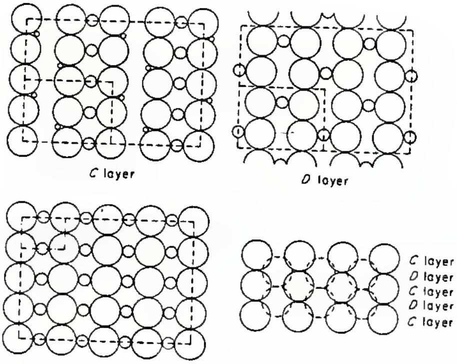

Structure of γ alumina showing tetrahedral and octahedral Al^{3+} ion positions. (2)

layer has Al^{3+} ions located in the octahedral positions only. The A layer is obtained by transferring 2/3 of the cation from octahedral positions, like those found in the B layer, to tetrahedral positions. See Figure 3.1. The resulting structure is made by stacking the layers in the sequence A,B,A,B, etc..

For gamma alumina, one must envision the {110} face with two planes labeled C and D that can also be seen in Figure 3.1. In the C layer equal number of cations are positioned in tetrahedral and octahedral interstices between the rows of oxygen atoms. The D layer has only octahedrally located Al^{3+} ions. The stacking of the layers for gamma alumina is C,D,C,D, etc..

Because of energetic reasons only anion layers will terminate a crystallite, and it is thought that these surfaces probably consist of OH^-groups. The surface layer parallel to the {111} plane of the spinel lattice can be envisioned by placing a close packed layer of OH^- groups on the A and B layers.

Consider the A layer covered with OH^- groups. Two types of OH^- configurations can be seen in this layer. A surface OH^- group that is coordinated to a single tetrahedral Al^{3+} cation. This OH^- group is called type Ia. Type IIa is an OH^- group which links a tetrahedral Al^{3+} to an octahedral Al^{3+} cation. Likewise, when the B layer is covered with OH^- groups, two configurations are seen. Both configurations consist of bridging OH groups. Type IIb links two Al^{3+} ions that are in the octahedral positions. While, type III is coordinated to three Al^{3+} ions in the octahedral positions. In this layer it is found that type IIb groups occur three times as frequently as type III and in the A layer type IIa are also three times more abundant than type Ia. If possible vacant positions are taken into account a fifth configuration is seen called type Ib, in which the OH^- group is coordinated to a single cation in an octahedral site. Schematics of these five types of OH^- groups may be seen in Table 3.1.

Upon looking at the C and D layers covered with OH^- groups for the {110} plane, it is found that only 3 possible configurations can occur. These configurations are called type Ia and IIb for the C layer, and type Ib for the D layer. These groups can also be seen in Table 3.1.

If one were to envision the {110} plane of the spinel lattice it could be represented by a square lattice of oxygen atoms where only octahedral cation positions are possible. If this layer were covered with OH^- groups, one would find that only a single OH configuration could exist. It is called type Ib. A summary of all of the possible configurations for all the planes dealt with here can be seen in Table 3.1. Also in Table 3.1 is the net charge at a surface oxygen and a surface OH^- group for the various configurations. (ie. if the planes were covered with oxygen instead of OH^- groups) According to Pauling, the net charge in a stable ionic structure should be equal to

Table 3.1

Possible OH Configurations. (2)

Crystal face	Layer	Configuration		Coordination numbers of surface anions		Net Charge at O	Net Charge at OH	$\tilde{\nu}$ (OH) cm^{-1}
				AI(VI)	AI(IV)			
(111)	B		III	3	-	-0.5	+0.5	3700-3710
	B		IIb	2	-	-1.0	0	3740-3745
	A		IIa	1	1	-.75	+.25	3730-3735
	A		Ia	-	1	-1.25	-.25	3760-3780
	A,B		Ib	1	-	-1.5	-.5	3785-3800
(110)	C		IIb	2	-	-1.0	0	3740-3745
	C		Ia	-	1	-1.25	-.25	3760-3780
	D		Ib	1	-	-1.5	-.5	3795-3800
(100)			Ib	1	-	-1.5	-.5	3785-3800

Large circles are oxygen atoms or hydroxyl groups.
● Al atoms in octahedral positions. AI(VI)
○ Al atoms in tetrahedral positions. AI(IV)

or very near zero. This is found to be better approximated when the surface is covered with OH^- groups instead of oxygen atoms. Also, the OH^- groups in the surface help explain the loss of water upon heating of the alumina as will be discussed later.

The OH^- groups in the different configurations were examined and found to have slightly different net charges and, as a result, have different properties. For example, one would expect type III groups to be the most acidic because if the hydrogen is removed only a charge of -.5 would remain on the oxygen. See Table 3.1. This is still close to zero, meeting the condition for a stable structure. Using the same argument, one would expect the acidity of the OH^- groups to decrease as the net charge that is left on the oxygen, once the hydrogen is removed, becomes more negative.

The proton acidity and the ease of removal of an OH^- group are important factors governing the dehydration process of these aluminas, at least at low temperatures when proton mobility is low. Consider the A layer again, type Ia and IIa hydroxyl groups are found to occur as neighbors. Type Ia is the more acidic group and type IIa the more basic group. Thus these two groups should combine with the Ia hydroxyl group taking the hydrogen from the IIa group, and a water molecule is released. This would result in the formation of an anion vacancy and therefore a Lewis acid site. This also would expose a 3-coordinated Al^{3+}

cation in a tetrahedral interstice together with an oxygen, which would be a Lewis base site, and would between tetrahedral and octahedral ions. See Figure 3.2.

In the B layer types IIb and III exist as neighbors and would combine with IIb being the more basic. This would create vacancies that would expose two 5-coordinated cations in octahedral sites. Combinations in the C layer would follow the same principles. However, in the D layer, where all the OH^- groups are type Ib the removal of water molecules by combination of OH^- groups would probably follow the method used by Peri (17) which is described later.

According to the above model, the dehydration of the surface should proceed based on the relative basicities and protonic acidity of neighboring OH^- ions and their orientations. Dehydration could proceed in this manner to about 50% dehydration on the A and B layers where type IIa and IIb groups would be left. This is approximately the state of hydration that eta and gamma alumina are in when heated to about 500°C. The regular dehydration could be disturbed by several factors. One way for this to occur is the formation of type Ib groups from either a type IIb or IIa configuration, or the less favorable combination of two neighboring OH^- groups. This will lead to defect sites on the surface.

The above model for the surface of eta and gamma alumina based on ideal surfaces was put forth by Knozinger and Ratnesamy (2). Next a model for the surface of

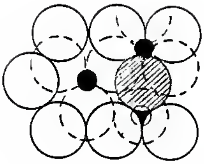

Figure 3.2. A representation of an Anion vacancy/oxygen pair in the (111) face A layer of eta alumina. (2)

● - Al^{3+}

○ - Hydroxyl group in the plane of the paper

◌ - Hydroxyl group in the plane below the paper

▨ - Oxygen atom in the plane of the paper.

gamma alumina that was put forth by Peri will be discussed (17).

3.3 Surface Models of Eta and Gamma by Peri (17).

Peri assumed that the {110} plane of gamma was the plane that was preferentially exposed. Also in Peri's model the following assumptions were made. The surface was to include two outer layers of an ionic crystal and only one face was exposed. On ideal dry alumina the top layer contained only oxygen ions regularly arranged over Al^{3+} ions in octahedral sites in the next lower layer. See Figure 3.3. Only as many cxygen ions were present in the top layer as in the next lower layer. The stoichiometry of the two upper layers combined corresponded to Al_2O_3. At 100°C, or higher depending on the method of rehydration, enough chemisorbed water is held to convert the top layer to a filled square lattice of hydroxyl groups as shown in Figure 3.3. When the top layer is filled, each hydroxyl ion is assumed to be directly over an aluminum ion in the next lower level.

Next, in order to reduce the dissorder that would result from a purely random process, the assumption was made that water must initially be removed in such a way that two or more oxygen atoms are not left on immediately adjacent sites. Also, water was not removed that left adjacent sites vacant. Using these rules a Monte Carlo type of process was carried out. It was found that the rate of OH^- removal decreased rapidly with decreasing surface coverage. The rate of removal approached zero at

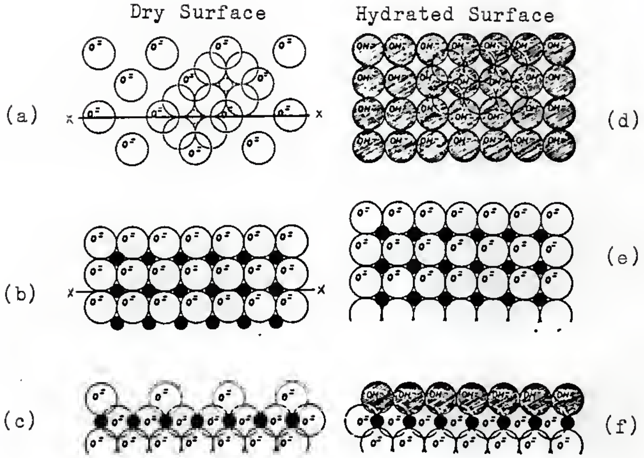

Figure 3.3. The ideal (100) surface of the spinel type alumina. Figures a, b, and c deal with the dry surface. Figure (a) shows the surface lattice of oxide ions remaining after removal of water. (b) is the next lower plane where alternated Al^{3+} ● ions that lie beneath oxide ions of the surface lattice. (c) The section perpendicular to the surface at x-x. Figures d, e, f deal with the hydrated surface. (d) Show the surface layer of hydroxyl ions. (e) Is the next lower plane and the Al^{3+} ions ● lie directly below the OH^- ions of the surface layer. (f) Section perpendicular to surface. (17)

approximately 67% removal.

Futher dehydration of the surface required the creation of oxide and/or vacancy defects. When the restrictions in the preceding paragraph were lifted the hydroxyl removal was continued until 82% had been removed. Many isolated OH^- groups remained, and there were various defects present.

The remaining OH^- pairs were removed by a random process. Finally, the remaining OH^- ions covered 9.6% of the lattice. It was found that the remaing OH^-ions could be classified into five types of sites in which they had from zero to four nearest neighbors. These are shown and given a better identity in Figure 3.4. The sixth type of site in which two oxygen ions were symmetrically located on opposite sides of the OH^- group, was negligible.

The most negative OH group was found to be type A with four oxygen molecules as its nearest neighbors. Type C was found to be the positive with four vacant sites as neighbors. The order of decreasing basicity for the sites was A,D,B,E,C, with A being the most basic.

Both of the models described in this chapter seem to do a reasonable job in explaining some of the results obtained from infrared studies of the surfaces of eta and gamma. However, it should be noted that the literature dealing with the infrared studies of alumina surfaces is quite large and contains many conflicting results. Some of the conflicts may be due to different starting materials and variations in preparation procedures, which from experience yields

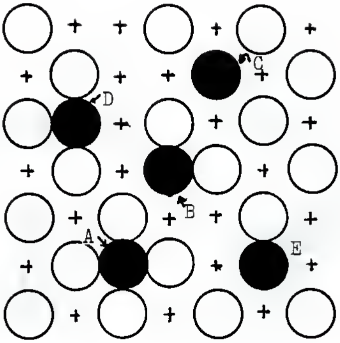

○ O^{2-}

● OH^-

\+ Denotes Al ion in lower layer.

Figure 3.4. Types of isolated hydroxyl ions. (17)

aluminas with very different properties. The major flaw in these models of the surfaces, seems to be that they deal with idealized surfaces, and they assume that only one plane is preferentially exposed. This is probably not the case at all. In fact, the true surface is probably a mixture of different exposed planes which is a result of stacking defects and other non-uniformities in the structure. The fact remains that these models give some insight as to the nature of the surface of eta and gamma alumina despite being idealized.

CHAPTER 4

X-RAY DIFFRACTION

4.1 Introduction

X-ray diffraction is a technique used to gain information concerning the structure of crystalline materials. A crystalline material is one in which the atoms are arranged in an ordered, repeating, three dimensional pattern. Essentially all metals, a significant fraction of ceramics, and certain polymers are considered crystalline materials (18). If a material does not possess an ordered repeating pattern it is called amorphous (without form). Glasses, liquids, and gases fall into the amorphous catagory.

In this work, x-ray diffraction was used to differentiate between the many possible crystalline phases that can be formed by alumina. This chapter describes how x-ray diffraction patterns are formed by crystalline substances and the information that can be obtained from the diffraction pattern. This chapter deals mainly with the diffraction patterns obtained by the powder method.
X-ray diffraction is not a normal part of the curriculum in chemical engineering. Therefore, this chapter and the corresponding appendix were written to aid future students in understanding x-ray diffraction and the information that may be obtained from it.

4.2 Theory of X-ray Diffraction Patterns

When x-rays strike an atom in a material, the rays are scattered in all directions and the diffraction pattern obtained is due to the interference patterns of waves as they are scattered from the atoms. Therefore, a diffracted beam may be defined as a beam composed of a large number of scattered rays mutually reinforcing one another.

To more fully understand how a diffracted beam comes about, consider an incident x-ray beam striking a crystal as shown in Figure 4.1. The scattering from the first plane of atoms will be examined first, that is, rays 1 and 1a in the incident beam. The incident beams are all assumed to be in phase at X,X'. Beams 1 and 1a strike atoms K and P respectively, and are scattered in all directions. Only in the directions of 1' and 1a' however, are these scattered beams completely in phase and therefore able to reinforce one another. This reinforcement is made possible because the difference in the path lengths between wave fronts X,X' and Y,Y', for the two beams is equal to zero and is shown by the following equation.

$$QK - PR = PK\cos(\theta) - PK\cos(\theta) = 0 \qquad 4.1$$

The rays scattered by all the atoms in the first plane in the direction parallel to 1' are likewise in phase thereby making the diffracted beam more intense. This analysis can be performed for all the planes separately and found to be true.

Now consider rays 1 and 2 that strike atoms in planes A and B that are labeled K and P respectively. After the rays strike the atoms they are scattered in all directions.

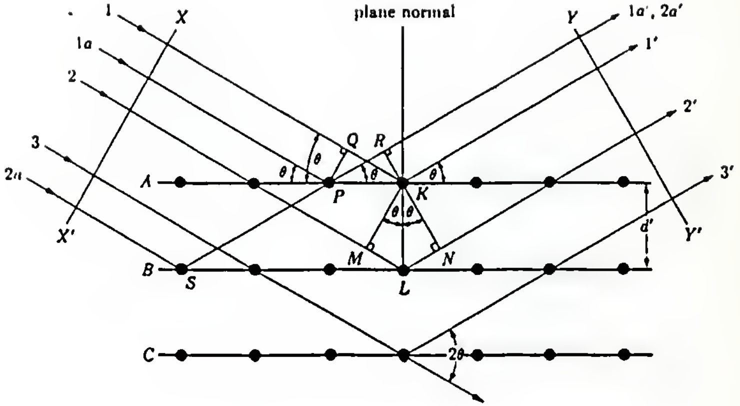

Figure 4.1. Diffraction of x-rays by a crystal. (38)

The path difference between rays 1 and 2 from the wave fronts X,X' to Y,Y' is given by equation 4.2.

$$ML - LN = d' \sin(\theta) + d' \sin(\theta) = 2d' \sin(\theta) \qquad 4.2$$

(This is also the path difference between rays 1a and 2a.) The scattered rays 1' and 2' (1a' and 2a') will be completely in phase and reinforce each other if the path difference is an integer number of wavelengths, which is given by equation 4.3.

$$n\lambda = 2d' \sin(\theta) \qquad 4.3$$

where

$n = 1,2,3,4 \ldots$

λ = The wavelength of radiation that is used.

Equation 4.3 is known as Bragg's Law. It states the essential condition that must be fulfilled in order for diffraction to occur. The angle at which diffraction occurs is sometimes called the Bragg angle. "n" is referred to as the order of the reflections and is equal to the integer number of wavelengths needed to traverse the path difference. Therefore, if monochromatic radiation is used, the smallest spacing between the planes may be found by assuming n=1, obtaining θ from the diffraction pattern, and solving equation 4.3 for d'.

In a diffracted beam the scattered rays 1' and 2' would differ in path length by one wavelength (n=1). Rays 1' and 3' would differ by two wavelengths (n=2), and so on down the crystal. The rays scattered by all the atoms in all the planes are completely in phase and reinforce one another by constructive interference. See Figure 4.2. In directions other than the Bragg angle, the scattered rays are out of phase and cancel one another through destructive interference shown in Figure 4.2.

A better idea of how the destructive interference comes about can be obtained by considering rays 1' and 2' at an angle different than that needed for diffraction. The phases of the rays with respect to one another could be like those shown in Figure 4.3. It is evident that the ray obtained by adding the two rays together is smaller than the ray obtained if constructive interference were occuring. Now consider the interference between rays 1' and 3' at the same conditions. Ray 3' strikes an atom in layer C and the interaction of rays 1' and 3' produces a wave that is even smaller than that obtained by combining rays 1' and 2'. If we continue to look at rays scattered from atoms in successively lower layers we would at some point see a ray scattered that would be exactly out of phase with ray 1' and completely destructively interfere with it. Then if we looked at the interference of ray 2' and the layer below the one that was exactly out of phase with ray 1', we would see these two rays are also exactly out of phase and cancel each other. Therefore if there were an infinite number of layers of atoms all the rays would be cancelled at all other angles except the Bragg angles.

However, crystals are only finite in thickness and we see that the closer we get to an angle where diffraction

Figure 4.2.

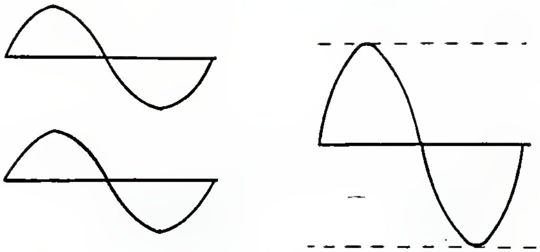

Constructive interference that occurs when two waves are exactly in phase with respect to each other. The waves reinforce each other .

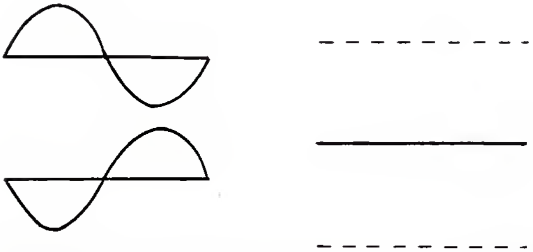

Destructive interference occurs when two wave are exactly out of phase with one another. The two waves then cancel each other.

Figure 4.3.

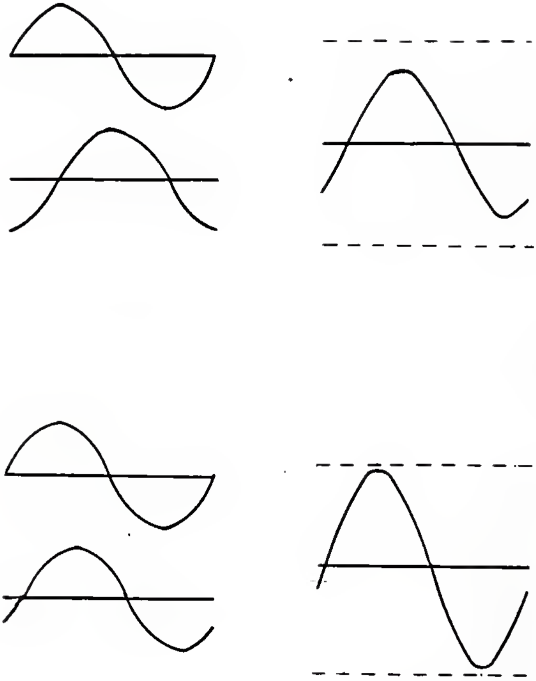

As waves that are more out of phase with respect to each other they interfere so to produce a resulting wave that has a lower intensity. Figure a is more out of phase than b and so the resulting wave is smaller for a than for b. The dotted lines is the amplitude that would result from complete constructive interference.

occurs the farther down the crystal we must go to find rays that will cancel rays from the surface. This is because the path difference of rays in adjacent layers for an angle near the angle of diffraction is very nearly an integer number of wavelengths. Hence, we must have a ray from far below the surface to have a path difference sufficient to produce destructive interference. If the crystal is large this is usually not a problem, but if the crystal is small we do not have the rays needed for the destructive interference. When this occurs a beam is emitted and we see a broadening of the angles in which diffraction occurs. Also, when the crystal is small the number of planes that are present to produce rays that constructively interfere at the correct angle is smaller and therefore the diffracted beam produced is not as intense as it would be for a larger crystal.

The diffracted beam is rather strong compared to the sum of all the rays scattered in the same direction simply because of the constructive interference that occurs. However, the diffracted beam is extremely weak when compared to the incident beam because the atoms scatter only a small fraction of the energy incident on them in the direction of the diffracted beam. If the atoms scattering the radiation were not arranged in a periodic fashion, for example a liquid or gas, the rays scattered by the atoms would have a random phase relationship to one another. In other words, there would be an equal probability of the path difference (phase difference) between any two scattered rays to be between zero and an integer number of wavelengths. Neither constructive or destructive interference predominates in this case, and the beam scattered in a particular direction is just the sum of the intensities of all of the rays scattered in that direction.

Diffraction differs from reflection in three fundamental aspects: 1. The diffracted beam from a crystal is built up of rays scattered by all of the atoms of the crystal which lie in the path of the incident beam. The reflection of visible light takes place in a thin surface layer only. 2. The diffraction of monochromatic x-rays takes place only at those particular angles of incidence that satisfy the Bragg Law. The reflection of visible light takes place at any angle of incidence. 3. The reflection of light by a good mirror is almost 100% efficient. The intensity of a diffracted beam, as stated before, is extremely small compared to the incident beam.

In summary, diffraction is essentially a scattering phenomena in which a large number of atoms participate. Since atoms are arranged periodically in a crystal lattice, the rays scattered by the atoms have definite phase relationships between them. These phase relationships are such that destructive interference occurs in most directions of scattering. However, in a few directions, constructive interference takes place and diffracted beams are produced.

The two items that are necessary to produce diffraction beams are a wave motion capable of interference (x-rays), and a set of periodically arranged scattering centers (atoms in a crystal). The reason x-rays are used instead of other electromagnetic radiation is because the wavelength of x-rays is on the same order of magnitude as the spacing between atoms in a crystal, ie. 1 to 2 Å.

4.3 Methods For Obtaining Diffraction Patterns

The Laue method, rotating crystal method, and the powder method are a few of the several different methods available to obtain diffraction patterns from a substance. Each method yields a different pattern, and therefore different information about the structure. Both the Laue and the rotating crystal methods require the use of large single crystals, while the powder method uses many small crystals in the form of a powder. Because large single crystals are not available for some of the alumina phases, the only method that can be employed on these phases to examine the structure is the powder method.

In the powder method the substance to be examined is crushed or ground to a very fine powder and placed in a beam of monochromatic x-rays. Each particle of the powder is a crystal or a group of smaller crystals, orientated at random with respect to the incident beam. Consider a substance with a structure of that pictured in Figure 4.4. In a powder of this substance some of the crystals, by chance, will be orientated so that the spacing d1 will

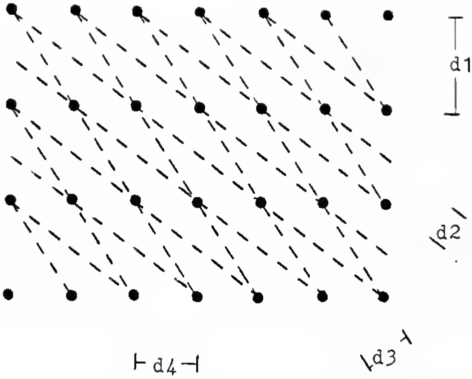

Figure 4.4. A representation of the different d spacings that can be produced by a crystal.

diffract at the correct angle and others will be orientated so that d2 will diffract and so on. Therefore, in the powder, every possible plane spacing will be represented. That is not to say that the intensities of all of the diffractions beams for all the spacings will be equal. The intensity of each diffracted beam depends on the type of atoms that are in the plane, the number of atoms in the plane, and the number of planes present.

There are however, some drawbacks in using the powder method alone instead of in connection with a single crystal method. The main drawback is that in a powder pattern there is no way to tell if the diffracted beam is produced by one set of planes with a particular spacing or if other sets of planes with the same spacings are involved. In order to make this point clearer, look again at Figure 4.4. If the planes that make up d2 were spaced so d2 and d1 were equal, then both sets of planes would cause a diffracted beam to occur at the same angle if the powder method were used. This would not be the case with the single crystal diffraction methods. Because of this possible production of a single diffracted beam by two different sets of planes, it is very difficult to determine the exact crystal structure of a material except in the simplest of cases. (ie. simple body centered cubic or simple face centered cubic)

Despite this, powder diffraction patterns are well suited to determine if a substance has changed structures after some treatment, or to confirm if a sample is in a particular structure by comparing the observed spacings to those found in the literature. This method works well to distinguish between the different crystalline phases of alumina. The only problem is that because of the closeness of the patterns obtained from eta and gamma, the powder method cannot tell if a mixture of these two phases are present. This will be discussed in more detail later.

In this work, the diffraction patterns were obtained using a Siemens x-ray tube, goinecmeter, and scintillation detector. The powder sample was mounted in an amorphous glass specimen holder and would stay in the holder well enough by packing with a slight amount of pressure, that no binder had to be used. A copper x-ray source was used and the beam was passed through a nickel filter to produce a nearly monochromatic beam. A step by step procedure used to obtain the diffraction pattern along with the settings of the instruments, is given in the appendix.

The x-ray diffraction patterns of the alumina prepared and used in this work can be seen in Figures 4.5 to 4.9. Literature values of the planer spacings for the various phases of alumina can be found in Table 4.1. It is evident from the diffraction patterns obtained that the boehmite and bayerite prepared using the amalgamation procedure are well crystallized. At first glance the diffraction patterns of eta and gamma look the same. However, on closer examination, the gamma pattern has two peaks overlapping at approximately 46 degrees, as is evident by the change in the slope of the peak. Also, eta has a sharper peak at 21 degrees, while gamma just shows a broad base. These are the features that Van Norstrand (19) used to distinguish between eta and gamma alumina. The reason these patterns are so close is because of the closeness of the stuctures themselves. As was stated in section 3.7, the only difference between eta and gamma is that eta has more aluminum ions in tetrahedral sites.

Figure 4.5

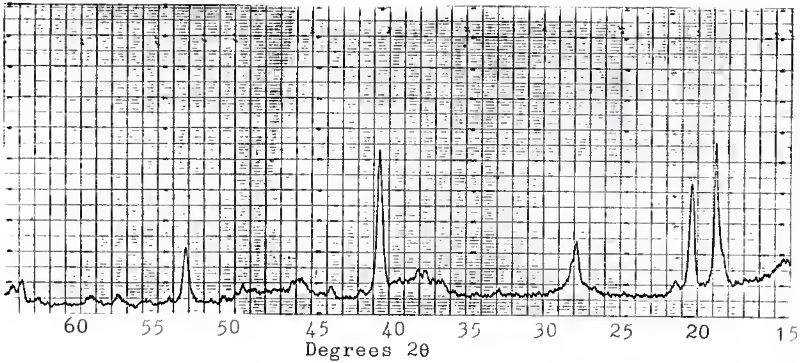

X-ray diffraction pattern of bayerite that was made by the procedure outlined in this work.

Figure 4.6.

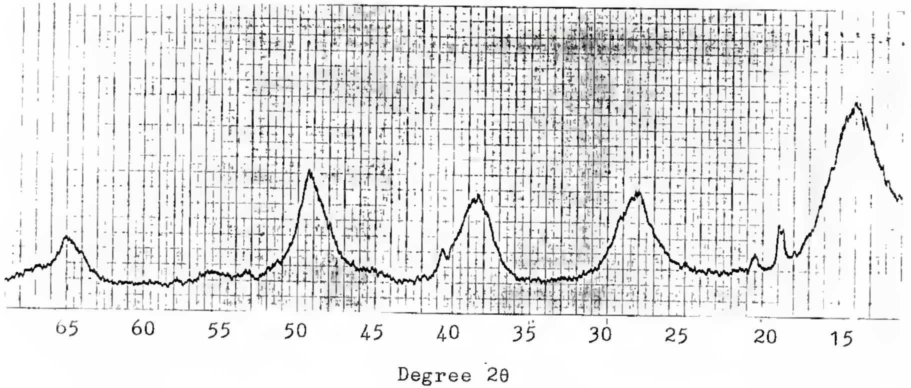

X-ray diffraction pattern of boehmite that was made by the procedure outlined in this work.

Figure 4.7.

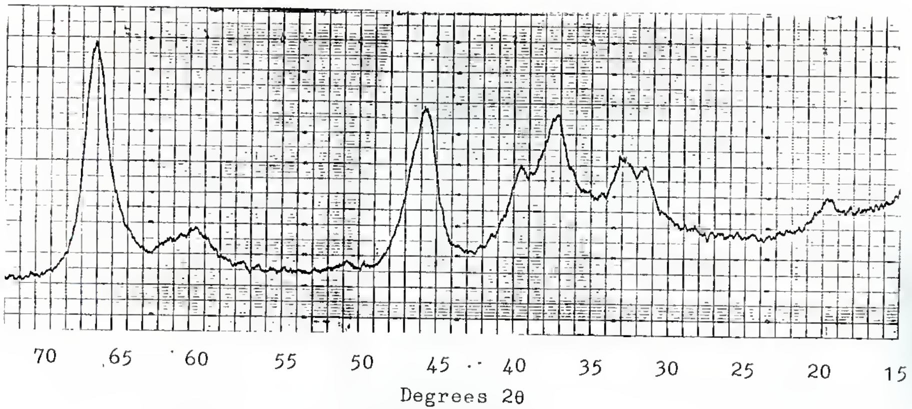

X-ray diffraction pattern of eta alumina obtained by heating bayerite at 550 C for 24 hours in air.

Figure 4.8

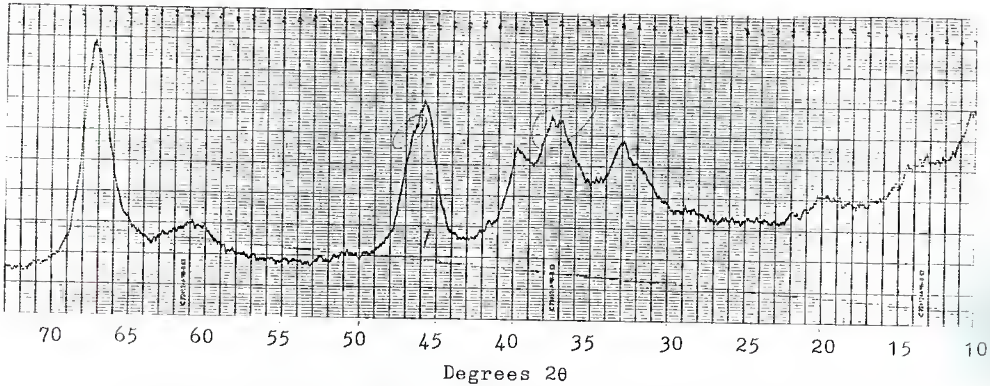

X-ray diffraction pattern of gamma alumina which is obtained by heating boehmite at 550 C for 24 hours.

Figure 4.9

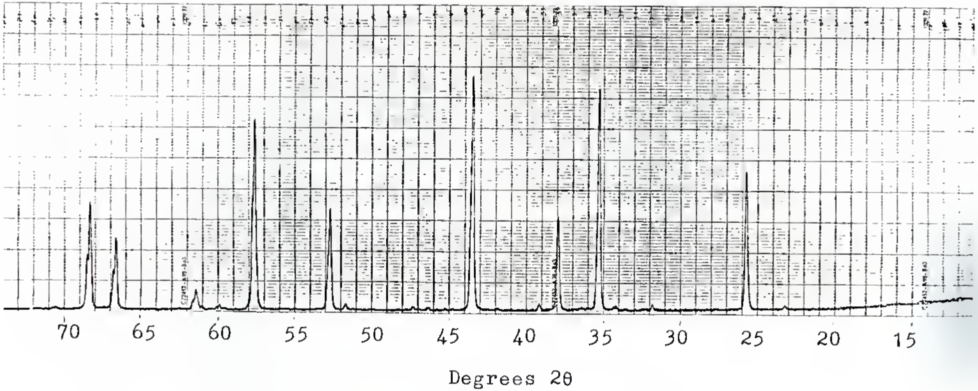

X-ray diffraction pattern of alpha alumina which was produced by heating boehmite at 1200 C for 24 hours.

Table 4.1 (6)
X-ray Powder Diffraction Patterns.
Interplanar Spacings and Relative Line Intensities.
Filtered CuK Radiation.

Gibbsite		Bayerite		Nordstrandite		Boehmite		Diaspore		Chi		Gamma		Eta		Delta		Delta		Theta		Iota		Kappa		Alpha	
4.82	100	4.72	100	4.790	10	6.11	100	4.71	13							5.02	3	7.97	8	5.2	3	5.45	100	6.2	3	3.479	74
4.34	40	4.36	70	4.373	2	3.164	65	3.99	100					4.6	4	4.55	3	6.58	10	4.5	6	3.47	90	4.5	2	2.552	92
4.30	20	3.19	25	4.310	4	2.346	53	3.214	10							4.07	2	5.07	20	3.53	2	2.92	40	4.2	1	2.379	42
3.35	10	3.08	1	4.205	4	1.980	6	2.558	30					2.8	2	2.87	4	4.05	20	2.85	8	2.72	80	3.04	4	2.165	1
3.31	6	2.69	3	4.153	4	1.860	32	2.434	3			2.7	2			2.73	8	3.56	7	2.72	8	2.59	70	2.79	6	2.085	100
3.17	8	2.45	3	3.880	3	1.850	27	2.386	5							2.58	3	3.40	10	2.56	3	2.46	10	2.70	2	1.740	43
3.08	4	2.34	6	3.600	3	1.770	6	2.356	8	2.40	4	2.41	6	2.40	6	2.43	6	3.28	15	2.43	8	2.34	40	2.57	8	1.601	81
2.44	15	2.28	3	3.462	2	1.662	13	2.317	56	2.27	2	2.28	6	2.27	3	2.28	4	3.21	10	2.31	6	2.24	80	2.41	3	1.546	3
2.42	4	2.21	67	3.022	2	1.527	6	2.131	52			2.18	2					3.03	10	2.24	6	2.15	60	2.32	4	1.510	7
2.37	20	2.14	3	2.815	2	1.453	16	2.077	39	2.11	3	2.09	1					2.783	30	2.11	1	1.99	10	2.26	1	1.404	32
2.28	4	2.06	2	2.706	1	1.434	9	1.901	3	1.98	2	1.98	10	1.97	8	1.99	8	2.737	30	2.01	8	1.94	10	2.16	1	1.374	48
2.23	6	1.97	3	2.490	1	1.412	1	1.815	8			1.95	6			1.95	3	2.593	70	1.91	4	1.88	40	2.11	8	1.276	2
2.15	8	1.91	1	2.478	3	1.396	2	1.733	3							1.91	2	2.457	70	1.80	3	1.73	50	2.06	3	1.289	16
2.03	12	1.83	1	2.451	2	1.383	6	1.712	15							1.80	2	2.311	40	1.73	1	1.61	40	1.99	4	1.190	6
1.98	10	1.76	1	2.390	7	1.369	2	1.678	3	1.53	1	1.54	2			1.54	4	2.277	30	1.61	2	1.55	70	1.95	2	1.160	1
1.95	2	1.71	26	2.261	7	1.312	15	1.633	43					1.52	2	1.51	3	2.156	25	1.54	6	1.492	30	1.87	6	1.147	4
1.90	7	1.68	2	2.217	1	1.303	3	1.608	12							1.49	4	1.989	70	1.49	4	1.461	40	1.82	3	1.138	1
1.79	10	1.64	1	2.029	1	1.224	1	1.570	4							1.45	3	1.950	65	1.45	4	1.435	10	1.74	2	1.125	5
1.74	9	1.59	4	2.013	5	1.209	2	1.522	6					1.40	10	1.40	6	1.793	7	1.43	1	1.410	10	1.64	6	1.099	6
1.67	9	1.56	2	1.898	5	1.178	3	1.480	20	1.39	10	1.39	10			1.39	10	1.701	4	1.40	6	1.370	10	1.54	1	1.083	3
1.65	3	1.55	4	1.777	4	1.171	1	1.431	7							1.29	2	1.616	10	1.39	10	1.346	40	1.49	3	1.078	7
1.63	1	1.52	1	1.717	1	1.161	3	1.423	12							1.26	1	1.602	15	1.34	1	1.325	5	1.45	3	1.043	13
1.58	3	1.48	1	1.698	1	1.134	5	1.400	6					1.21	1			1.543	10	1.29	3	1.288	60	1.43	8	1.018	1
1.57	1	1.47	1	1.680	1	1.092	1	1.376	16			1.14	3	1.14	2	1.14	2	1.507	20	1.26	2			1.39	10	.998	11
1.55	2	1.45	7	1.667	1	1.046	2	1.340	5			1.04	1	1.03	1			1.462	8	1.23	2			1.34	3	.982	2
				1.647	2													1.407	60								
				1.591	2													1.392	100								
				1.569	2													1.250	4								
				1.545	2													1.238	9								
				1.510	3													1.180	4								
				1.475	3													1.134	10								
				1.438	6																						
				1.400	2																						

CHAPTER 5

LITERATURE REVIEW ON PREPARATION OF ALUMINA

5.1 Introduction

There are three general techniques by which alumina is produced that are found in the literature:

1) Precipitation of alumina from aqueous solutions containing aluminum ions which are present from aluminum salts. e.g. $AlCl_3$, $AlSO_4$, etc. (6,7,20).

2) Pyrolysis of aluminum salts (20,21).

3) Reaction of amalgamated aluminum with liquid or vapor water (6,7,9,22,23,24).

In this work an amalgamation procedure was used to prepare the aluminas that are used. In light of this and because of the volumes that have been written on the other preparation techniques, only a review of the procedures dealing with the amalgamation process will be discussed here. Reviews of some of the many precipitation and pyrolysis preparation methods can be found in references 6,7,20. It should be noted that numerous references on the preparation of aluminas by precipitation techniques conflict with one another. These discrepancies occur because the product obtained by a given preparation method depends greatly on such conditions as starting materials, temperature, and impurities present.

5.2 Literature Review of Amalgamation Procedures

Amalgamated aluminum is aluminum that has been reacted with mercury. Under normal circumstances, a piece of aluminum exposed to air, has a stable, passive oxide layer which has been described as amorphous. This layer will form gelatinous products when reacted with water below the boiling point (6). The thickness of this passive layer has been estimated to vary between 20 and 100 Å depending on temperature and environment. Aluminum that is in this stable state cannot be wetted by contacting with mercury. If the passive layer is removed or cracked by an acid or base in the presence of mercury, then the surface of the aluminum can be wetted and an interaction takes place.

In 1870 Cossa found that a fibrous alumina gel was formed by the action of mercury and moisture on aluminum. It was found that at room temperature bayerite lines were present in diffraction patterns from this fibrous gel. Wislicenus in 1908 also formed fibrous alumina on the surface of amalgamated aluminum. This material was found to be composed of long fragile fibers of aluminum hydroxide. These fibers age rapidly in water forming a structure that is isomorphous and similar to a Ca gel. A Ca gel is amorphous to X-rays and corresponds to a trihydroxide in water content (6,7).

5.2-1 Bayerite Preparation

Schmah in 1946 treated amalgamated aluminum foil with water at room temperature and obtained bayerite with a sharp diffraction pattern (9). Lippens used Schmah's method in the following procedure to produce bayerite. Strips of very pure aluminum foil (99.99% pure) approximately, 10 cm. in length, 1.5 cm. wide, and 2 mm. thick were used. They were degreased with acetone, etched with 2 N sodium hydroxide for ten seconds and thoroughly rinsed with distilled water. Next, they were amalgamated by immersion for 2 seconds in a 1% mercury chloride solution in which the mercury is displaced from the solution and deposited on the surface of the aluminum metal (24).

The strips were then placed in porcelain disks containing 100 ml distilled water, brought to different pH's by adding NH_3 or by saturating with CO_2. The NH_3 served to raise the pH above 7, while the CO_2 lowered the pH. After a weeks time, during which the pH was kept constant by adding NH_3 if necessary, all of the aluminum was disolved, except that prepared with CO_2. The best results were obtained in water with a pH of 7. Lippens noted that the presence of electrolytes, like ammonium sulphate, slowed the formation of bayerite considerably, and in some cases gelatinous boehmite was formed. This was also confirmed by Lahondy-Sarc (24) in 1978.

In 1973 Bennet and Pinnel (22,23) reported a method of producing bayerite in which mercury metal was used. In this method a .25 g aluminum bar was lowered into a beaker containing mercury with a dilute solution of hydrochloric acid floating on top. The acid solution removed the normal passive layer on the aluminum and allowed the mercury to contact the "clean" surface. While the aluminum was still submersed in the mercury, the acid solution was flushed from the mercury with distilled water, which was then decanted off. The aluminum sample was removed from the mercury and placed in a clean beaker containing distilled water at room temperature.

Hydrogen gas was immediately released from the water as the amalgamated aluminum was placed in the water, but it took a day before the water became cloudy with the reaction product. After 460 hours, the remaining aluminum was removed from the beaker and the beaker, plus contents, allowed to evaporate to dryness at room temperature. The solid that was obtained from the beaker was found to be well crystallized bayerite.

The aluminum that was removed from the beaker was exposed to air and a white fibrous alumina product formed on the surface. This alumina product was found by Bennet and Pinnel to be gamma alumina (22,23).

5.2-2 Boehmite preparation

Boehmite can also be produced using an amalgamation process. Bennet and Pinnel (22,23) produced well crystallized boehmite using essentially the same procedure that they used for bayerite except that they placed the amalgamated aluminum in distilled water at 90°C rather than at room temperature. When this was carried out, there was vigourous evolution of hydrogen and immediate clouding of the water, indicating that the reaction was proceeding at a much faster rate than before. Also, all of the aluminum (.25 g bar) was consumed in a weeks time.

The beaker and its contents, were kept at 90°C until all the water had evaporated and a white powder that formed a cake that easily crumbled remained. The powder was found to be well crystallized boehmite.

O. Lahondny-Sarc et. al. (34) tried to produce well crystallized boehmite by degreasing aluminum metal in acetone, and amalgamating it in a saturated solution of mercury chloride. They placed newly treated aluminum samples in water kept at temperatures between 25 and 100°C. They reported that pseudoboehmite, or a mixture of pseudoboehmite and bayerite was produced at the higher temperatures and claimed that well crystallized boehmite could not be produced using this method.

5.3 The Role of the Mercury

The mechanism for the conversion of aluminum metal to alumina is not known, but the role of the mercury in this process has been investigated. Bennet and Pinnel (22,23) claim that the mercury acts as a catalyst and is therefore not consumed in the reaction. They point out that while liquid mercury is not soluble in solid aluminum, there is a small solubility of aluminum in liquid mercury. (approxmately .002 wt.% at room temperature). Therefore at room temperature (25°C) at the mercury-aluminum interface an equilibrium exists between a very dilute solution of aluminum in mercury and pure solid aluminum.

It is also pointed out that it is thermodynamically more favorable for the aluminum to exist as an oxide or hydroxide rather than as a free atom in the mercury. See

Table 5.1. Hence, at the mercury-water interface aluminum atoms are removed from the mercury, while at the mercury-aluminum interface aluminum atoms are going into solution to try to maintain equilibrium.

Table 5.1.

Heats of formation and free energies for the aluminum compounds Al_2O_3, $Al(OH)_3$ and water (22).

	ΔH(f) Kcal/mol	ΔG(f) Kcal/mol
Al_2O_3 (corundum)	-399.9	-376.87
$Al(OH)_3$	-304.8	-272.90
$H_2O_{(l)}$	-68.32	-56.69

The function of the mercury seems to be threefold: First, it seems to keep the aluminum surface active by preventing the formation of the passive layer on the surface of the aluminum. Secondly, its phase equilibrium requirements serve to remove aluminum atoms from the bulk aluminum. Thirdly, since mercury is liquid at room temperature, it serves as a rapid transport medium to bring the aluminum atoms to the mercury-water interface. Mercury acting in this way is not depleted in the formation of the aluminum oxide or hydroxide, and therefore plays a catalytic role. See Figure 5.1.

Lahodny-Sarc et. al. (24) proposed a different explanation of the role of the mercury. They stated that because of the large differences in the electrochemical

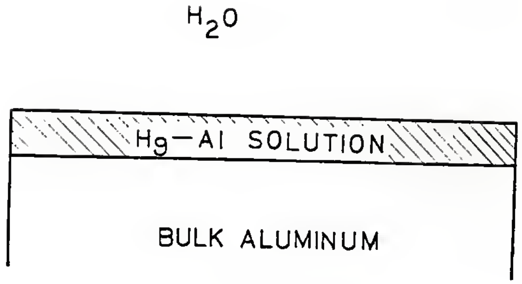

Figure 5.1. A possible catalytic role of mercury in the reaction between aluminum and water. Aluminum enters the mercury at the mercury - aluminum interface and forms a solution with the mercury. The aluminum reacts with the water at the mercury - water interface.

potentials between the aluminum and the mercury, local electromotive cells are formed. The resulting anodic dissolution then produces aluminum ions which react with hydroxyl ions from the water to form the aluminum hydroxide. Hydrogen ions are discharged at the sites where the amalgamation is formed and the hydrogen ions combine to produce H_2 gas or form a hydride. See Figure 5.2.

It is not known at this time which of these theories is correct in explaining the role of the mercury. It is possible however, that both of these ideas could be used to explain the observed behavior by occuring at the same time.

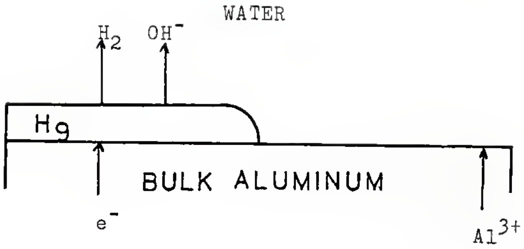

Anode $Al \rightarrow Al^{3+} + 3e^-$

Cathode $3H_2O + 3e^- \rightarrow 3OH^- + \frac{3}{2}H_2$

Figure 5.2. A possible explanation for the role of the mercury in promoting the reaction between aluminum and water. The mercury on the aluminum creates a potential and the above reactions are carried out. The aluminum is the anode and the mercury the cathode.

CHAPTER 6

LITERATURE REVIEW OF CARBON MONOXIDE ADSORPTION ON ALUMINA

6.1 Introduction

It should be noted from the onset that the literature review of CO and CO_2 adsorbed on alumina, while helpful and of definite interest, may not be directly applicable to the system studied in this work. In the literature the adsorbed species were examined at elevated temperatures and low pressures (less than 50 torr), or at room temperature and low pressures. The system that was used for this work utilized CO at atmospheric pressures and elevated temperatures (450 - 700°C). Because of the drastic differences in conditions between the literature experiments and those performed here, the information obtained from the literature should be examined carefully, keeping in mind that other phenomena, than what was seen in the literature, may be occuring at the new conditions.

6.2 Literature review

Several authors have investigated the adsorption of CO and CO_2 on alumina by using infrared techniques (25,26,27, 28,30,31,32,33). The authors are in general agreement that adsorbed CO and CO_2 form some of the same surface species. There is some difference in the assignment of the infrared data to surface species.

N. D. Parkyns reported on the adsorption of CO and CO_2 in two separate papers (26,27). He confirmed that CO adsorbed on a sample cf gamma alumina that was degassed at 400° C for 16 - 20 hours and then equilibrated with 15 - 35 torr of CO at room temperature is characterized by a fairly sharp band, of medium intensity, near 2000 cm^{-1}. These results had been reported earlier by Amberg and his coworkers (25). Amberg concluded that the band should be assigned to a dipole type interaction as shown below.

$$-Al^{+} - O^{-} ---- C^{+} = O^{-}$$

When the sample treated by Parkyns was allowed to stand for a few hours in contact with the CO, other bands at 3605, 1640, 1480, and 1233 cm^{-1} appeared. Parkyns stated that the bands below 2000 cm^{-1} are due to adsorbed CO_2. To ensure that the CO_2 formation was not a result of a reaction between CO and adsorbed molecular oxygen, alumina was degassed as before and then reduced with 20 torr hydrogen at 400° C for 1 hour, after which the excess was evacuated. On leaving the "reduced" alumina stand in contact with CO, the same phenomena was noted after a few hours. However, this time the bands at 3605, 1800, 1640 and 1233 cm^{-1} increased in intensity to a maximum after 48 hours. Treating the samples with deuterium instead of hydrogen had no effect on the frequencies of the adsorbed CO band (ie 2200 cm^{-1}), but some of the other frequencies attributed to adsorbed CO_2 were lowered.

When an alumina sample was degassed at 400° C for extended periods of time (6 days) and allowed to adsorbed CO, only the 2200 cm^{-1} band was observed and no others. However, on standing in contact with the CO, the other bands appeared.

The bands at 3605, 1800, 1640, and 1233 cm^{-1} are characterized by Parkyns to by CO_2 strongly adsorbed in at least two and possibly 3 distinct ways.

Parkyns postulated that the adsorbed CO_2 could be accounted for by two possible mechanisms: 1. Disproportionation of CO to give CO_2 according to the Boudouard reaction. That is, $2CO = C + CO_2$. 2. Oxidation of adsorbed CO by some oxygen containing species either preadsorbed on the surface or coming from the surface itself.

Parkyns believed that both mechanisms operated but that the Boudouard reaction is much slower. For example, a sample of alumina which had been degassed for extended periods or reduced with hydrogen, although initially free of CO_2 bands, when treated with CO, developed them after a few hours. The reaction could be speeded by heating the system to 200° C. Although, the presence of carbon produced by the Boudouard reaction had not been explicitly proven, samples treated in this manner developed a light brown color, which was removed by heating them in oxygen. On the other hand, an oxidation mechanism must be invoked to explain the almost instantaneous appearance of CO_2 bands on the addition of CO to alumina that was only partially degassed (16 - 24 hours at 400° C)

CHAPTER 7

EXPERIMENTAL

7.1 Production of Alumina

The alumina that was used in this work was prepared from aluminum metal using a process similar to that of Bennet and Pinnel (22). Aluminum metal, in foil form, (99.99% pure) from Allied Chemical was cut into approximately one inch squares. Next, about 15 grams of the metal squares were lowered into a beaker containing clean mercury with a dilute solution of hydrochloric acid floating on the mercury. The acid solution was prepared with 4 parts distilled water to 1 part concentrated hydrochloric acid by volume. The aluminum metal pieces were kept submerged in the mercury, while the acid layer was decanted from atop the mercury. The mercury was then rinsed with distilled water leaving a clean distilled water layer in place of the acid layer. The aluminum metal was removed from the mercury, and placed in a clean beaker containing water either at room temperature or above 90° C which produced bayerite or boehmite respectively.

The aluminum placed in the water at room temperature seemed to react very slowly at first. Small bubbles of what is believed to by hydrogen, formed on the aluminum surface and rose to the surface of the water. The rate of formation of the bubbles steadily increased and after a few hours (2 - 4) the water became gray with the reaction product. It was noticed that the temperature of the water had increased slightly during that time and only very small pieces of aluminum were left. After appoximately two additional hours, the small pieces of aluminum were also dissolved and the liquid remained an opaque gray. Upon standing overnight, the contents of the beaker had changed color from a dark gray to a gray shaded white. The contents were allowed to evaporate to dryness, at room temperature, forming a white powdery cake that crumbled easily in the bottom of the beaker. The white substance was found to be bayerite alumina by x-ray diffraction. See Figure 4.5. The bayerite was then calcined in air at 550° C for 24 hours to produce eta alumina, which also verified by x-ray diffraction. See Figure 4.7.

The aluminum that was placed in water between 90 and 100° C reacted much more rapidly than that placed in room temperature water. In the higher temperature water, there was an immediate evolution of gasses from the surface of the aluminum. The water became cloudy and opaque gray within approximately 30 minutes. Almost all of the aluminum metal pieces were dissolved in about an hour and the evolution of gasses stopped. The beaker and its contents were then placed in an oven at approximately 94° C. A glass plate was placed over the beaker overnight to prevent the rapid evaporation of the water. By the next morning, the contents of the beaker had changed color from an opaque gray to white. The glass plate was removed and the contents allowed to evaporate to dryness which took 2 days. The product that was obtained formed a white powder in the bottom of the beaker which was found to be boehmite by x-ray diffraction. See Figure 4.6. The boehmite was heated for 24 hours, in air, at 550° C to produce gamma alumina. See Figure 4.8.

It should by noted that in both the preparation of bayerite and boehmite, a small amout of mercury, which had adheared to the aluminum metal surface, was present in the beaker after all the aluminum was dissolved and the beaker still contained liquid. This mercury was removed from the product by decanting off as much of the aqueous phase as possible. The beaker and the remaining mercury were rinsed with distilled water several times, each time decanting the water into the original product liquid. Finally, after all the reaction products had been rinsed from the beaker and only the mercury remained, the mercury was added to the bulk mercury used in the process. It is not believed that mercury was present in the products bayerite or boehmite, however, no tests were made to confirm this.

The calcining of the bayerite and boehmite were performed in a muffle furnace, in air. The aluminas were placed in ceramic crucibles during the heating. After the calcination, the resulting eta and gamma alumina were stored in a desiccator with calcium sulfate as the desiccant to reduce the adsorption of water from the air by the aluminas.

The structural determination of the aluminas in this work was performed using a Semiens Crystoflex 4 X-ray

Diffractometer. Copper radiation at 40 kV and 18 ma were used for all of the samples. The sweep speed through the angles of interest was 1 degree (2θ) per minute. The samples were mounted in a glass holder that was made and found to by amorphous to x-rays. The diffraction patterns seen in Figures 4.5 to 4.9 are from alumina used in this work. A short instructional section on how to set up the equipment to obtain a diffraction pattern can be found in the appendix.

7.2 Choosing the Reactor

The reaction of CO with alumina studied in this work, was investigated using a differential plug flow reactor. With a differential reactor the reaction is carried out so that it can be assumed that the reaction conditions are the same throughout the bed. In other words, the catalyst at the end of the reactor is surrounded by the same environment as the catlyst at the beginning of the bed. In order for this assumption to approach reality, the reactor must be operated so that the extent of reaction is low, making the composition of the gas stream at the end of the catalyst bed only slightly different from that at the front.

The differential plug flow reactor was chosen for this work over the integral reactor because, with the differential reactor, a value for the rate of reaction could by obtained directly from experimental data without having to assume anything about the reaction mechanism. That is, rate verses time or carbon content data was obtained and then the reaction kinetics were assumed and tested to see if the data obtained could be explained in terms of the assumed kinetics. If the integral plug flow reactor were used, a reaction mechanism would need to be assumed and somehow integrated over the length of the catalyst bed and an exit concentration calculated based on the assumed model. Then the calculated exit composition would be compared to the experimental results to determine if the assumption was correct. A value for the rate of reaction would not be available until after the mechanism was assumed. Therefore, the only data obtained directly by the integral reactor would be the extent of conversion.

The differential analysis of the reactor which will be described in detail later is summarized below. The equation used to calculate the rate was derived for the general case of a mixture of CO and CO_2 being fed to the reactor. The only components assumed to be exiting the reactor were CO and CO_2. The composition of exit stream was different from the inlet because of the disproportionation reaction. The next step in the development of an expression relating the exit composition to the rate of reaction was to make an oxygen balance around the reactor. This related the molar flow rate into the reactor to the molar flow rate out of the reactor according to the relation

$$W_{out} = \frac{W_{in}\ (2 - x)}{(2-y)} \qquad 7.1$$

where

W_{out} = The total molar flow rate out of the reactor
W_{in} = The total molar flow rate into the reactor
x = The mole fraction of CO entering the reactor
y = The mole fraction of CO leaving the reactor

Next, a CO balance was performed on the system which yielded the following relation.

$$xW_{in} - yW_{out} - rM_{cat} = 0 \qquad 7.2$$

where

r = The rate of reaction of CO per unit mass of catalyst
M_{cat} = The mass of catalyst present in the reactor.

The result of substituting for the molar flow rate exiting the reactor with the earlier expression, and rearranging can be found in equation 7.3.

$$r = \frac{W_{in}}{M_{cat}} \left[x - \frac{y(2 - x)}{(2 - y)} \right] \qquad 7.3$$

Equation 7.3 is the one used to calculate the rate of reaction from the compositions of the inlet and outlet streams, the inlet total molar flow rate, and the mass of alumina used. This derivation can be seen in more detail in the appendix.

7.3 Equipment

In this work, the reactor used was a vycor tube made of 96% silica. The tube was 15 mm O.D. with an approximate wall thickness of 1.2 mm and was obtained from Fisher Scientific Co.. It was capable of withstanding temperatures up to 900° C. Other reactors constructed with metal or other glass were not used because of the temperatures involved and because iron, copper, nickel, and other metals are known to catalyze the disproportionation of CO at rates substantially higher than those obtained from alumina. The vycor tubing that was used has been found to catalyze the disproportionation reaction at a rate much lower than that of alumina (34). Because it was known to catalyze the reaction of interest, blanks were run on the tube and quartz wool that were used. This will be discussed in more detail below.

Quartz wool, obtained from Quartz Scientific, was used to hold the alumina in place in the tube. Quartz wool had to be used instead of glass wool because, at the operating temperatures between 450 and 700° C, it was found that the glass wool melted, plugging the reactor and coating the catalyst. No problem of that type was encountered with the quartz wool.

The gasses that were used in this work were carbon monoxide, carbon dioxide, and helium. The CO and CO_2 were supplied by Matheson. The CO was Ultra High Purity grade (99.8%), while the CO_2 was Coleman purity (99.99%). No further purification of the gasses was performed.

Analysis of the gasses in this work were performed on a Packard 427 gas chromatograph with a thermal conductivity detector. Helium was used as the carrier gas and a 6 foot ¼ inch I.D. column packed with Propak Q 100/120 was used for the separation of the constituents. All analysis were performed with the temperature of the chromatograph maintained at a constant 150° C. The retension times for CO and CO_2 were 1.3 and 2.8 minutes respectively. No overlap was found to exist between the CO and CO_2 peaks. The gas samples were obtained using a gas syringe. Sample sizes of .3ml were used.

Calibration of the chromatograph was accomplished by sampling a flowing stream of known CO and CO_2 composition. Next the ratio of the height of the CO peak to that of the sum of the heights of the CO and CO_2 peaks was found. This was done for a variety of compositions. A linear correlation was found to exist between the mole fraction of CO and the fraction of CO peak height. See Figures 7.1 and 7.2.

Two different calibrations using this method were made. One in which the entire range of CO and CO_2 compositions were used and the attenuation of the chromatograph was kept at 128 for both the CO and the CO_2 peaks. See Figure 7.1. After it was determined that the range of interest was between 92% and 100% CO mole fractions, a second calibration was performed where the attenuation was set at 128 for the CO peak and changed to 8 for the CO_2 peak. See Figure 7.2. This was done to increase the size of the CO_2 peak so that an accurate measurement could be obtained. The attenuation factor between attenuations of 8 and 128 was found to be 16.064. A detailed description of the steps used to obtain the calibration curves, and

Figure 7.1.

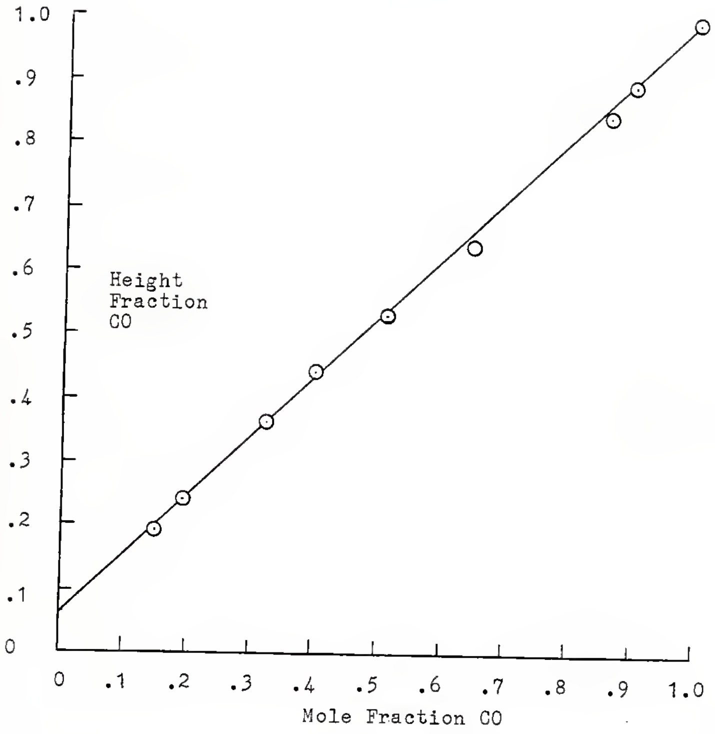

Calibration curve for the gas chromatograph over the entire concentration of CO and CO_2.

Figure 7.2.

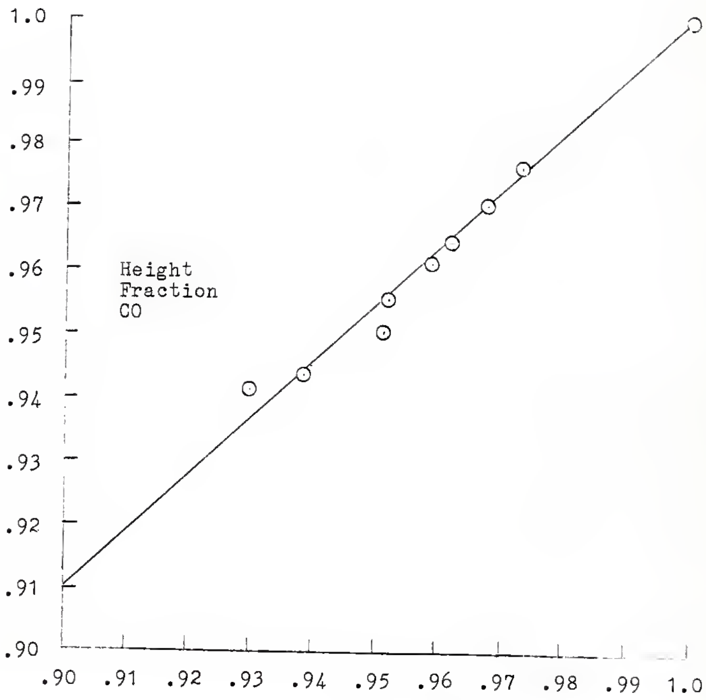

Mole Fraction CO

Second calibration of gas chormatograph in which the attenuation was change between the CO and CO_2 peaks.

the attenuation factor may be found in the appendix.

7.4 The Initial Reactor Configuration

For the initial experiments, a configuration shown in Figure 7.3 was used to carry out the reaction. Gamma alumina was used because the preparation process was much shorter than for eta alumina, and in the first few experiments quantities up to 12 grams were used in a single experiment. In these first experiments two tubular heaters were used. Inside the section of vycor tubing that would be inside the first tube heater, quartz wool was packed to attempt to heat the entering gasses to the desired temperature before they reached the catalyst. In the section of the tube in the second tube heater the catalyst, sieved to between mesh size numbers 12 and 40, was placed between two quartz wool plugs as shown in Figure 7.3.

When pure CO was used as the reactant stream at a flow of .6879 cm^3/sec. and 10.8472 grams of catalyst was used the initial mole fraction of CO_2 in the exist stream was approximately .0721 with a reactor temperature of 596° C. When a blank was run at these conditions with only the quartz wool present in the reactor, no CO_2 could be detected by the chromatograph when the attenuation was at 128 for both peaks, the setting for which the runs were made.

The procedure to make the experimental runs were as follows: First, the vycor tube was washed with soap and water and dried by slowly passing it through the tubular furnaces which were at the reaction temperature. Second, a

Figure 7.3.

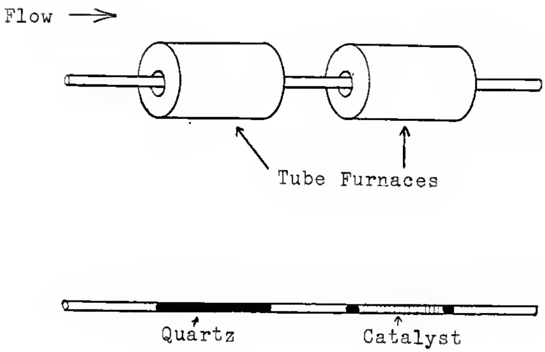

Initial reactor arrangement in which two tube furnaces are used. Quartz wool was used in the first tube furnace and was used to hold the catalst in place in the second reactor.

wool plug and a known weight of catalyst were loaded into the tube. Then the quartz wool used in the lead tube heater was placed in the tube and the tube positioned in the heaters. Helium was connected to the tube to purge the system of all air . Air was found to have the same retention time as CO making the analysis difficult if the system was not purged with helium. Helium, since it was used as the carrier gas in the chromatograph, did not produce a peak on the analysis. The system was purged for 1 to 2 hours until the tube and heaters reached thermal equilibrium. Finally, gas entering the reactor was switched to pure CO and a timer started. Samples were taken of the exit gasses and the time of sampling recorded.

The results from the initial experiments where different amounts of catalyst were used under approximately the same reaction conditions, indicated that the reaction was taking place in only a small portion of the bed. This conclusion was reached because the rate was found to be inversely proportional with the mass of catalyst used. See Figure 7.4. In other words, the rate seemed to increase when the amount of catalyst used was decreased and the temperature remained nearly constant. If all of the catalyst were used the rate of reaction would have remained nearly constant as the amount of catalyst used was varied at the same temperature. Because of this phenomena, smaller amounts of catalyst were used in the hopes of reaching the point where the entire catalyst bed was participating in the reaction.

Figure 7.4.

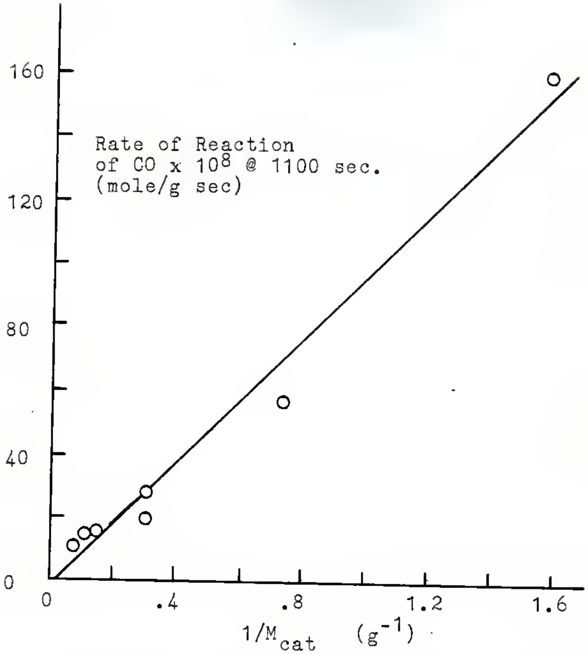

Phenomena that was experienced with the first reactor arrangement and large catalyst particles.

Amounts as low as .2 grams were used, but the phenomena persisted.

7.5 The Final Reactor Configuration

In an attempt to alleviate this problem, the catalyst was ground into smaller particles using a mortar and pestle. The particles were then sieved using a mesh size number 270 with a 53 micron nominal opening. This was done to reduce the possibility that diffusion into or out of the catalyst limited the rate of reaction. Also, the flow rate of CO was slowed to between 0.1 and 0.3 cm^3/sec to keep the conversion high enough to be accurately measured when the small amounts of catalyst were used.

The configuration of the catalyst in the reactor was also changed. Instead of having plugs of quartz wool and a bed of alumina, as before, the small alumina particles were distributed evenly throughout the reactor supported on the quartz wool. This new arrangement helped to ensure that all of the particles were surrounded by the same reaction conditions by preventing the black carbon front from forming at the entrance of the catalyst bed.

At the same time only one tube furnace was used to heat the tube and contents. See Figure 7.5. With lower flow rates, and amounts or catalyst, it was felt that better control over the reaction temperature could be obtained using only one tube furnace. Also, at this low flow rate of CO, it was found that the disproportionation reaction was promoted slightly by the quartz wool. This too played a

Figure 7.5.

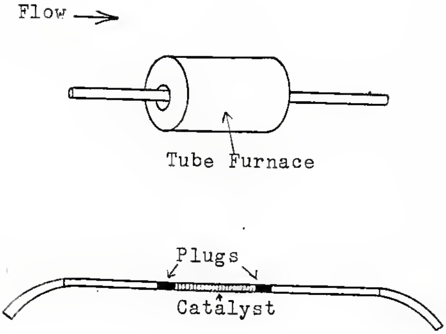

Second reactor arrangement that was used to obtain the reaction rates found in this work.

role in the reactor arrangement change, since the exact concentration of the gas stream entering the catalyst bed could not be known if two heaters were used. Because the wool was found to catalyze the reaction, blanks were run at the reaction conditions studied to determine the extent of the reaction caused by the wool. This amount was then subtracted from the results obtained when catalyst and quartz and wool were used to determine the extent of reaction produced from the catalyst only. The concentration of CO_2 that was found during the blank runs and used in the calculations can be found with tabulated data for the runs in the appendix.

Because of the small amount of catalyst present, (.3 to .5 grams) and the low conversion, (less than 2%) the attenuation of the gas chromatograph had to be changed between the CO and CO_2 peaks. The attenuation was left on 128 for the CO peak, but changed to 8 for the CO_2 peak. This change was necessary to accurately analyze the exit gas concentrations.

7.6 Experimental Procedure

The final procedure that was followed to obtain the data that was used for analysis in the results section of this work was as follows: First, the tube heater was preheated to the reaction temperature and allowed to stablize with an empty vycor tube mounted inside. The temperature of the furnace was found using an iron-constantan thermocouple that was placed in the center of the furnace but outside of the reactor. Next, the vycor tube was washed and dried thoroughly to ensure that no water was left inside the tube. A known amount of catalyst that had been screened to below a mesh size number 270 was weighed out. Then, a glass funnel was placed in one end of the tube as shown in Figure 7.6. A small amount of quartz wool was placed in the funnel and pushed into the tube to form a quartz plug so the catalyst would not fall or be blown out of the tube. Again, a small amount of quartz wool was placed in the funnel and some of the measured catalyst was carefully distributed over the wool so that the catalyst was evenly covered by the quartz wool. Any catalyst that happened to fall through the wool in the funnel fell into the reactor onto the wool already in the tube. The catalyst covered wool was gently pushed into the tube. This step was repeated until all of the weighed catalyst was in the reactor. The length of the wool-supported catalyst was approximately 8 cm. A leading quartz wool plug was placed in the tube. The tube furnace was 16 cm in length, and the reactor tube was placed in the furnace such that the catalyst was centered inside the furnace.

Two sections of plastic tubing were placed on the ends of the vycor tube so that they were curved downward as shown in Figure 7.5. This was to make connection of gasses to the reactor easier and to try to reduce any natural convection by forcing the heated gasses in the reactor down before they were allowed to leave the reactor. The reactor was purged with helium at a flow rate of 5 cm^3/sec. The purge was left on at least one hour or until the furnace and the reactor had reached thermal equilibrium. It had been found earlier that at the low gas flow rates through the reactor, the temperature inside the reactor was the same as that inside the furnace but outside the reactor. This was found by placing one thermocouple inside the tube under reaction conditions and another inside the furnace but outside the reactor. The temperature was the same for both thermocouples. Thermal equilibrium was considered complete when the temperature inside the furnace had returned to the value it was when it was stablized with the empty vycor tube inside.

After the reactor and contents had reached thermal equilibrium, the helium flow was stopped and a pre-measured flow of CO was connected to the reactor. As soon as the CO flow was connected, a timer was started. 0.3 ml samples were taken of the exit gasses using a gas syringe. The sample was immediately analyzed on the gas chromatograph, and the time the sample was taken recorded. A summary of the conditions that were studied using this procedure can be found in Table 7.1. A blank run, using quartz wool but no catalyst was made for all the conditions studied except for the experiment carried out at 700°C. When the blank runs were carried out, everything was kept the same as the experimental run but this time only quartz wool was located in the reactor. No catalyst was placed in the reactor.

The CO flow rate was determined using a bubble flow meter as shown in Figure 7.7. The time needed for a bubble to pass between the two etched marks on the flow meter was recorded. The volume between the etched marks had been very accurately determined by Handa (34) and was found to be 20.0699 cm^3. Therefore, the flow rate could be found by dividing 20.0699 by the time needed for the bubble to traverse the distance. The average of several timings were used to compute the flow rates. The temperature and atmospheric pressure prevailing at the time of the flow measurement were recorded so the molar flow rate could be calculated.

All of the gamma alumina that was used with the final reactor scheme was obtained from the same batch. This was to ensure that the surface area and pore size were the same for all of the experiments. The surface area of the gamma alumina was determined using a Perkin-Elmer Shell Model 212 Sorptometer which utilizes continuous flow techniques. The surface area was determined at liquid nitrogen temperatures by physical adsorption of nitrogen onto the alumina. Then the model put forth by Brunauer, Emmett and Teller (BET) was used to determine the specific surface area. The surface area for the gamma alumina used in the final reactor scheme was 94.8 m^2/g. A full description of the instrument and the theory that was used to obtain the surface area measurment can be found in references 34 and 35.

Figure 7.6.

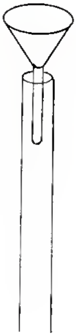

The arrangement of the funnel and the vycor tube that was used to load the catalyst into the reactor mixed with quartz wool.

Figure 7.7.

The bubble flow meter that was used to measure the flow rate of CO that was fed to the reactor.

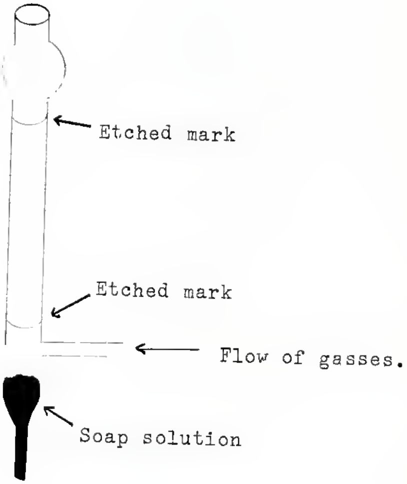

CHAPTER 8

RESULTS AND DISCUSSION

8.1 First Reactor Arrangement

As stated earlier in the experimental procedure, two different reactor arrangements were used in this work. The results obtained from the first reactor arrangement will be discussed first. At the onset of this work, the goal was to obtain rate verses time, or carbon content data for the disproportionation reaction $2CO = CO_2 + C$, on alumina. The data was to be extrapolated back to obtain the initial rate for different temperatures so an Arrhenius plot could be made. Because of this outlook, the experiments in which the first reactor arrangement was used were only conducted for approximately two hours, sampling every 3 to 5 minutes.

To ensure that the reaction rate was not limited by transport limitations, runs were made at the same temperature but with different flow rates of reactants and different amounts of catalyst. The results obtained indicated that changing the amount of catalyst had a marked effect on the rate that was obtained. As the amount of catalyst decreased the rate of reaction increased. A plot of the rate of reaction taken at 1100 seconds verses the inverse of the mass of catalyst showed the relationship that was present. See Figure 7.4. These resultss indicated that only a small portion of the catalyst was participating in the reaction. Visual inspections of the catalyst bed after an experimental run was completed, revealed that a small section, 1 to 2 mm in length, at the beginning of the bed, was considerably darker than the rest of the catalyst. The remainder of the catalyst bed had become gray from its initial white.

Because of this, it was speculated that the majority of the disproportionation was occuring at the entrance of the catalyst bed. The exact reason for this phenomena has not been determined. However, it was theorized that the initial portion of the catalyst bed reacted more than the remainder of the catalyst because it did not encounter any of the products of the reaction that the catalyst downstream did. The CO_2 that was present downstream of the initial section could have inhibited the disproportionation by preferentially adsorbing on active sites, or by promoting the reverse reaction thereby removing any carbon that was deposited. It should be noted that at the temperatures used, 450 to 700°C, the equilibrium requirements for the system are such that the reaction should go to completion for all of the temperatures used except 700°C. At 700° C the change in the free energy of the disproportionation reaction is found to be positive indicating that at equilibrium little of the CO should react. See Table 8.1 for a summary of the equilibrium constant as a function of temperature for this system.

Both of the theories suggest that if the reaction was

Table 8.1

Thermodynamic data for the reaction

$2CO \rightarrow CO_2 + C$.

Temp. (^{o}C)	ΔH_{rxn} (cal/mol)	ΔG_{rxn} (cal/mol)	Equil. Const.
0	-41134	-29674	5.551×10^{23}
15.56	-41185	-29024	9.389×10^{21}
25.00	-41214	-28626	9.664×10^{20}
37.78	-41250	-28087	5.543×10^{19}
93.33	-41377	-25728	2.209×10^{15}
204.44	-41490	-21632	7.955×10^{9}
315.56	-41465	-16206	1.039×10^{6}
426.67	-41348	-11449	3.765×10^{3}
537.78	-41167	-6718	6.467×10^{1}
648.89	-40945	2013	3.333×10^{-1}
760.00	-40698	2667	2.727×10^{-1}
871.11	-40431	7317	4.003×10^{-2}
982.22	-40144	11942	8.333×10^{-3}
1093.33	-39842	16537	2.224×10^{-3}

From reference 40.

left to proceed for a long period of time, a dark front would migrate down the catalyst bed. To investigate this an experiment was conducted for approximately 159 hours. During this experiment, the catalyst was examined by sliding the vycor tube out of the tube heater for a moment, and then sliding it back. The flow of CO to the catalyst was not interrupted when the catalyst was viewed in this manner. It was observed that a dark section again formed at the beginning of the catalyst bed. As the reaction continued, the catalyst behind the initial dark section slowly became darker, and a dark front on the catalyst slowly moved down the bed. This evidence, while not proving the explanations given, indicated that a localized phenomena was indeed occuring and not all of the catalyst was participating fully in the reaction.

Based on this result, it was thought that if a small enough amount of catalyst was used, all of it would by used to promote the disproportionation reaction. Therefore, smaller amounts of catalyst were used. Amounts ranging from 12 to approximately 0.3 grams were used but the phenomena persisted.

8.2 Second Reactor Arrangement

In an attempt to alleviate this localized reaction phenomena, the gamma alumina that was used as the catalyst was ground into smaller particles and screened to mesh number 270 which has a nominal opening of 53 microns. Also, the catalyst was not placed in the reactor as before but was spread throughout the reactor by diluting it with quartz wool. Thus the second reactor configuration described in the procedure was used. See Figure 7.5.

Because of the dilution of the catalyst with quartz wool used in the second reactor arrangement, only small amounts of catalyst could by used (.2 to .4 g). Also the flow rate of CO had to be reduced to keep the concentration of CO_2 in the exitings gases high enough to be measured with confidence. To see if the new arrangement eliminated the localized phenomena, two experiments were made using different amounts of catalyst. The results are shown below.

	Run 33	Run 34
Temperature	505°C	494°C
Flow rate CO	.1421 cm^3/sec	.1974 cm^3/sec
Mass of catalyst	.2230 g	.4404 g
Rate after 2 hours in mol/g sec	49.04×10^8	50.08×10^8

Because the rates were approximately the same for different amounts of catalyst it was thought that all of the catalyst was participating in the reaction and a satisfactory reactor arrangement had been found.

8.3 Data From Experiments

Using the second reactor arrangement, experiments using gamma alumina were conducted at 500, 550, 600, and 700° C. Also, an experiment was conducted using eta alumina at 500° C. A summary of the conditions studied using this arrangement, can be seen in Table 8.2. The length of time that each experiment was conducted was increased to over 100 hours with multiple samples being taken at every sampling time. The exit stream was sampled at least every few hours. The length of the experiments was increased to study the behavior of the reaction at longer times. The results of the multiple samples were averaged to obtain one data point for each sample time. The results of the experiments can be seen in Figures 8.1 to 8.6. Sample calculations and tabulated data of the results can be seen in the appendix.

As shown in Table 8.2, runs 35 and 39 were carried out at nearly the same conditions, and the results from these two runs were nearly identical. This indicated that the result could be reproduced and the phenomena being studied was real. However it should be noted that after run 43 an experiment at 450° C using gamma alumina was attempted which yielded rates that were far lower than those experienced earlier. A check was then made to see if the results of runs 35 and 39 could again be duplicated. This was unsuccessful. The rates that were obtained were well below those obtained even at 500° C earlier. Based on these results it was concluded that the catalyst had somehow changed. Exactly how the catalyst changed is not known, but a possibility is that the alumina irreversibly adsorbed something from the atmosphere which changed its reactivity. The gamma alumina that was used in all of the runs using the second reactor arrangement was from the same

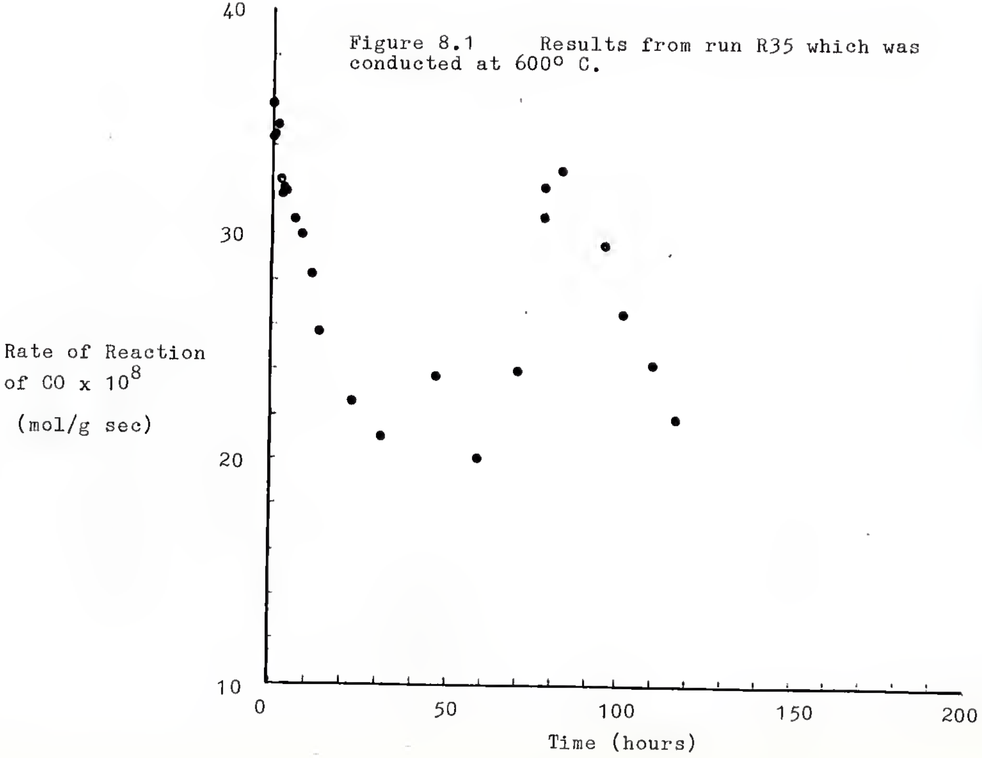

Figure 8.1 Results from run R35 which was conducted at 600° C.

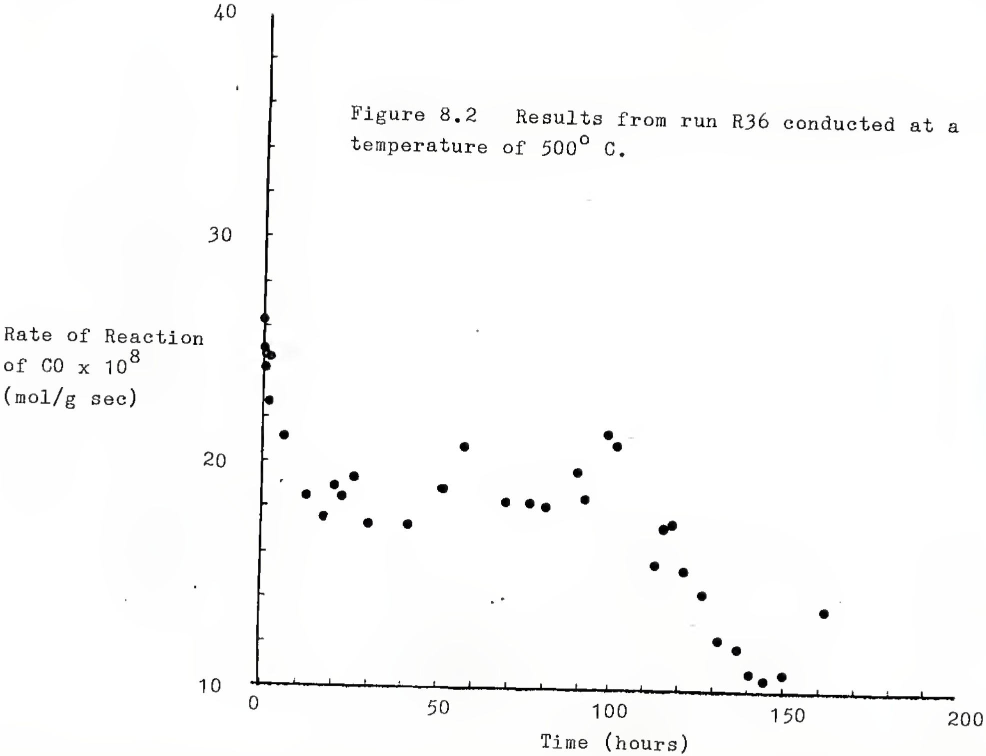

Figure 8.2 Results from run R36 conducted at a temperature of 500° C.

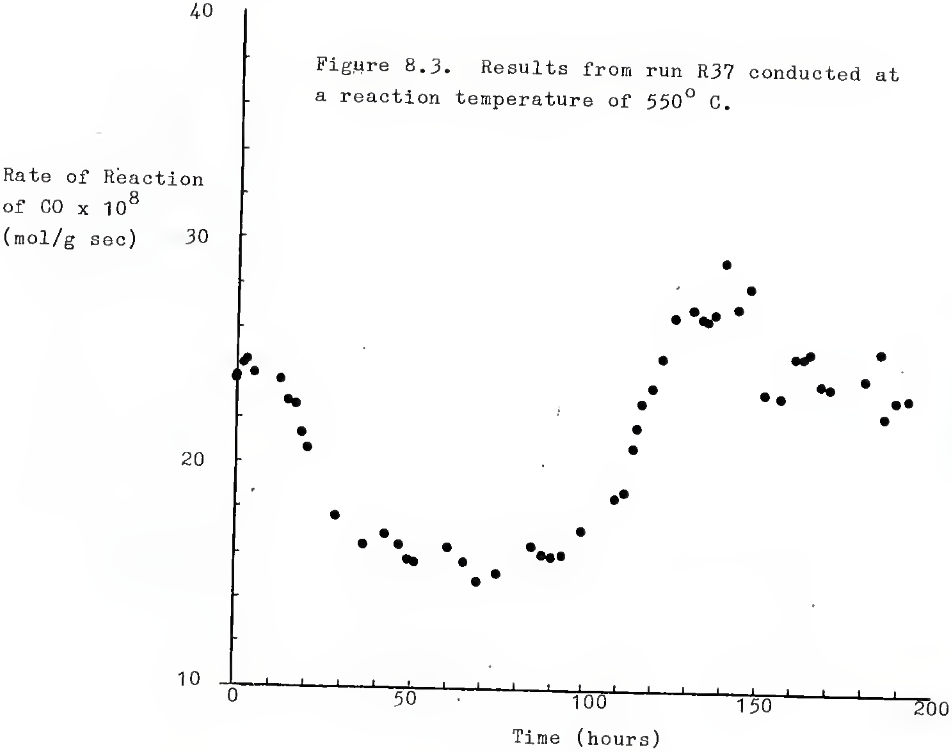

Figure 8.3. Results from run R37 conducted at a reaction temperature of 550° C.

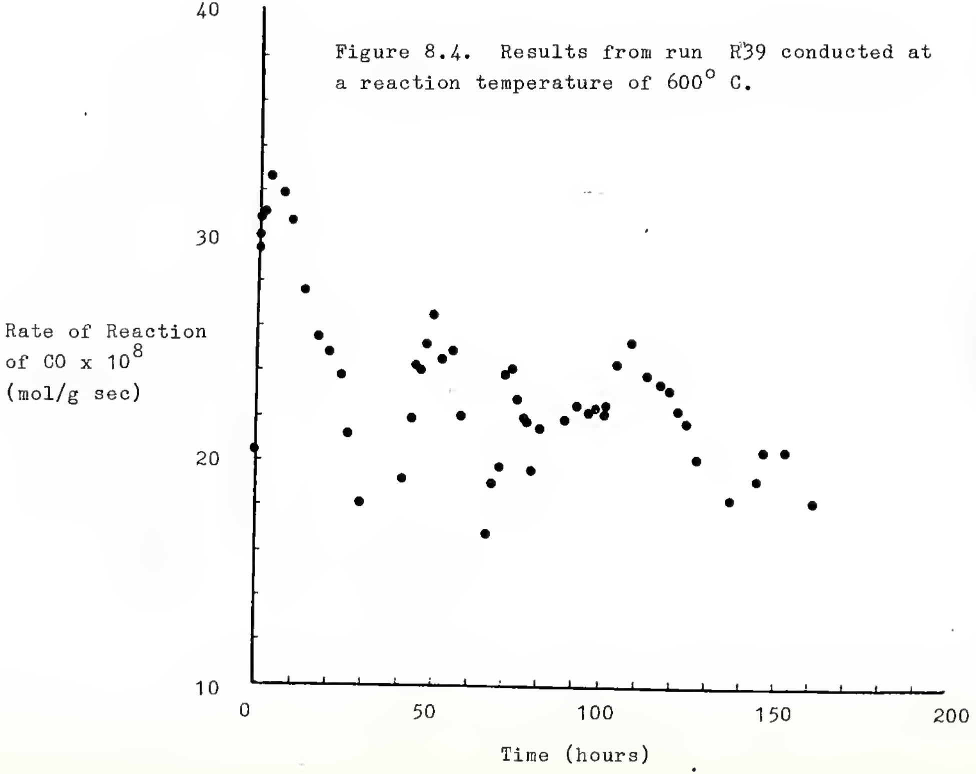

Figure 8.4. Results from run R39 conducted at a reaction temperature of 600° C.

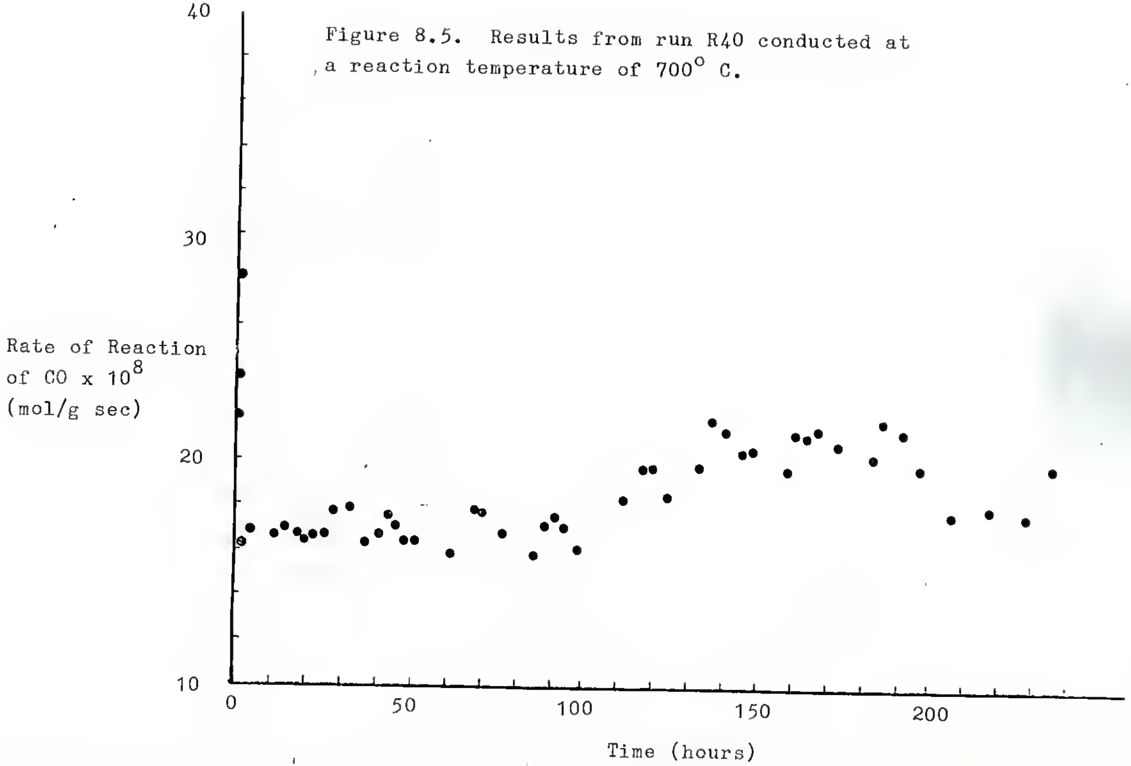

Figure 8.5. Results from run R40 conducted at a reaction temperature of 700° C.

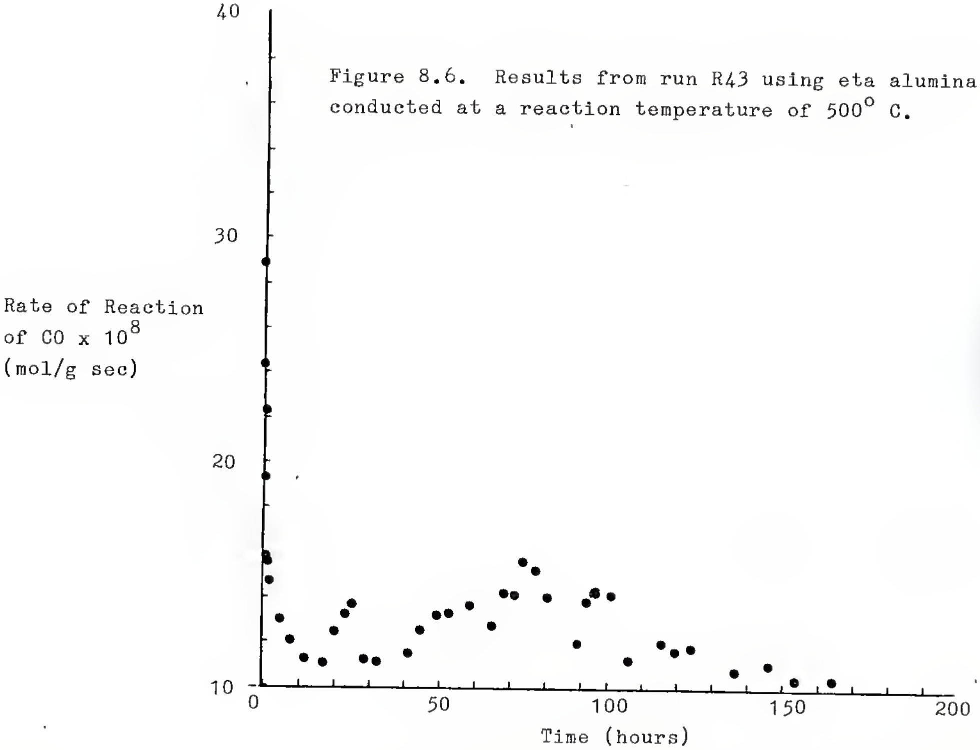

Figure 8.6. Results from run R43 using eta alumina conducted at a reaction temperature of 500° C.

Table 8.2

Experimental conditions. Gamma alumina was used except where indicated.

Run #	Flow Rate (mol/sec) x10^6	Mass of Catalyst (g)	Temp. (^oC)
R-35	6.831	.2376	600
R-36	7.693	.3188	500
R-37	6.009	.3095	550
R-39	6.571	.2400	600
R-40	6.358	.2489	700
*R-43	6.501	.2645	500

The temperature was controlled to ± 10^o C.

* η alumina was used.

production batch, and had to be stored and handled for over 2 months before the problem occured.

It is believed that the data in runs 35, 36, 37, and 39 is good because experiments 36 and 37 were performed between two runs that repeated themselves. The repetition of runs 35 and 39 is very unlikely to be coincidental. The results from run 40 at 700° C were also found to be lower than those obtained at lower temperatures, but this was attributed to the change in the equilibrium driving force of the reaction that had occured. See Figure 8.5 and Table 8.1.

8.4 Investigation of Phase Change

The results, seen in Figures 8.1 to 8.5, show an expected initial decline in the rate but then an unexpected increase was observed. After this increase, the rate again declined and continued to decline for the remainder of the experiment.

The rate increase was postulated to occur from a phase change of the gamma alumina to theta alumina. The temperature in which the experiments were conducted, 450 to 700° C, is near the transition range of gamma to theta alumina. However, the temperature required for the phase change is dependent upon the crystallite size and impurities that are present and is not clearly defined. To investigate the possibility that the crystallographic phase change caused the rate increase, x-ray diffraction patterns were made on alumina subjected to the reaction conditions. Because it was not possible to separate the alumina from the quartz wool, a bed of catalyst not diluted or supported on the wool was used. This enabled a sample of the alumina to be taken and used for the x-ray diffraction studies. The results of the diffraction patterns of the alumina subjected to reaction conditions at 550° C can be seen in Figures 8.7 and 8.8. The x-ray diffraction patterns obtained in this manner were compared to those of the gamma alumina before the experiments, Figure 4.8, and it was concluded that the phase change did not take place and was not responsible for the increase in the rate. A check of the literature revealed no mention of this type of behavior for this reaction and no other explanation could be put forth.

8.5 Reaction Kinetics Analysis

The focus of the work was then directed to studying the initial decline of the rate, specifically, the time before the rate started to increase but after the reactor had stabilized. That is, the first points of the experiments that produced rates far above any of the other points were not considered. These initial samples contained some helium, as was evident by the reduced height of CO and CO_2 peaks compared the samples taken a few minutes later. Because of helium being present, an accurate composition of the exit gas stream could not be found using the gas chromatograph. Graphs showing the portion of the data that will be discussed may be seen in Figures 8.9 to 8.14.

The data was analyzed using the principles described

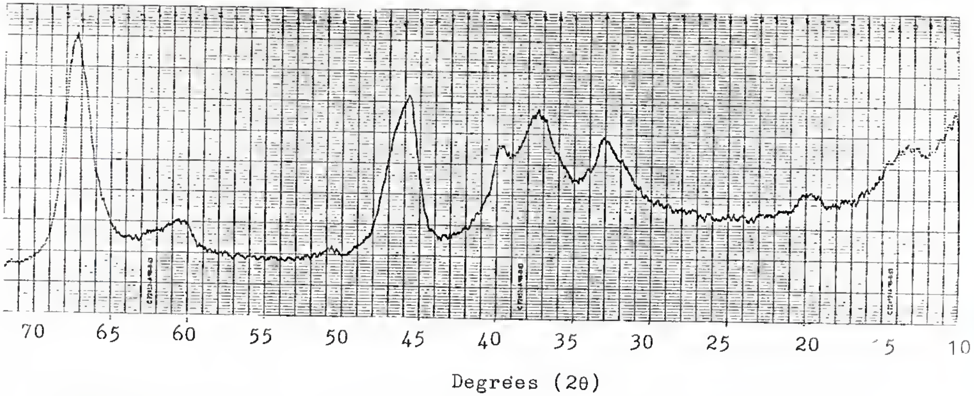

Figure 8.7. The x-ray diffraction pattern of gamma alumina that was placed in flowing carbon monoxide for 15 hours at 600 C.

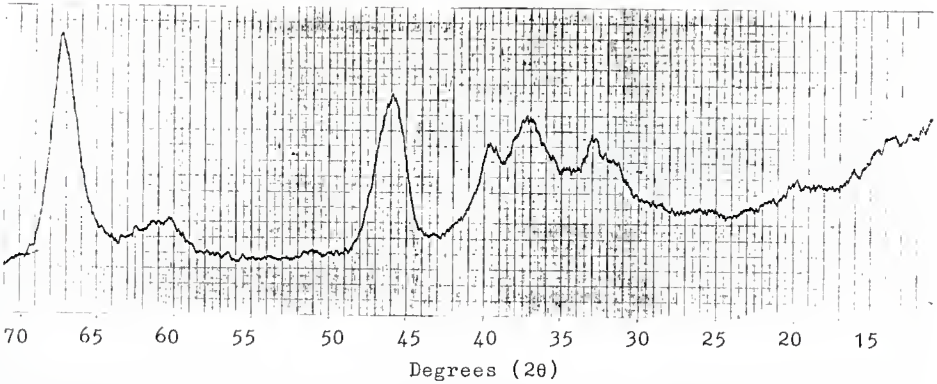

Figure 8.8. The x-ray diffraction pattern of gamma alumina that was placed in flowing carbon monoxide for 159 hours at 600 C.

Figure 8.9. The initial decline of the rate of reaction for run R35.

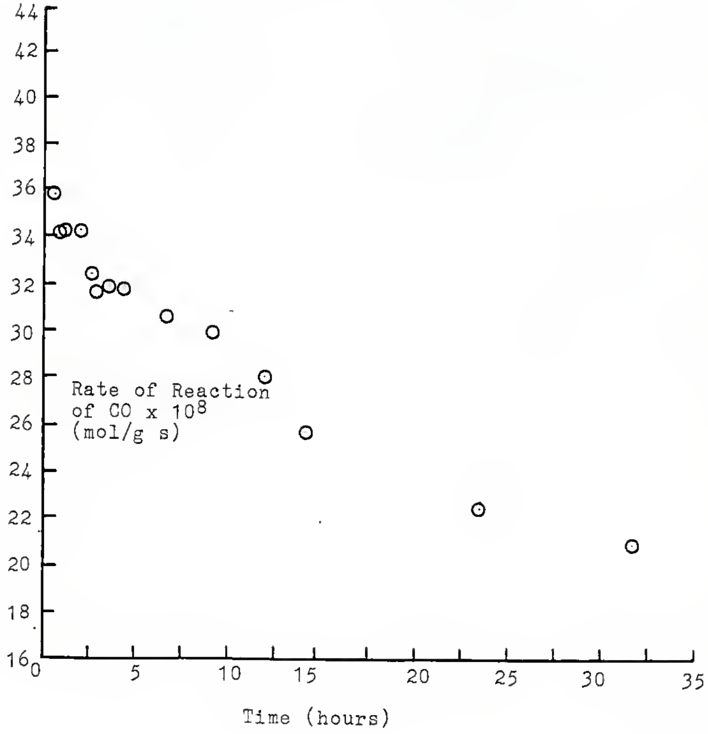

Figure 8.10. The initial decline of the rate of reaction for run R36.

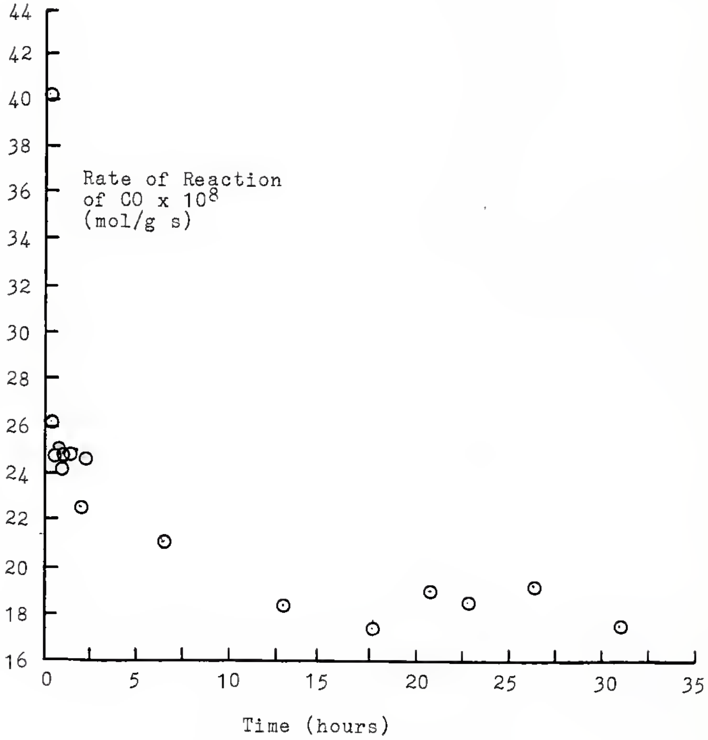

Figure 8.11. The initial decline in the rate of reaction for run R37.

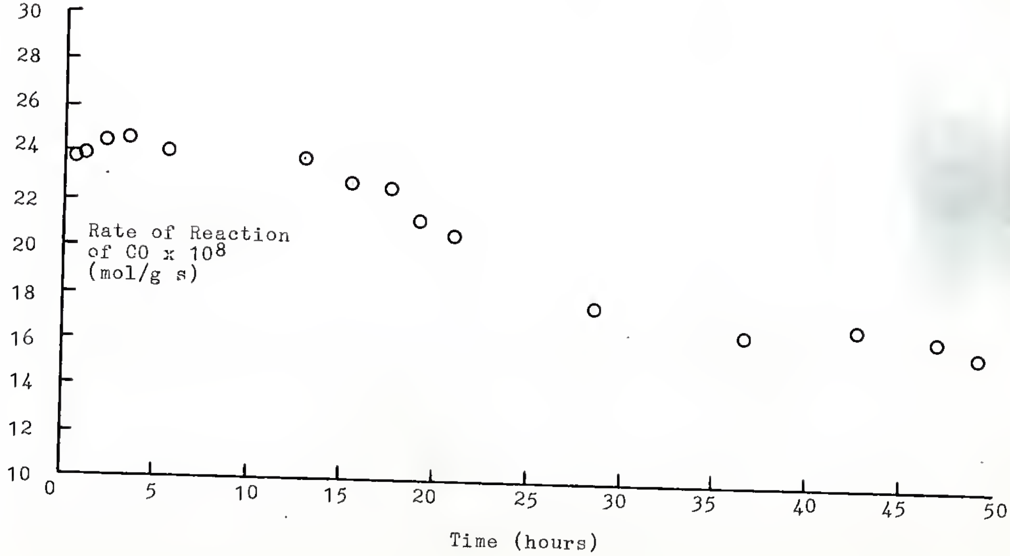

Figure 8.12. The initial decline in the rate of reaction for run R39.

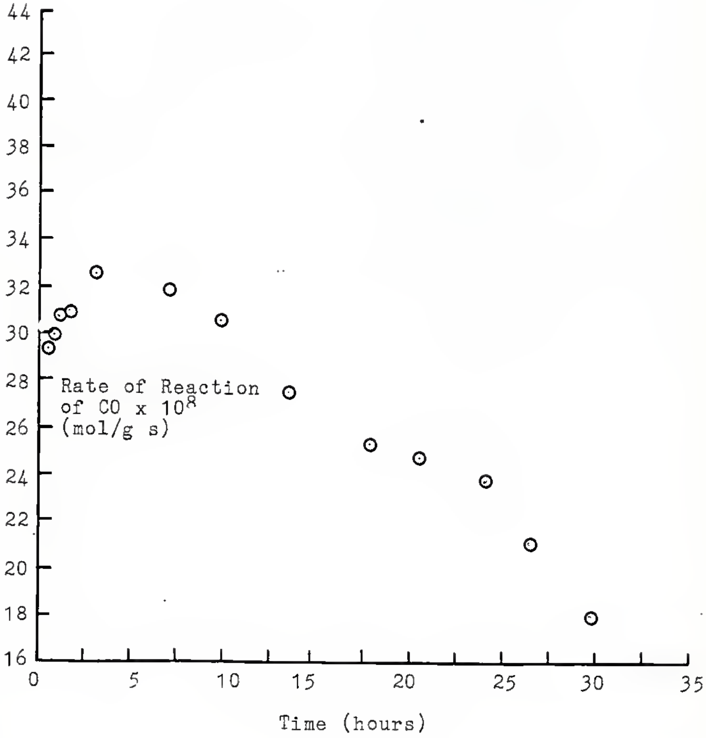

Figure 8.13. The initial decline in the rate of reaction for run R40.

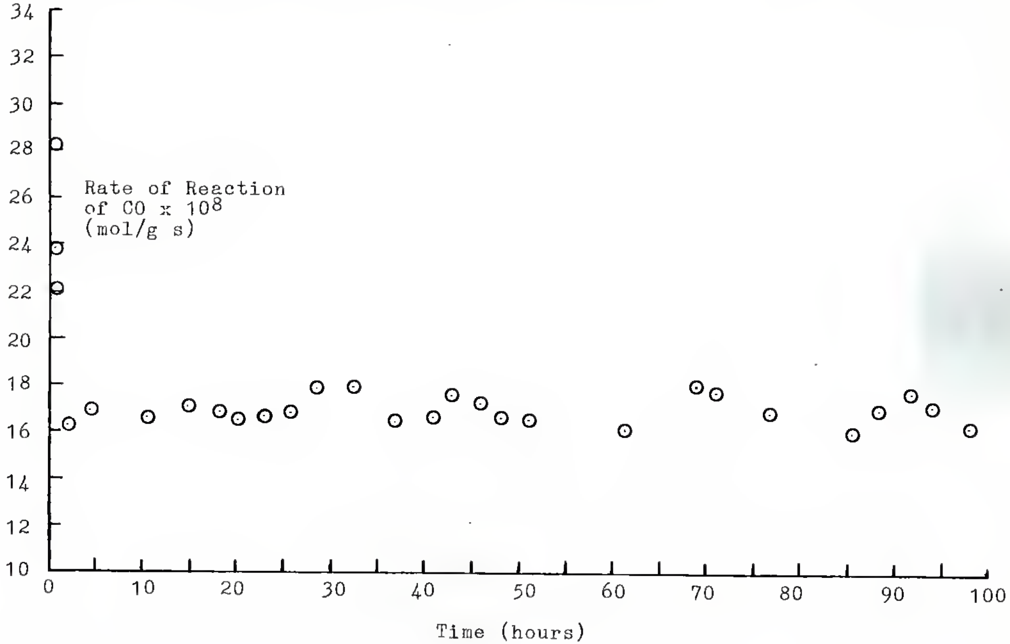

Figure 8.14. The initial decline of the rate of reaction for run R43.

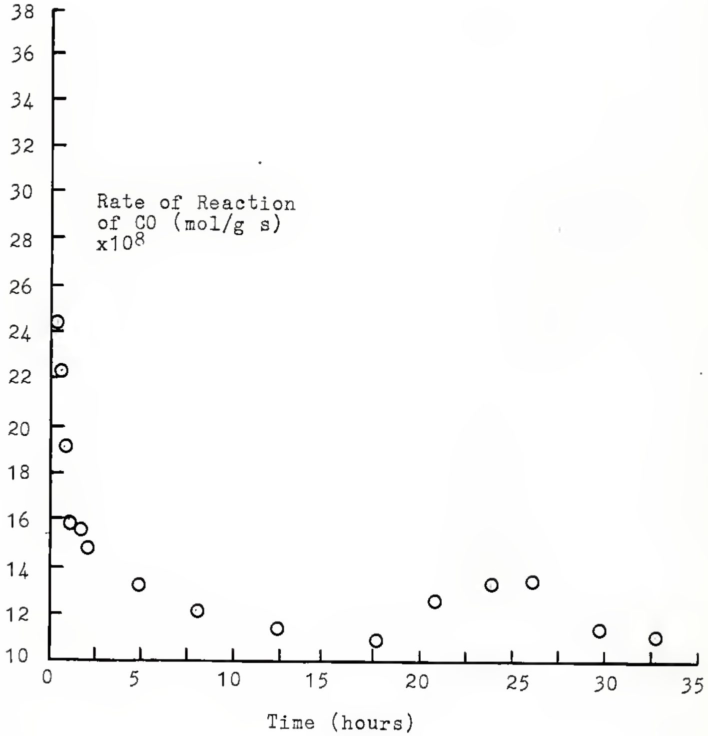

by Froment and Bischoff (4,37) for the kinetics of catalyst deactivation by coking. The disproportionation reaction on alumina was well suited for this analysis since everytime a molecule of CO_2 wa- produced a molecule of carbon (coke) was left on the catalyst.

Historically, empirical correlations such as the Voorheis corrialtion, shown in equation 8.1, have been widely accepted to correlate coking and a reaction rate. This approach does not try to explain or consider the origin of the coke.

$$C_1 = At^n \qquad .05<n<1 \qquad 8.1$$

Since coke is formed from the reaction mixture itself, the rate of coking must depend upon the composition of the reaction mixture, the temperature, and catalyst activity. Therefore, it is not justified to treat coking separately from the main reaction as the Voorheis correlation does. Froment and Bischoff were the first to relate the factors that affect coking, quantitatively to the rate of coking, and draw conclusions form the relation.

The analysis of Froment and Bischoff can best be explained by working whrough an example. Consider the following steps:

Step A $2CO + 2l \rightleftarrows 2COl$ 8.2

Step B $2COl \rightleftarrows CO_2l + C_l$ 8.3

Step C $CO_2l \rightleftarrows CO_2 + l$ 8.4

where

1 = a vacant site on the catalyst
CO1 = an adsorbed CO molecule
$CO_2 1$ = an adsorbed CO_2 molecule
C_1 = an adsorbed carbon molecule

If it is assumed that step B is the rate controlling step, the other steps can be assumed to be in equilibrium and the following equilibrium relationships may be written.

From step A $\{CO1\} = (K_1)^{\frac{1}{2}}\{CO\}\{1\}$ 8.5

From step B $\{CO_2 1\} = K_3\{CO_2\}\{1\}$ 8.6

where the bracketed quantities are concentrations of the species inside.

From step B the rate of reaction may be written as

$$r = k_1\{CO1\}^2 - k_2\{CO_2 1\}\{C_1\} \qquad 8.7$$

where k_1 and k_2 are the rate constants for the forward and reverse reactions of step B respectively. Equation 8.7 can be rewritten using $K_2 = k_2/k_1$ to obtain the following result.

$$r = k_1\left(\{CO1\}^2 - \frac{\{CO_2 1\}\{C_1\}}{K_2}\right) \qquad 8.8$$

Substitutions for the non-measurable quantities of {CO1} and $\{CO_2 1\}$ using the equilibrium relations from steps A and C were made to obtain equation 8.9.

$$r = k_1\left(K_1\{CO\}^2\{1\}^2 - \frac{K_3}{K_2}\{CO_2\}\{1\}\{C_1\}\right) \qquad 8.9$$

It was now assumed that the concentration of the total number of sites taking part in the reaction was a constant T which may be expressed by the following relation.

$$T = \{l\} + \{COl\} + \{CO_2l\} + \{C_l\} \qquad 8.10$$

Substituting for COl and CO_2l using the equilibrium equations 8.5 and 8.6, equation 8.10 may be written as follows:

$$T - \{C_l\} = \{l\}\ (1 - K_1^{\frac{1}{2}}\{CO\} + K_3\{CO_2\}) \qquad 8.11$$

$(T - \{C_l\})$ is the concentration of sites actively participating in the reaction. Using this quantity an expression for the fraction of the initial sites that are actively participating in the reaction (ϕ_c) may be found using equation 8.12 below.

$$\phi_c = \frac{T - \{C_l\}}{T} \qquad 8.12$$

ϕ_c could also by reffered to as the activity of the catalyst. The catalyst would initially have an actively of 1 and would declince as more sites become deactivated as carbon deposited on the catalyst. If equation 8.11 is solved for $\{l\}$ and the result substituted into the rate equation along with ϕ_c the resulting expression for the rate can be seen in equation 8.13.

$$r = \frac{k_1K_1\{CO\}^2T^2\phi_c^2}{(1 + K_1^{\frac{1}{2}}\{CO\} + K_3\{CO_2\})} - \frac{k_1K_3\{CO_2\}(1 - \phi_c)\phi_cT^2}{K_2(1 + K_1^{\frac{1}{2}}\{CO\} + K_3\{CO_2\})} \qquad 8.13$$

In the absence of information on the total number of sites participating in the reaction and the coverage of the active sites by coke, there is no other possibility than to relate ϕ_c emperically to the deactivation. The most direct measure of the sites covered by coke, and also ϕ_c, is the carbon (coke) content of the catalyst. In other words express ϕ_c as a function of the carbon content. $\phi_c = f(\{C_1\})$ On the basis of experimental observation, Froment and Bischoff proposed the following forms for the relationship between ϕ_c and $\{C_1\}$.

$$\phi_c = \exp(-\alpha\{C_1\}) \qquad 8.14$$

$$\phi_c = \frac{1}{1 + \alpha\{C_1\}} \qquad 8.15$$

where α is a constant.

The approach followed in deactivation studies is often different from the one used here. The difference appears in the empirical expression for ϕ_c, the activity. The approach used here is to assume the activity is a function of the carbon content, whereas the alternate approach assumed ϕ_c is a function of time. Using the deactivation function as a function of time presents several drawbacks.

First, from the definition of ϕ_c in equation 8.12 it can be concluded that

$$\frac{-1}{T}\frac{d\{C_1\}}{dt} = \frac{d\phi_c}{dt} \qquad 8.16$$

From step B it can be concluded that the following equation is true.

$$-r = \frac{d\{C_1\}}{dt} \qquad 8.17$$

If the relation for the rate, equation 8.13, is substituted for r in equation 8.17, the following expression is obtained.

$$\frac{d\phi_c}{dt} = \frac{k_1K_1\{CO\}^2T\phi_c^2}{(1 + K_1^{\frac{1}{2}}\{CO\} + K_3\{CO_2\})^2} - \frac{k_1K_3\{CO_2\}\ (1 - \phi_c)\phi_cT^2}{K_2(1 + K_1^{\frac{1}{2}}\{CO\} + K_3\{CO_2\})^2} \qquad 8.18$$

Equation 8.18 clearly shows that ϕ_c cannot be solely a function of time. Also, in assuming $\phi_c = f(t)$, the application of the relation that is found empirically is limited to the conditions prevailing during its determination. With the approach described by Froment and Bischoff (4.37), α is a true constant related to the deactivation event totally since the effects of the operating conditions on the deactivation are explicitly accounted for in the rate equation.

In this work, four different mechanisms were examined in the manner just described. The analysis was carried out several times for each proposed mechanism. Each time a different step was assumed to be rate controlling. The four mechansims that were examined can be seen in Table 8.3 and the resulting rate expressions in Table 8.4. The derivations of these rate equations can be found in the appendix. Certainly an infinite number of reaction

Table 8.3

Proposed mechanisms for the disproportionation of CO on alumina.

Mechanism 1.

Step A	$2CO + 2l \rightleftarrows 2COl$	
Step B	$2COl \rightleftarrows CO_2l + C_l$	(a1)
Step C	$CC_2l \rightleftarrows CO_2 + l$	

Mechanism 2.

Step A	$CC + l \rightleftarrows COl$	(b1)
Step B	$COl + CO + l \rightleftarrows CO_2l + C_l$	(b2)
Step C	$CO_2l \rightleftarrows CO_2 + l$	

Mechanism 3.

Step A	$CC + l \rightleftarrows COl$	(c1)
Step B	$CCl + CO \rightleftarrows C_2O_2{}^*l$	(c2)
Step C	$C_2O_2{}^*l \rightleftarrows CO_2 + C_l$	(c3)

Mechanism 4.

Step A	$CO + l \rightleftarrows COl$	(d1)
Step B	$COl + CO \rightleftarrows CO_2 + C_l$	(d2)

Table 8.4

Derived Rate Equations

(a1) $$r = \frac{k_1K_1\{CO\}^2T^2\phi_c^2}{(1 + K_1^{\frac{1}{2}}\{CO\} + K_3\{CO_2\})^2} - \frac{k_1K_3\{CO_2\}(1 - \phi_c)T^2}{K_2(1 + K_1^{\frac{1}{2}}\{CO\} + K_3\{CO_2\})}$$

(b1) $$r = k_1\{CO\}\left[\frac{\phi_cT\left[1 - \frac{K_3\{CO_2\}}{K_2\{CO\}}\right] + \frac{TK_3\{CO_2\}}{K_2\{CO\}}}{K_3\ CO_2 + 1}\right] - \frac{k_1K_3\{CO_2\}(1 - \phi_c)T}{K_2K_1\{CO\}}$$

(b2) $$r = \frac{k_1K_1\{CO\}^2T^2\phi_c^2}{(1 + K_1\{CO\} + K_3\{CO_2\})^2} - \frac{k_1K_3\{CO_2\}(1 - \phi_c)\phi_cT^2}{K_2(1 + K_1\{CO\} + K_3\{CO_2\})}$$

(c1) $$r = k_1\{CO\}\left[\phi_cT - \frac{K_3\{CO_2\}(1 - \phi_c)T}{K_2\{CO\}} - K_3\{CO_2\}(1 - \phi_c)T\right] - \frac{k_1K_3\{CO_2\}(1 - \phi_c)T}{K_1K_2}$$

(c2) $$r = k_1K_1\{CO\}^2\left[\frac{\phi_cT - K_3\{CO_2\}(1 - \phi_c)T}{1 + K_1\{CO\}}\right] - \frac{k_1K_3\{CO_2\}(1 - \phi_c)T}{K_2}$$

Table 8.4 Cont.

(c3) $$r = k_1K_2K_1\{CO\}^2\ \phi_cT - \frac{k_1\{CO_2\}(1 - \phi_c)T}{K_3}$$

(d1) $$r = k_1\{CO\}\left[\phi_cT\left[1 + \frac{\{CO_2\}}{K_2\{CO\}}\right] + \frac{\{CO_2\}}{K_2\{CO\}}\right] - \frac{k_1\{CO_2\}(1 - \phi_c)T}{K_1K_2\{CO\}}$$

(d2) $$r = \frac{k_1K_1\{CO\}^2T_c}{1 + K_1\{CO\}} - \frac{k_1\{CO_2\}(1 - \phi_c)T}{K_2}$$

mechanisms could be proposed for this reaction. Those investigated here are just a few of those that are possible.

In this work, pure CO was used as the reactant feed and the extent of reaction was kept low (<2%) so the reactor could be analyzed differentially. Therefore, the concentration of CO_2 was very small. Also, the equilibrium constant for all of the temperatures investigated, except 700° C, indicated that nearly complete reaction would have to occur before equilibrium was approached for this system. Because of the low CO_2 concentrations and the equilibrium constant, the terms involving the concentration of CO_2, which were the reverse reaction terms, were assumed to be small compared to the other terms in the expressions. Also, because the extent of conversion was low, the concentration of CO in the reactor could be treated as a constant for the length of the experiment. When this was taken into account, all of the derived rate expressions reduced to two forms. See equations 8.19 and 8.20. The details of this simplification may be found in the appendix.

$$r = X\phi_c \qquad 8.19$$

$$r = X\phi_c^2 \qquad 8.20$$

where X = a constant.

The next step in the analysis of the data was to substitute the suggested forms for the activity given by Froment and Bischoff (4) into the simplified rate expressions. This was done to see if the data obtained could be correlated in a manner consistant with the mechanisms derived using the suggested activity functions.

After the suggested expressions for the activity were substituted into the simplified rate equations, the resulting equations were rearranged so that a plot could be made to determine if the data could be correlated. A summary of the results of the simplification and the rearrangement can be seen in Table 8.5. The final equations were put into a form in which a linear plot would result when the plot indicated in Table 8.5 were made if the data was consistent with the theory.

In order to make the needed plots a value for the carbon content per gram of catalyst had to be determined for every sampling time. This was done by integrating the CO_2 concentration in the exit stream with respect to time, multiplying the result by the molar flow rate and dividing by the mass of the catalyst used.

The integration was carried out by drawing a line between successive data points and finding the area below the line. Performing the integration in this manner precluded the need to smooth the data and was accomplished using a program written by the author for a Commodore 64 computer. The integration started after 6 minutes had elapsed from the start of the reaction. This eliminated the initial data points in which the exact mole fractions of the CO_2 present could not be found because of the helium that was present. The program that was used may be found in the appendix.

Table 8.5

Simplified Rate Expressions

Simplified Rate Expression	$r = X\phi_c$	
Suggested Form for ϕ_c	$\phi_c = \exp(-\alpha\{C_1\})$	$\phi_c = \frac{1}{1 + \alpha\{C_1\}}$
Resulting Rate Expression	$r = X\exp(-\alpha\{C_1\})$	$r = \frac{X}{1 + \alpha\{C_1\}}$
Rearranged of Rate Expression	$\ln(r) = \ln(X) - \alpha\{C_1\}$	$r = -r\alpha\{C_1\} + X$
Plot Used to Test Data	$\ln(r)$ vs $\{C_1\}$	r vs $r\{C_1\}$
Slope	$-\alpha$	$-\alpha$
Intercept	$\ln(X)$	X

Table 8.5 Cont.

Simplified Rate Expression	$r = X\phi_c^2$	
Suggested Form for ϕ_c	$\phi_c = \exp(-\alpha\{C_1\})$	$\phi_c = \frac{1}{1 + \alpha\{C_1\}}$
Resulting Rate Expression	$r = X\exp(-2\alpha\{C_1\})$	$r = \frac{X}{(1 + \alpha\{C_1\})^2}$
Rearrangement of Rate Expression	$\ln(r) = \ln(X) - 2 \quad C_1$	$\sqrt{r} = -\sqrt{r}\alpha\{C_1\} + \sqrt{X}$
Plot Used to Test Data	$\ln(r)$ vs $\{C_1\}$	$\sqrt{r}$ vs $\sqrt{r}\{C_1\}$
Slope	-2α	$-\alpha$
Intercept	$\ln(X)$	$-\sqrt{X}$

The graphs indicated in Table 8.5 were made and may be seen in Figures 8.15 to 8.17. The 700° C experiment was not used in this analysis because at this temperature, the equilibrium requirements were such that the reverse reaction could be taking place at an appreciable rate which made this analysis invalid. All of the graphs were found to be linear which indicated that the data obtained could be correlated using the techniques outlined here. In fact, upon further investigation it was found that the data from runs at different temperatures could be fit rather well with a line having the same slope but a different intercept. See Figures 8.15 to 8.17. This indicated that the deactivation could be correlated and the deactivation constant was the same for all of the temperatures studied. Because the plots were nearly linear for all the runs and the different functions for the activity, none of the mechanisms and functions for the activity could be proven to be incorrect.

A summary of the linear relations that were found for each of the individual experiments and the average for each of the activity relationships studied may be found in Tables 8.6 to 8.8. The linear relations for the individual lines were found using least squares, but not all of the data at the beginning of the run was used, to prevent overemphasis of the beginning of the run in determining the slope.

In the developement of the analysis it was stated that

Figure 8.15. A plot of ln(rate of reaction) verses the carbon content of the catalyst.

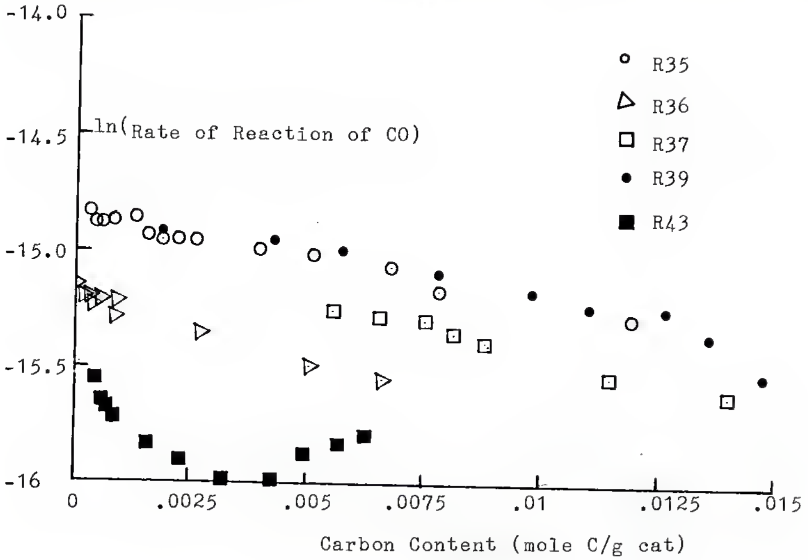

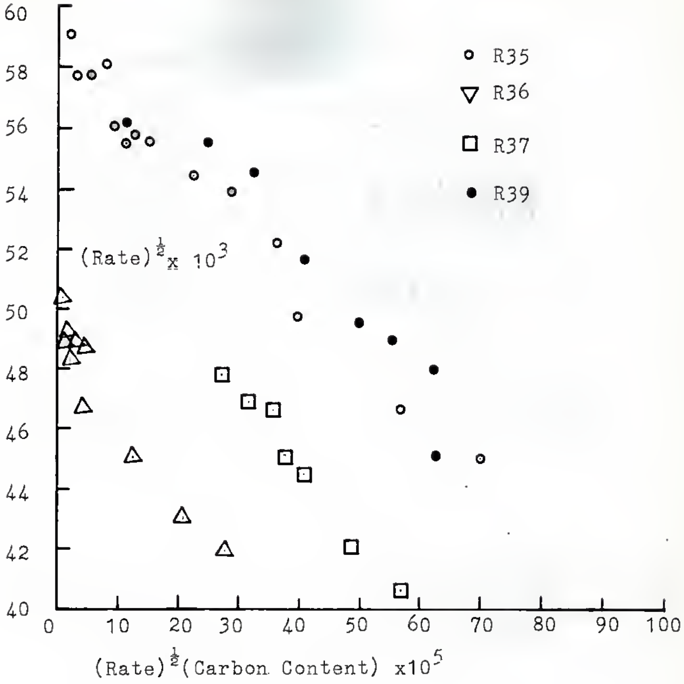

Figure 8.16. A plot used to determine the relationship between the carbon content of the alumina and the activity of the catalyst for the disproportionation reaction.

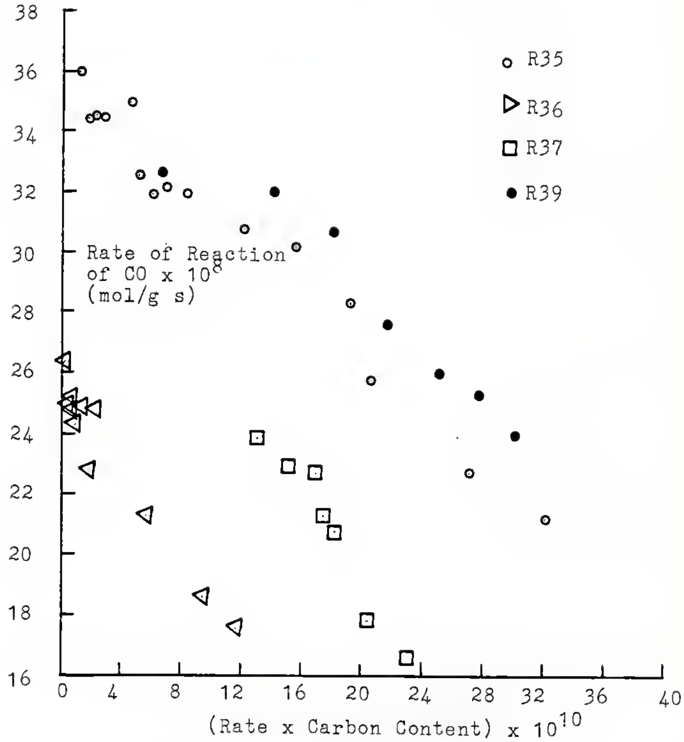

Figure 8.17. A plot used to determine the relationship between the carbon content of the alumina and the activity of the catalyst for the disproportionation reaction.

Table 8.6

Information obtained from the Rate vs. Carbon Content plot

Exp. #	Slope	Intercept	α
R35	-52.13	3.721×10^{-7}	52.13
R36	-70.68	2.549×10^{-7}	70.68
R37	-81.16	3.527×10^{-7}	81.16
R39	-52.36	3.937×10^{-7}	52.36
*Average	-68.03	--------	68.03
**R43	-145.0	1.650×10^{-7}	145.0

* The average slope was calculated by first averaging the slopes of R35 and R39 and using this result to average with R36 and R37.

**Eta alumina was used in this experiment.

Table 8.7

Information obtained from the ln(Rate) vs Carbon Content plot.

Exp. #	Slope	Intercept	α
R35	-39.24	-14.84	39.24
R36	-46.24	-15.25	46.24
R37	-46.53	-14.98	46.53
R39	-42.08	-14.78	42.08
*Average	-44.48	------	44.48
**R43	-111.0	-15.65	111.0

* The average slope was calculated by first averaging the slopes of R35 and R39 and using this result to average with R36 and R37.

** Eta alumina was used in this experiment.

Table 8.8

Information obtained from $(\text{Rate})^{\frac{1}{2}}$ vs. $(\text{Rate})^{\frac{1}{2}}$(Carbon Content) Plot.

Exp. #	Slope	Intercept	α
R35	-21.84	6.057×10^{-4}	21.84
R36	-34.24	5.095×10^{-4}	34.24
R37	-29.84	5.738×10^{-4}	29.84
R39	-20.46	6.081×10^{-4}	20.46
*Average	-28.41	----------	28.41
**R43	-63.01	4.032×10^{-4}	63.01

*The average slope was calculated by first averaging the slopes of R35 and R39 and using this result to average with R36 and R37.

**Eta alumina was used in this experiment.

the constant α is related totally to the d activation event and the effects of the operating conditions were explicitly accounted for in the rate equation. This fact enables the relations between the activity of the gamma alumina and the carbon content that were found in this work, to be used in future work where the composition of the entrance stream was a mixture of CO and CO_2. The data obtained from this future work, along with the results obtained here could then be used to determine which, if any of the proposed mechanisms describe what is actually occuring. Therefore, this work should be considered the first step in an ongoing attempt to determine a possible mechanism for the disproportionation of CO on alumina.

8.6 Removal of Carbon

It should be mentioned that the carbon that was deposited on the alumina seemed quite easy to remove by heating the alumina in air. After an experimental run was completed, the CO flow was stopped and the reactor left open to the atmosphere, while the catalyst was maintained at the reaction temperature. The alumina that had turned gray during the experiment appeared white again within 30 minutes. The removal of the carbon under these conditions was thought to occur by a burning reaction between the carbon and the oxygen in the air. Also, it was found that the carbon could be removed by passing pure CO_2 over the catalyst containing the carbon at the reaction temperatures. The removal of the carbon in this manner was thought to proceed by the reverse disproportionation reaction i.e.,

$$C + CO_2 \rightleftarrows 2CO$$

8.7 Effect of Carbon on Surface Area

In order to determine if the carbon deposited by the reaction was deposited evenly on the surface or in a manner in which pores of the alumina were closed, surface area studies of the alumina containing carbon were conducted. The surface area of the alumina before the reaction, after the reaction, and after the reaction and the carbon deposited was burned off, were made and the results found in Table 8.9. The surface area was measured utilizing physical adsorption of nitrogen at liquid nitrogen temperatures using a Perkin-Elmer Sorptometer as mentioned earlier in the procedure.

The surface areas from the different samples all yielded approximately the same surface area, nearly 95 m^2/g. This indicated that the carbon did not clog the pores of the alumina. If that had happened, a dramatic decrease in the surface area should have resulted. This was very engouraging because the alumina deposited with carbon retained its high surface area. The resulting mixture was one of two widely used adsorbents. It is possible that the mixture of these two adsorbents, carbon and alumina, would produce a substance with a combination of the sorptive properties of the individual components that culd be used in applications in the future.

Table 8.9

Results of Surface Area Studies on Alumina

Sample	m^2/g
γ Alumina	94.8
γ Alumina with Carbon present	87.8
γ Alumina after Carbon deposit was removed	113.2

It is also possible that the carbon containing alumina could have some unique and useful catalytic properties. This too should be investigated.

CHAPTER 9

FUTURE WORK

In this work, correlations between the carbon content of gamma alumina and the rate of CO disproportionation at different temperatures were determined using the approach put forth by Froment and Bischoff. Additional data is required in which a range of compositions of CO and CO_2 are fed to the reactor and a parametric study of the results with the derived rate expressions performed. This would determine which, if any, of the proposed mechanisms fully explain the observed reaction. Determination of the mechanism that best correlates to the data could lead to some new insights on the causes of coking and how to prevent it. This type of analysis could also be extended to different phases of alumina such as eta, delta, and theta.

The sorptive and catalytic properties of the carbon containing alumina that is produced by the disproportionation reaction should be investigated. It is possible that the carbon deposited on the alumina would have properties similar to activated carbon, and therefore the carbon containing alumina may possess a combination of the properties normally associated with alumina and activated carbon individually. This may result in a substance that could have applications in which alumina or activated carbon individually, would not normally be used.

ACKNOWLEDGMENTS

The author wishes to express sincere gratitude to Dr. John C. Matthews for his advice and encouragement during this work. The author also extends his gratitude to the Department of Chemical Engineering and the Dow Chemical Company for financial support. Thanks are also due to Dr. John R. Schlup and Dr. Benjamin Kyle, for serving as the advisory committee. Thanks are extended to Mr. Duane Morey for his help with equipment maintenance and Jeff Smith for the surface area determinations.

Most of all, the author wishes to give special thanks to his wife Yvonne, whose constant help and support helped him through the rough times.

REFERENCES

1. Belding, W. A. and Warfield, W. C., "Controlling the Properties of Catalyst Substrates Using Alumina", Kaiser Aluminum and Chemical Corporation, Pleasanton, p 1, 1982.

2. Knozinger, H., et al., "Catalytic Alumina: Surface Models and Characterization of Surface Sites", Catal. Rev. - Sci. & Eng., 17:1 (1978).

3. Gates, B. C., et al., "Chemistry of Catalytic Processes", McGraw-Hill, New York, 1979.

4. Froment, G. F. and Bischoff, K. B., "Chemical Reactor Analysis and Design", John Wiley & Sons, New York, pp 271-301, 1979.

5. Lippens, B. C. and Steggerda, J. J. in "Physical and Chemical Aspects of Adsorbents and Catalysts", edited by Lisen, B. G., Academic Press, New York, 1970.

6. Wefers, K. and Bell, G. M., "Oxides and Hydroxides of Aluminum", Alcoa Research Laboratories, Technical Paper No. 19, 1972.

7. American Ceramic Society, "Alumina as a Ceramic Material", edited by Gitzen, W. H., American Ceramic Society, Columbus, Ohio, 1970.

8. Bragg, W. L., et al., in "Crystal Structures of Minerals", Cornell University Press, Ithaca, New York, 1970.

9. Lippens, B. C., "Structure and Texture of Aluminas", Doctorate Dissertation, Technical School, Delft, April 26, 1961.

10. Leonard, A. J., et al., "Structures and Properties of Amorphous Silico-Aluminas", Proc. British Ceramic Society, No.13, pp 103-116 (1969).

11. Geller, S., "Crystal Structure of β-Ga_2O_3", J. Chem. Phys., 33:3 (1960).

12. Kohn, J. A., et al., "Characterization of β-Ga_2O_3 and Its Alumina Isomorph θ-Al_2O_3", Amer. Mineral., Vol. 42, pp 398-408 (1957).

13. Lippens, B. C. and deBour, J. H., "Study of Phase Transformation During Calcination of Aluminum Hydroxides by Selected Area Electron Diffraction", Acta Cryst., 17:10, pp1312-21 (1964).

14. Roy, R., et al., "Polymorphs of Alumina and Gallia", Ind Eng. Chem., 45:4, pp 819-20 (1953).

15. Saalfeld, H., "Structure Phases of Dehydrated Gibbsite", Proc. Intern. Symp. Reactivity Solid, 4th, Amsterdam, pp 310-320 (1960).

16. Brindley, G. W., "The Reaction Series Gibbsite-Chi-Kappa-Corundum II", Amer. Mineral., Vol. 46, pp 1187-90 (1961).

17. Peri, J. B., "A Model for the Surface of Gamma Alumina", J. Phys. Chem., 69:1, pp 220-30 (1965).

18. Van Vlack, L. H., "Elements of Material Science and Engineering", 4th Ed., Addison & Wesley, Reading, Massachusetts, 1980.

19. Van Norstrand, R. E., "X-ray Studies of Activated Aluminas. I. Eta and Gamma Aluminas", American Chemical Society, Dallas Meeting, April 8-13, p43, 1956.

20. Kim-Oanh, T. N., Masters Thesis, Kansas State University, 1981.

21. Sato, T., et al., Thermal Analysis, Int. 6th Conf., Bayreuth, 1980.

22. Bennett, J. E. and Pinnel, M. R., "Voluminous Oxidation of Aluminum by Continuous Dissolution in a Wetting Mercury Film", J. Materials Sci., Vol. 7, pp 1016-1026 (1972).

23. Bennett, J. E. and Pinnel, M. R., "Reactions Between Mercury-Wetted Aluminum and Liquid Water", J. Materials Sci., Vol 8, pp 1189-1193 (1973).

24. Lahodny-Sarc, O., et al., "The Influence of the Activity of Water on the Phase Composition of Aluminum Hydroxides Formed by the Reaction of Amalgamated Aluminum with Water", Clays & Clay Min., 26:2, pp 153-159 (1978).

25. Little, L. H. and Amberg, C. H., "Infrared Spectra of Carbon Monoxide and Carbon Dioxide Adsorbed on Chromia-Alumina and on Alumina", Canadian J. Chemistry, Vol. 42, pp 1997-2006 (1962).

26. Parkyns, N. D., "The Surface Properties of Metal Oxides. Part I. Infrared Studies of the Adsorption and Oxidation of Carbon Dioxide on Alumina", J. Chem. Soc. London (A), pp 1910-1913 (1967).

27. Parkyns, N. D., "The Surface Properties of Metal Oxides. Part II. An Infrared Study of the Adsorption of Carbon Dioxide on Gamma Alumina", J. Chem. Soc. London (A), pp 410-417 (1969).

28. Morterra, C., et al., "I. R. Spectroscopic Study of CO_2 Adsorption onto η-Al_2O_3", J. Chem. Soc. London, Faraday Trans. 1, Vol. 73, pp 1544-1560 (1977).

29. Parkyns, N. D., "The Influence of Thermal Pretreatment on the Infrared Spectrum of Carbon Dioxide Adsorbed on Alumina", J. Phys. Chem., 75:4, pp 526-531 (1971).

30. Yakerson, V. I. et al., "Adsorption of Carbon Monoxide on the surface of Gamma Alumina Oxide", Izv. Akad. Nauk SSSR Ser. Khin., Vol. 19, (1969).

31. Fink, P., "I. R. Spectroscopic and Gravimetric Investigations About the Formation of Carboxylate Surface Species During the Chemisorption of CO, CO_2 and Simple Organic Oxygen Compounds on Gamma Alumina", Revue Roumaine de Chimie, Vol. 14, pp 811-822 (1969).

32. Stanislaus, M. et al., "The Kinetics of Adsorption of Carbon Monoxide on Alumina", J. Phys. Chem., 76:17, pp 2249-2252 (1972).

33. Gatta, G. D. et al., "The Chemisorption of Carbon Monoxide on Various Transition Aluminas", J. of Catal., Vol. 43, pp 90-98 (1976).

34. Handa, P., Masters Thesis, Kansas State University, 1978

35. Instuctions - The Perkin-Elmer Shell Model 212D Sorptometer.

36. Pursley, S. A. et al., " The Kinetics of Carbon Dioxide and Carbon Formation from Carbon Monoxide", J. Phys. Chem., 70:12, pp 3768-3770 (1966).

37. Froment, G. F. and Dumez, F. J., "Dyhydrogenation of 1-Butene into Butadiene. Kinetics, Catalyst Coking, and Reactor Design", Ind. Eng. Chem. Process Des., 15:2, pp 291-301 (1976).

38. Cullity, D., "Elements of X-ray Diffraction", 2nd Edition, Addison-Wesley, Philippines, 1978.

39. Klug, H. P. and Alexander, L., "X-ray Diffraction Procedures', 2nd Edition, Wiley, New York, 1974.

40. United Catalysts Inc., "Physical and Thermodynamic Properties of Elements and Compounds", United Catalysts Inc.

41. Instructions - The Siemens Crystalflex 4 Diffractometer.

APPENDIX 1

DERIVATION OF RATE EQUATION

The notation used in this appendix will be the same as that used in chapter 7.

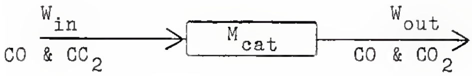

It was assumed that only CO and CO_2 were present in the entrance and exit streams. The first step was to perform an oxygen balance on the reactor assuming it operated in a pseudo steady state condition.

$$xW_{in} + 2(1 - x)W_{in} - yW_{out} - 2(1 - y)W_{out} = 0 \qquad \text{A1.1}$$

Equation A1.1 can be simplified to obtain the following equation.

$$W_{in}(2 - x) - W_{out}(2 - y) = 0 \qquad \text{A1.2}$$

Equation A1.2 can be rearranged to obtain the following expression relating the molar flow rate entering and leaving the reactor.

$$W_{out} = \frac{W_{in}(2 - x)}{(2 - y)} \qquad \text{A1.3}$$

Next, a CO balance was performed on the reactor, again assuming a pseudo steady state condition.

$$xW_{in} - yW_{out} - rM_{cat} = 0 \qquad \text{A1.4}$$

Equation A1.3 was used to substitute for W_{out} in equation A1.4 to obtain equation A1.5.

$$xW_{in} - \frac{yW_{in}(2 - x)}{(2 - y)} - rM_{cat} = 0 \qquad \text{A1.5}$$

Equation A1.5 was solved for r to obtain the following result.

$$r = \frac{W_{in}}{M_{cat}} \left\{ x - \frac{y(2 - x)}{(2 - y)} \right\} \qquad \text{A1.6}$$

Equation A1.6 was used to calculate the rate of reaction of CO per unit mass of catalyst as a function of the entrance and exit compositions and molar flow rate into the reactor.

APPENDIX 2

DERIVATION OF RATE EQUATIONS FROM PROPOSED MECHANISMS

The following is a step by step derivation of rate expressions of the disproportionation reaction of CO on alumina based on assumed mechanisms and the procedure put forth by Froment and Bischoff (4,37). The first possible mechanism that will be analyzed is composed of the following steps.

Mechanism 1

Step 1 $2CO + 2l \rightleftarrows 2COl$ A2.1

Step 2 $2COl \rightleftarrows CO_2l + C_l$ A2.2

Step 3 $CO_2l \rightleftarrows CO_2 + l$ A2.3

where

COl = an adsorbed CO molecule on the alumina

CO_2l = an adsorbed CO_2 molecule on the alumina

C_l = an adsorbed carbon molecule on the alumina

l = a vacant site on the alumina

The analysis using this proposed mechanism will be performed assuming step 2 is the rate determining step. In all of the derivations in this appendix, k_1 will represent the rate constant in the forward direction of the rate determining step, and k_2 will represent the reverse reaction rate constant of the rate determining step.

Because step 2 is considered to be the rate determining step, steps 1 and 3 can be considered to be in equilibrium and the following equilibrium relations may be written.

From step 1 $\{COl\} = K_1^{\frac{1}{2}}\{CO\}\{l\}$ A2.4

From step 3 $\{CO_2l\} = K_3\{CO_2\}\{l\}$ A2.5

where the bracketed quantities are the concentration of the enclosed quantity. K_1 and K_3 are the equilibrium constants for steps 1 and 3 respectively.

Note: It is standard practice to write the equilibrium relation for the desorption reactions as if adsorption were taking place.

Next, the rate of reaction assuming step 2 is rate determining may be written as follows:

$$r = k_1\{COl\}^2 - k_2\{CO_2l\}\{C_l\} \qquad \text{A2.6}$$

Equation A2.6 may be rewritten to obtain equation A2.7.

$$r = k_1\left(\{COl\}^2 - \frac{\{CO_2l\}\{C_l\}}{K_2}\right) \qquad \text{A2.7}$$

where $K_2 = k_2/k_1$

$\{COl\}$ and $\{CO_2l\}$ in equation A2.7 can be replaced using the equilibrium relations in equations A2.4 and A2.5 to obtain the following equation.

$$r = k_1\left(K_1\{CO\}^2\{l\}^2 - \frac{K_3}{K_2}\{CO_2\}\{l\}\{C_l\}\right) \qquad \text{A2.8}$$

The total concentration of sites that participated in the reaction (T), may be written as the sum of all of the adsorbed species plus the vacant sites.

$$T = \{l\} + \{COl\} + \{CO_2l\} + \{C_l\} \qquad \text{A2.9}$$

Again the equilibrium relationships are used to substitute for {COl} and {CO$_2$l} in equation A2.9 which yields the following relation.

$$T = \{l\} + K_1^{\frac{1}{2}}\{CO\}\{l\} + K_3\{CO_2l\}\{l\} + \{C_1\} \qquad \text{A2.10}$$

Equation A2.10 may by rewritten to obtain equation A2.11.

$$T - \{C_1\} = \{l\}(1 + K_1^{\frac{1}{2}}\{CO\} + K_3\{CO_2\}) \qquad \text{A2.11}$$

T - {C$_1$} is the concentration of sites that are still active. When equation A2.11 is solved for {l} and the result substituted into equation A2.8, the following equation for the rate of reaction is obtained.

$$r = k_1\left(\frac{K_1\{CO\}^2(T - \{C_1\})^2}{(1 + K_1^{\frac{1}{2}}\{CO\} + K_2\{CO_2\})^2} - \frac{K_3\{CO_2\}\{C_1\}(T - \{C_1\})}{K_2(1 + K_1^{\frac{1}{2}}\{CO\} + K_3\{CO_2\})}\right)$$

A2.12

Next, the fraction of sites that are actively participating in the disproportionation reaction as the reaction proceeds is given by ϕ_c in equation A2.13.

$$\phi_c = \frac{T - \{C_1\}}{T} \qquad \text{A2.13}$$

When ϕ_c is substituted into the rate equation A2.12, the final form of the complete rate expression is obtained.

$$r = \frac{k_1K_1\{CO\}^2T^2\phi_c}{(1 + K_1^{\frac{1}{2}}\{CO\} + K_3\{CO_2\})^2} - \frac{k_1K_3\{CO_2\}(1 - \phi_c)T^2\phi_c}{K_2(1 + K_1^{\frac{1}{2}}\{CO\} + K_3\{CO_2\})}$$

A2.14

In this work, $\{CO_2\}$ was very small, nearly zero, because **pure CO** was fed to the reactor and the extent of conversion was small (<1%) in most cases. Because of this, the rate equation A2.14 may be simplified by neglecting the terms containing $\{CO_2\}$. The simplified rate expression is seen in equation A2.15.

$$r = \frac{k_1 K_1 \{CO\}^2 T^2 \phi_c}{(1 + K_1^{\frac{1}{2}}\{CO\})^2} \qquad A2.15$$

This may be further simplified because the concentration of CO was nearly a constant throughout the experiment. The final simplified rate expression has the form of a constant X, multiplied by the activity as shown in equation A2.16.

$$r = X\phi_c \qquad A2.16$$

where

$$X = \frac{k_1 K_1 T^2 \{CO\}^2}{(1 + K_1^{\frac{1}{2}}\{CO\})^2} \simeq \text{constant}$$

The same type of analysis was applied to the following proposed mechanism.

Mechanism 2

Step 1 $CO + l \rightleftarrows COl$ A2.17

Step 2 $COl + CO + l \rightleftarrows CO_2l + C_l$ A2.18

Step 3 $CO_2l \rightleftarrows CO_2 + l$ A2.19

Step 1 will be assumed to be the rate determining step. The same convention will be used as before, with k_1 and k_2 being the rate constant for the rate determining step in the forward and reverse reactions as it appears in the proposed mechanism. Just as before, steps 2 and 3 may be considered in equilibrium if step 1 is the rate determining step. The equilibrium expressions from steps 2 and 3 are as follows:

From step 2 $$K_2 = \frac{\{CO_2l\}\{C_l\}}{\{COl\}\{CO\}\{l\}} \qquad A2.20$$

From step 3 $$\{CO_2l\} = K_3\{CO_2\}\{l\} \qquad A2.21$$

When equation A2.21 is substituted into equation A2.20 the resulting equilibrium expression is equation A2.22.

$$K_2 = \frac{K_3\{CO_2\}\{C_l\}}{\{COl\}\{CO\}} \qquad A2.22$$

The rate of reaction based on mechanism 2 with step 1 controlling may be written as follows:

$$r = k_1\left(\{CO\}\{l\} - \frac{\{COl\}}{K_1}\right) \qquad A2.23$$

where $K_1 = k_2/k_1$.

Substituting for COl in equation A2.23 using equation A2.21, the following result is obtained.

$$r = k_1\left(\{CO\}\{l\} - \frac{K_3\{CO_2\}\{C_l\}}{K_2K_1\{CO\}}\right) \qquad A2.24$$

Next, the total concentration of sites is written as the sum of the adsorbed species and the vacant sites as was performed earlier in equation A2.9. The nonmeasurable quantities in the sum, {COl} and $\{CO_2l\}$ are substituted for using the equilibrium relations A2.21 and A2.22. The resulting expression is solved for {l}, and ϕ_c as defined in equation A2.13 is substituted into the expression to obtain the following equation.

$$\{l\} = \frac{\phi_c T\left(1 - \frac{K_3\{CO_2\}}{K_2\{CO\}}\right) + \frac{TK_3\{CO_2\}}{K_2\{CO\}}}{K_3\{CO_2\} + 1} \qquad A2.25$$

A2.25 is then substituted into equation A2.24 to obtain the final full rate expression.

$$r = k_1\{CO\}\left(\frac{\phi_c T\left(1 - \frac{K_3\{CO_2\}}{K_2\{CO\}}\right) + \frac{TK_3\{CO_2\}}{K_2\{CO\}}}{K_3\{CO_2\} + 1}\right) - \frac{k_1K_3\{CO_2\}(1 - \phi_c)T}{K_2K_1\{CO\}} \qquad A2.26$$

When $\{CO_2\}$ is considered to be nearly zero for the same reasons given before the resulting simplified rate expression is obtained.

$$r = k_1\{CO\}\phi_c T \qquad A2.27$$

If {CO} is taken to be constant as before, equation A2.27 takes the form $r = X\phi_c$.

Mechanism 2 was used again to derive another rate expression but this time step 2 was considered to be the rate determining step. The appropriate equilibrium relations in this derivation can be seen in equations A2.28 and A2.29.

$$\{CO1\} = K_1\{CO\}\{1\} \qquad A2.28$$

$$\{CO_2 1\} = K_3\{CO_2\}\{1\} \qquad A2.29$$

Using the same convention as before, $K_2 = k_2/k_1$. The rate expression may then be written.

$$r = k_1\left[\{CO1\}\{CO\}\{1\} - \frac{\{CO_2 1\}\{C_1\}}{K_2}\right] \qquad A2.30$$

When the equilibrium expressions A2.28 and A2.29 are substituted into A2.30 the resulting rate may be seen in equation A2.31.

$$r = k_1\left[K_1\{CO\}^2\{1\}^2 - \frac{K_3}{K_2}\{CO_2\}\{C1\}\{1\}\right] \qquad A2.31$$

Again finding the concentration of the total number of sites participating in the reaction as the sum of the adsorbed species and the vacant sites, and substituting for {CO1} and $\{CO_2 1\}$ using A2.28 and A2.29. The resulting expression is solved for {1}, ϕ_c is substituted in, and the result substituted into A2.31 to obtain A2.32.

$$r = \frac{k_1K_1\{CO\}^2T^2\phi_c^2}{(1 + K_1\{CO\} + K_3\{CO_2\})^2} - \frac{k_1K_3\{CO_2\}(1 - \phi_c)\phi_cT^2}{K_2(1 + K_1\{CO\} + K_3\{CO_2\})} \qquad A2.32$$

If $\{CO_2\}$ is considered nearly zero, as before, the simplified rate expression may be written.

$$r = \frac{k_1K_1\{CO\}^2T^2\phi_c^2}{(1 + K_1\{CO\})^2} \qquad A2.33$$

If CO is taken to be a constant, then the rate equation can be written by the following form.

$$r = X\phi_c^2 \qquad \text{A2.34}$$

where $X = \dfrac{k_1K_1\{CO\}^2T^2}{(1 + K_1\{CO\})^2} \simeq$ constant

Because the same logical sequence is used to derive all the rate equations is the same as what has been shown, the narrative will not be continued. However, the sequential derivation, in equation form will be seen.

Mechanism 3

Step 1 $CO + 1 \rightleftarrows CO1$ A2.36

Step 2 $CO1 + CO \leftrightarrows C_2O_2{*}1$ A2.37

Step 3 $C_2O_2{*}1 \rightleftarrows CO_2 + C_1$ A2.38

$C_2O_2{*}1$ in an adsorbed activated complex.

Assume that step 1 is the rate determining step. The equilibrium relationships that will be used are as follows:

From step 3 $\{C_2O_2{*}1\} = K_3\{CO_2\}\{C_1\}$ A2.39

From step 2 $K_2 = \dfrac{\{C_2O_2{*}1\}}{\{CO1\}\{CO\}} = \dfrac{K_2\{CO\}\{C_1\}}{\{CO1\}\{CO\}}$ A2.40

The rate expression is shown in equation A2.42 where $K_1 = k_2/k_1$, and k_2 and k_1 are defined as before.

$$r = k_1\left(\{CO\}\{1\} - \frac{K_3\{CO_2\}\{C_1\}}{K_1K_2\{CO\}}\right) \qquad \text{A2.41}$$

$$T = \{l\} + \{COl\} + \{C_2O_2{*}l\} + \{C_1\} \tag{A2.42}$$

$$T = \{l\} + \frac{K_3\{CO_2\}\{C_1\}}{K_2\{CO\}} + K_3\{CO_2\}\{C_1\} + \{C_1\} \tag{A2.43}$$

$$\phi_c = \frac{T - \{C_1\}}{T} \tag{A2.44}$$

$$\{l\} = \phi_c T - \frac{K_3\{CO_2\}\{C_1\}}{K_2\{CO\}} - K_3\{CO_2\}\{C_1\} \tag{A2.45}$$

$$r = k_1 \left(\phi_c T - \frac{K_3\{CO_2\}\{C_1\}}{K_2\{CO\}} - K_3\{CO_2\}\{C_1\}\right)\{CO\} - \frac{k_1 K_3\{CO_2\}\{C_1\}}{K_1\ K_2\{CO\}} \tag{A2.46}$$

If $\{CO_2\} \simeq 0$

$$r = k_1\{CO\}T\phi_c \tag{A2.47}$$

If $\{CO\} \simeq$ constant then the rate expression has the form

$$r = X\phi_c \tag{A2.48}$$

where $X = k_1\{CO\}T \simeq$ constat

Now consider step 2 to be the rate determining step in mechanism 3. The equilibrium expressions needed can be seen in equations A2.49 and A2.50.

From step 1 $\quad \{COl\} = K_1\{CO\}\{l\}$ A2.49

From step 3 $\quad \{C_2O_2{*}l\} = K_3\{CO_2\}\{C_1\}$ A2.50

$$r = k_1 \left(\{COl\}\{CO\} - \frac{\{C_2O_2{*}l\}}{K_2}\right) \tag{A2.51}$$

where $K_2 = k_2/k_1$

$$r = k_1 \left(K_1\{CO\}^2\{1\} - \frac{K_3\{CO_2\}\{C_1\}}{K_2} \right) \qquad A2.52$$

$$T = \{1\} + \{CO1\} + \{C_2O_2{*}1\} + \{C_1\} \qquad A2.53$$

$$T = \{1\} + K_1\{CO\}\{1\} + K_3\{CO_2\}\{C_1\} + \{C_1\} \qquad A2.54$$

$$\{1\} = \frac{(T - \{C_1\}) - K_3\{CO_2\}\{C_1\}}{1 + K_1\{CO\}} \qquad A2.55$$

$$\{1\} = \frac{\phi_c T - K_3\{CO_2\}\{C_1\}}{1 + K_1\{CO\}} \qquad A2.56$$

$$r = k_1K_1\{CO\}^2 \left(\frac{\phi_c T - K_3\{CO_2\}\{C_1\}}{1 + K_1\{CO\}} \right) - \frac{k_1K_3\{CO_2\}\{C_1\}}{K_2} \qquad A2.57$$

If $\{CO_2\} \simeq 0$

$$r = \frac{k_1K_1\{CO\}^2\phi_c T}{1 + K_1\{CO\}} \qquad A2.58$$

If $\{CO\} \simeq$ constant

$$r = X\phi_c \qquad A2.59$$

where $X = \dfrac{k_1K_1\{CO\}^2T}{1 + K_1\{CO\}} \simeq$ constant

Finally consider step 3 of mechanism 3 to be the rate controlling step. The pertinent equilibrium relationships for this assumption can be seen in equation A2.60 and A2.61.

From step 1 $\quad CO1 = K_1\ CO\ 1 \qquad$ A2.60

From step 2 $$K_2 = \frac{\{C_2O_2{*}1\}}{\{CO1\}\{CO\}} = \frac{\{C_2O_2{*}1\}}{K_1\{CO\}^2\{1\}} \qquad \text{A2.61}$$

$$r = k_1\left(\{C_2O_2{*}1\} - \frac{\{CO_2\}\{C_1\}}{K_3}\right) \qquad \text{A2.62}$$

where $K_3 = k_2/k_1$

$$r = k_1\left(K_2K_1\{CO\}^2\{1\} - \frac{\{CO_2\}\{C_1\}}{K_3}\right) \qquad \text{A2.63}$$

$$T = \{1\} + \{CO1\} + \{C_2O_2{*}1\} + \{C_1\} \qquad \text{A2.64}$$

$$T = \{1\} + K_1\{CO\}\{1\} + K_2K_1\{CO\}^2\{1\} + \{C_1\} \qquad \text{A2.65}$$

$$\{1\} = \frac{T - \{C_1\}}{(1 + K_2K_1\{CO\}^2 + K_1\{CO\})} \qquad \text{A2.66}$$

$$\phi_c = \frac{T - \{C_1\}}{T} \qquad \text{A2.67}$$

$$r = \frac{k_1K_2K_1\{CO\}^2\phi_cT}{1 + K_2K_1\{CO\}^2 + K_1\{CO\}} - \frac{k_1\{CO_2\}\{C_1\}}{K_3} \qquad \text{A2.68}$$

If $\{CO_2\} \simeq 0$ and $\{CO\} \simeq$ constant

$$r = X\phi_c \qquad \text{A2.69}$$

where $$X = \frac{k_1K_2K_1\{CO\}^2T}{1 + K_2K_1\{CO\}^2 + K_1\{CO\}} \qquad \text{constant}$$

Mechanism 4 is the last proposed mechanism to be considered. The derivation of the rate equations from this mechanism will be outlined similar to those of mechanism 3.

Mechansim 4

Step 1 $CO + 1 \rightleftarrows CO1$ A2.70

Step 2 $CO1 + CO \rightleftarrows CO_2 + C_1$ A2.71

Consider step 1 to be the rate determining step. The equilibrium equation that pertains to this derivation can be seen in equation A2.72.

From step 2 $$K_2 = \frac{\{C_1\}\{CO_2\}}{\{CO1\}\{CO\}} \qquad A2.72$$

$$r = k_1\left(\{CO\}\{1\} - \frac{\{CO1\}}{K_1}\right) \qquad A2.73$$

where $K_1 = k_2/k_1$

$$r = k_1\left(\{CO\}\{1\} - \frac{\{CO_2\}\{C_1\}}{K_2K_3\{CO\}}\right) \qquad A2.74$$

$$T = \{1\} + \{CO1\} + \{C_1\} \qquad A2.75$$

$$T = \{1\} + \frac{\{C_1\}\{CO_2\}}{K_2\{CO\}} + \{C_1\} \qquad A2.76$$

$$\{1\} = T - \{C_1\}\left(1 + \frac{\{CO_2\}}{K_2\{CO\}}\right) \qquad A2.77$$

$$\{1\} = (T - \{C_1\}) \left[1 + \frac{\{CO_2\}}{K_2\{CO\}} \right] + \frac{\{CO_2\}}{K_2\{CO\}} \qquad A2.78$$

$$r = k_1\{CO\} \left[\phi_c T \left(1 + \frac{\{CO_2\}}{K_2\{CO\}} \right) + \frac{\{CO_2\}}{K_2\{CO\}} \right] - \qquad A2.79$$

$$\frac{k_1\{CO_2\}\{C_1\}}{K_1 K_2\{CO\}}$$

If $\{CO_2\} \simeq 0$ and $\{CO\} \simeq$ constant

$$r = X\phi_c \qquad A2.80$$

where $X = k_1\{CO\}T \simeq$ constant

Now assume that step 2 of mechanism 4 is the rate determining step. The equilibrium relation for this derivation can be seen in equation A2.81.

From step 1 $\{CO1\} = K_1\{CO\}\{1\}$ A2.81

$$r = k_1 \left[\{CO1\}\{CO\} - \frac{\{CO_2\}\{C_1\}}{K_2} \right] \qquad A2.82$$

where $K_2 = k_2/k_1$

$$r = k_1 \left[K_1\{CO\}^2\{1\} - \frac{\{CO_2\}\{C_1\}}{K_2} \right] \qquad A2.83$$

$$T = \{1\} + \{C_1\} + \{CO1\} \qquad A2.84$$

$$T = \{1\} + \{C_1\} + K_1\{CO\}\{1\} \qquad A2.85$$

$$\{1\} = \frac{T - \{C_1\}}{1 + K_1\{CO\}} \qquad A2.86$$

$$\phi_c = \frac{T - \{C_1\}}{T} \qquad A2.87$$

$$\{1\} = \frac{T\phi_c}{1 + K_1\{CO\}} \qquad A2.88$$

$$r = \frac{k_1K_1\{CO\}^2T\phi_c}{1 + K_1\{CO\}} - \frac{k_1\{CO_2\}\{C_1\}}{K_2} \qquad A2.89$$

If $\{CO_2\} \approx 0$ and $\{CO\} \simeq$ constant

$$r = X\phi_c \qquad A2.90$$

where $X = \dfrac{k_1K_1\{CO\}^2T}{1 + K_1\{CO\}} \simeq$ constant

It should be noted that all of the expressions that were derived in this appendix reduced to the following two forms.

$r = X\phi_c$ and $r = X\phi_c^2$

where $X \simeq$ constant

APPENDIX 3

CALIBRATION OF GAS CHROMATOGRAPH

A Packard model 427 gas chromatograph equipped with a thermal conductivity detector was used to analyze all of the gas samples in this work. The column used for the separation was ¼ inch I.D. and six feet in length, packed with Propack Q with a mesh size between 100 and 120. The temperature used for the separation was a constant 150° C for all parts of the chromatograph. The flow of the carrier gas, helium, was regulated to obtain constant supply pressure of 30 psig to the chromatograph and a constant pressure drop across the columns. The current control for the thermoconductivity detector was set at position 6.

The chromatograph was turned on and allowed to stablize for a few hours at the conditions described above. The instrument was considered stable when the baseline of the output was constant at the lowest attenuation setting. The chart speed used to record the output was 1 cm/min .

Two different calibrations were made. The first covered the entire range of compositions of CO and CO_2. The attenuation was set at 128 for both of the peaks. The second calibration delt with mole fractions of CO_2 from approximately .92 to 1.0, the remainder being CO. For this calibration the attenuation was 128 for the CO peak and changed to 8 for the CO_2 peak. This was done to increase the size of the CO_2 peak so a more accurate determination of the composition could be obtained at high CO mole fractions

The first calibration, covering the entire range of compositions, was carried out by first measuring the volume flow rate of a CO stream using a wet test meter. Next, CO_2 was added to the flowing CO stream and the total volume flow was found using the wet test meter. The mixture of gases was passed through a section of tubing packed with glass beads to ensure that the gases were well mixed. The gases were allowed to flow for at least 15 minutes before the first sample was taken. This allowed the tubing to be purged with the desired mixture. .3ml samples were then taken of the mixture and injected into the chromatograph with the attenuation set at 128. Two peaks were observed. The first peak was found to be CO and the second CO_2. At least three samples were taken for each composition studied.

The heights of the peaks were measured and the fraction of the total height of CO was calculated by dividing the height of the CO peak for each sample by the sum of the heights of the CO and CO_2 peaks for that sample. This was done for all of the samples and the results obtained for the same compositions were averaged. Finally, a plot of the height fraction of CO verses the mole fraction of CO in the mixture was made. See Figure 7.1.

After it was determined that the range of compositions if interest were from approximately .92 to 1 mole fraction

CO, a second calibration was made in this range. This time however, the attenuation was set at 128 for the CO peak and changed to 8 for the CO_2peak. Also, this time the flows of CO and CO_2 were measured using a bubble flowmeter by timing how long it took a bubble to traverse the distance between two etched marks. See Figure 7.7. The volume between the marks was found to be 20.0699 cm^3 by Handa (34). Because of the small amount of CO_2 that was added to the CO stream the bubble flowmeter was used in place of the wet test meter for accuracy.

Because the attenuation was different for the CO and CO_2 peaks, an attenuation factor, which is the number of times the output signal is increased when the attenuation in changed from 128 to 8, had to be determined. An attenuation factor was determined for each of the concentrations studied and the results were averaged to obtain the final attenuation factor that was used. The factors at each composition were found by injecting 3 samples where the attenuation was left on 128 for both peaks, followed by at least 4 samples where the attenuation was changed between the peaks. The attenuation factor was then calculated using the following relationship.

$$\sum_i \frac{\dfrac{h_i}{h_i + k_i}}{i} = \sum_j \frac{\dfrac{h_j}{h_j + \dfrac{l_j}{x}}}{j}$$

where

h_i, h_j = the height of the CO peak in sample i,j Att. = 128
k_i = the height of the CO_2 peak in sample i Att. = 128
l_j = the height of the CO_2 peak in sample j Att. = 8
x = the attenuation factor

The relation was solved by x by using a trial and error method. After attenuation factors were found for each composition, the results were averaged to find the attenuation factor of 16.06. Using this result, the height fraction of CO was found by the following relation.

$$\frac{h_{CO}}{h_{CO} + \frac{h_{CO_2}}{x}} = \text{height fraction of CO}$$

The results obtained for each composition that was studied were averaged as before, and a plot of the height fraction of CO verses the mole fraction of CO in the stream was made. See Figure 7.2.

A summary of the data and calculations used for the calibrations may be seen in Tables A3.1 and A3.2.

Table A3.1

Data from the calibration of the gas chromatograph over the range .92 to .1 mole fraction of CO. (The remainder was CO_2).

Trial	Mole fraction CO	Height fraction CO	Attenuation factor
1	.9516	.9505	16.281
2	.9588	.9611	15.724
3	.9295	.9416	16.317
4	.9384	.9435	16.412
5	.9521	.9556	16.120
6	.9618	.9648	15.970
7	.9674	.9707	16.091
8	.9731	.9764	15.589
9	1.000	1.000	-

Table A3.2

Data from the calibration of the gas chromatograph over the entire range of CO and CO_2 compositions.

Trial	Mole fraction CO	Height fraction CO
1	.6377	.6422
2	.5120	.5337
3	.8611	.8510
4	.9003	.9000
5	.1500	.1913
6	.1932	.2405
7	.4044	.4438
8	.3224	.3668
9	1.000	1.000

APPENDIX 4

BRIEF INSTRUCTIONS TO OBTAIN AN X-RAY DIFFRACTION PATTERN

The equipment that was used for the x-ray diffraction analysis performed in this work was a Seimens Crystalloflex 4, goniometer, table and source. A goniometer is a device that holds the sample and electronic detector, and rotates the detector around the sample at a constant speed, to obtain a diffraction pattern. See Figure A4.1. The table is the equipment that the goniometer and x-ray source are placed on. It has a marble top and is very heavy and stable to reduce vibrations that would affect the diffraction pattern obtained. The table also contains the power supply needed to achieve the voltages required by the x-ray tube to produce x-rays.

Before an x-ray diffraction pattern may be obtained from a sample with this equipment, the sample must be ground or crushed to form a very fine powder. This is usually accomplished using a mortar and pestle. The crushed sample is then lightly packed into a sample holder leaving the surface of the sample that is exposed as smooth as possible. In this work, the sample holder was made of glass and was amorphous to x-rays. Under most conditions, the sample will remain in the holder well enough to be used. If, however, difficulty keeping the sample in the holder occurs, a small amount of binder may be added to the sample. Binders are to be amorphous to x-rays so that they will not interfere with the diffraction pattern obtained from the sample. A common binder is DUCO cement by Dupont. Binder should be used sparingly.

After the sample is in the holder, the holder is placed in the specimen holder on the goniometer. See Figure A4.2. The shield is then carefully lowered around the sample to protect the operator from radiation while running the diffractometer. At no time should the source by on and the port to the goniometer be open without the shield being in place. It should be noted that the radiation emmitted by this equipment can be very dangerous, if it is not operated in a safe manner. Next, that x-ray source may be energized and the electronics usdin in obtaining the the diffraction pattern turned on. This is done by first turning on the cooling water to the equipment and making sure that the pressure supplied to the system is greater then 30 psig. Next, the system is energized by depressing the center button located on the right side of the front of the table. It will take a moment for the equipment to warm up, but when everything is ready the depressed button will glow. If the cooling water has not been turned on or is too low, or if the timer on the front center of the table needs reset, the system will not allow itself to be brought-up.

After the center button is glowing and a check has been made to ensure that all the ports on the x-ray source are closed, the button labeled is depressed. When this is performed a red sign is illuminated above the buttons reading "HIGH TENSION", indicating that the x-ray tube is energized and x-rays would be emitted through an open port. The x-ray source that was used in this work was copper.

Next, the voltage and current on the x-ray tube, to determine the energy of the x-rays emitted, must by set using the knobs on the front of the table. Care should be used so that the source being used is not operated above its power rating. The copper source used here was rated for 750 W. It is advisable to operate below the maximum power rating to prolong the life of the x-ray tube. The settings used were 40 kV and 18 ma.

Next, a check to ensure that the detector is not positioned at an angle of 0 degrees, because this will damage the detector if the port were opened enabling the detector to see the incident beam. The detector should never be passed through 0 degrees while the source is energized and the port open to the goniometer. When the detector is in a safe location, the port to the goniometer may be opened. At this time high energy x-rays are being emitted from the source onto the sample.

The next step is to set the electronics connected with the detector such that the best diffraction pattern is obtained. This is most readily accomplished using experience and experimentation. The first device that must be set dealing with the electronincs is the voltage applied to the detector. This should never by higher than 1600 V or damage to the detector could result. Usually 1200 V is acceptable. The voltage supplied to the detector is raised to increase its ability to detect lower energy radiation and is raised if only higher energy radiation is to be detected. The detector also tends to pick up more backround radiation signals at higher voltages thereby increasing the noise seen in the diffraction pattern. So there is a balance between detecting lower energy radiation and the amount of stray backround radiation that is detected.

The remaining devices that must be adjusted to obtain a diffraction pattern are as follows:

The time constant
The linear pulse rate range control
The potentiometer for channel width adjustment
Integral or differential switch
Gain
Base line
Logarithmic or linear pulse rate switch
Zero point suppression for the linear range

The ratemeter that is used to measure the radiation observed by the detector can output the results on either a linear or logarithmic scale. The linear scale us usually used for x-ray diffraction studies, therefore the logarithmic-linear switch is set to linear. Also the electronics used is equipped with a pulse-height analyser which enables it to count only the radiation pulses above a specified energy (integral) or radiation within a range of enrgies (differential). Sharper diffraction patterns are usually obtained when the pulse-height analyser is used in the differential form. This is done by ensuring the toggle switch is toward the lable "diff". Of course if the integral mode was desired the switch would be positioned toward "integral".

The values for the baseline and channel width for the integral mode of operation are best determined with the aid of the pulse spectroscope. The pulse spectroscope displays the pulse spectrum or the energies of the radiation that is being detected on a display screen. The different energies of radiation detected are displayed by a lighted line or streak on the screen. The energies that are to be counted are shown on the screen by a dark section along the bottom of the screen in which the lighted lines will not pass through. From experience, the best procedure to set the baseline and the width is to locate an angle in which a diffraction line is known to occur, position the detector there and observe the area on the screen in which the illuminated lines increase in number. Then position the darkened box below only that area of the screen by adjusting the baseline and the width. The only pulses that are counted by the counter are those that strike this dark box. The remainder is ignored. The baseline and width may have to be reset after the remainder of the controls are set. The best results can only be obtained through experience and patience.

The linear pulse rate range control, time constant adjustment for the linear range and the control for the gain factor must now be set in a combination that will yield the best results. The linear pulse rate range control determines the rate of detection of radiation in impulse per second, that is needed for a full scale deflection. Therefore, the higher this is set, the larger the amount of radiation that will be required to reach full scale. The time constant control determines the time constant that is used in the RCL circuit used to measure the radiation. If the time constant is low, almost all of the rapid fluctuations in the radiation striking the detector is seen on the recorder, causing the output signal to be very eratic. If the time constant is high, rapid fluctuations are damped out but trends will be recorded and noise is reduced.

The linear pulse range control, and the gain are set so that the peaks obtained in the diffraction pattern cause a deflection on the recorder of the correct size. If the peaks go off scale the pulse range control should be increased or the gain decreased. There is a trade off between the pulse range and the gain. One would not want the pulse rate very low accompanied by a high gain because any noise is amplified along with the wanted pattern. However, one would also not want the pulse rate high because this would make the peaks in the diffraction pattern smaller, which could cause the smaller diffraction peaks to be suppressed, and therefore missed.

The time constant will affect the diffraction pattern in much the same way as the linear pulse range control and the gain. If the time constant is low, alot of noise will be seen on the output. However, if the time constant is large, small peaks could be damped out and the position of all of the peaks could be shifted. The shift in the angle of the diffracted peaks occurs because the high time constant causes the rise of the peak to be suppressed in the beginning, and after the peak has attained its maximum height, the high time constant keeps the output signal high until after the angle in which the maximum occurred has passed. The value of the time constant also depends on the sweep speed of the detector through the angles of interest. The slower the sweep speed, the higher the time constant may be before it starts to markedly affect the smaller peaks and the position of the other larger peaks.

Of course, the control for the zero point suppression in the linear range affects the baseline that is seen on the output. If the zero is increased 10%, the output will decrease 10 divisions (10% of the span).

After the controls for the electronics have been set, the detector is moved to the desired starting angle by rotating the knob in the right side of the goniometer. Next, the gears needed to obtain the proper sweep speed are placed on the drive, and the drive gear pushed in so that the two gears mesh together. It is usually wise to adjust the strip chart speed so that it corresponds to the sweep speed of the detector, which will make it easier to determine the angles at which the diffraction

Figure A4.1. X-ray Diffraction Equipment. (41)

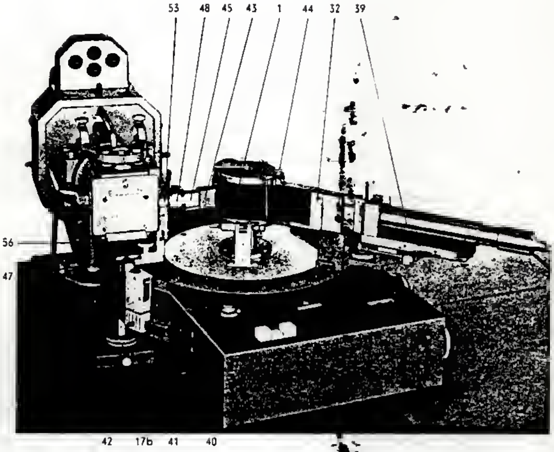

1	Radiation-protection cap
17b	Short guide rail
32	Scattered-radiation shield of the detector carrier
39	Geiger-Mullar counter tube
40	Sockets for the connection of the angle-mark transmitter
41	Opening for readjustment of worm shaft
42	Adjusting carriage
43	Nose on the radiation protection cap
44	Knurled-head screw for the attachment of the radiation protection cap
45	Scattered-radiation shield of aperture diaphragm
47	Aperture-diaphragm base
48	Aperture diaphragm
53	Radiation-protection clip
56	Knurled-head screw for the adjustment of the aperture diaphragm

Fig. 6 Diffractometer arranged at horizontal tube stand 4

Figure A4.2. The X-ray Diffraction Specimen holder. (41)

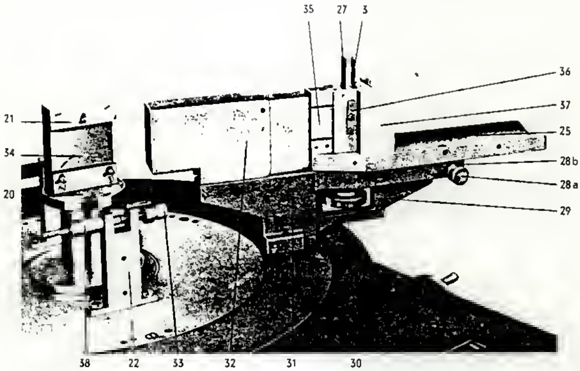

3	Filter slide with Kβ-filters
20	Specimen carrier
21	Specimen holder
22	Adjusting stand
25	Detector-carrier plate
27	Detector diaphragm
28a	Adjusting screw for detector-carrier plate (25)
28b	Lock nut
29	Detector-carrier base
30	Knurled nut
31	Detector carrier
32	Scattered-radiation shield of detector carrier
33	Adjusting screw on adjusting stand for specimen carrier (20)
34	Specimen
35	Soller diaphragm
36	Pressure spring
37	Detector holder
38	Counter-pressure spring

Table A4.1

Typical values of the x-ray diffraction equipment

Time constant	4
Gain	8
Linear/logarithmic display	linear
Potentiometer for channel width	2.43
Baseline	5.15
Integral/differential switch	integral
Linear pulse rate range	400 imp/sec
Sweep Speed	1° (2θ)/min
Chart speed	1 cm/min
Detector voltage	1200 V
Zero	40%

peaks occured.

After the speed of the chart recorder has been set, both the chart recorder and the sweep of the detector should be started at the same time. The sweep of the detector is started by depressing the button below the arrow which is pointing in the desired direction. It is advisable to always sweep through the angles of interest from the same direction. That is, from low angles to higher angles, or vise versa. Doing this reduces the possibility of play in the gears of the goniometer affecting the diffraction pattern. Care should also be taken to ensure that the detector is not allowed to strike the x-ray source. This could cause extensive damage to the detector and the source, as well as pose a possible health threat to anyone nearby.

It should be evident by now that these instructions are to serve only as a guide to operating the x-ray diffraction equipment. The best results are obtained by consulting texts books on the matter to aid in the understanding the phenomena that is occuring. Two such texts are referenced in the bibliography (38,39).

Typical values for the contols that were used to obtain the diffraction patterns in this work can be seen in Table A4.1.

It should be noted that a nickel filter was used to make the radiation seen by the detector nearly monochromatic. Also the slit sizes that were used were .1 mm near the detector and .8 on the variable shutter near the source.

APPENDIX 5

Sample calculations, Tabulated data and Computer programs.

SAMPLE CALCULATIONS

Data from run R39 will be used for the sample calculations.

Time of sample .11667 hours

Height measured from G C charts for CO. 103.1 mm

Height measured from G C charts for CO_2. 9.2 mm

Calculation of mole fractions of CO and CO_2

$$\text{Height fraction CO} = \frac{103.1}{103.1 + \dfrac{9.2}{16.064}} = .99447$$

Convert the height fraction to mole fraction.

$$\text{Mole fraction CO} = \frac{.99447 - .085022}{.914984} = .99395$$

Mole fraction CO from blank at 600° C. = .99773

Corrected mole fraction = .99395 + (1 - .99773) = .99623

Calculation of the rate of reaction of CO

The molar flow rate into the reactor = 6.571×10^{-6} mol/sec

Mass of catalyst in the reactor = .24 g

Pure CO was used for the reactant stream.

$$r = \frac{6.571 \times 10^{-6}}{.24} \left(1 - \frac{.99623(2-1)}{2 - .99623} \right) = 20.57 \times 10^{-7} \text{ mol/g sec}$$

Table A5.1

Mole fractions of CO that were obtained from the exit stream during a blank run

T	Mole fraction CO
500	.99838
550	.99812
600	.99773

The following data is printed for the different experiments that were discussed in this work. The data points are the average of the multiple samples that were taken for each particular sample time.

DATA FROM EXPERIMENT R35

MOLAR FLOW RATE 6.831E-06 MOLE/SEC
MASS OF CATALYST .2376 GRAMS

SAMPLE NUMBER	TIME HRS	HEIGHT FRACT CO (MM)	HEIGHT FRACT CO2 (MM)	MOLE FRACT CO	RATE (MOL/S G)
2	.25	190	33.7	.99029	5.528E-08
3	.5	213.1	27	.99371	3.594E-08
4	.75	214.1	26.2	.99397	3.444E-08
5	1	215	26.3	.99397	3.445E-08
6	1.25	214	26.2	.99396	3.449E-08
7	2	215.1	26.7	.99388	3.496E-08
8	2.5	212.3	25	.99431	3.251E-08
9	3	216.1	25.1	.99442	3.19E-08
10	3.51	214.1	25	.99437	3.215E-08
11	4.25	214.1	24.8	.99441	3.195E-08
12	6.69	213.1	24.1	.99462	3.075E-08
13	8.83	215.3	24	.99473	3.011E-08
14	11.86	215.6	23	.99505	2.828E-08
15	13.91	216	21.6	.9955	2.575E-08
16	23.46	216.3	19.8	.99604	2.266E-08
17	31.6	216	19	.99631	2.113E-08
18	47.36	215.8	20.5	.99583	2.383E-08
19	59.38	214.1	18.2	.99648	2.016E-08
20	70.51	214	20.5	.99578	2.413E-08
21	77.66	212	24.1	.99458	3.098E-08
22	77.71	213.6	25	.99435	3.226E-08
23	82.93	211.8	25.2	.99422	3.3E-08
24	95.23	213	23.5	.9948	2.97E-08
25	101.68	213.8	21.8	.99533	2.668E-08
26	110.86	215.8	20.7	.99574	2.434E-08
27	117.46	216.1	19.5	.99616	2.199E-08

DATA FROM EXPERIMENT R36

MOLAR FLOW RATE 7.693E-06 MOLE/SEC
MASS OF CATALYST .3188 GRAMS

SAMPLE NUMBER	TIME HRS	HEIGHT FRACT CO (MM)	HEIGHT FRACT CO2 (MM)	MOLE FRACT CO	RATE (MOL/S G)
4	.15	126.6	24	.98887	5.309E-08
5	.2	175.1	26	.9916	4.018E-08
6	.25	200	21	.99451	2.632E-08
7	.3	209	21	.99482	2.487E-08
8	.4	213.6	21.5	.9948	2.492E-08
9	.48	212.3	21.2	.99483	2.482E-08
10	.64	213	21.6	.99475	2.517E-08
11	.86	213	21	.99494	2.426E-08
12	1	214	21.5	.99482	2.486E-08
13	1.29	213.8	21.5	.99481	2.489E-08
14	1.86	213.1	20	.99526	2.274E-08
15	2.18	214.5	21.5	.99483	2.479E-08
16	6.34	213.1	19	.99558	2.122E-08
17	12.91	217.6	17.6	.99614	1.855E-08
18	17.63	217	16.8	.99634	1.759E-08
19	20.76	214.6	17.7	.99603	1.908E-08
20	22.78	216	17.5	.99612	1.861E-08
21	26.21	215.8	18	.99596	1.938E-08
22	30.98	213.5	16.5	.99638	1.74E-08
23	42.08	216.1	16.7	.99638	1.739E-08
24	51.58	216.6	17.7	.99605	1.897E-08
25	57.71	216.1	19	.99566	2.082E-08
26	69.81	215.3	17.2	.99617	1.839E-08
27	76.26	211.8	17	.99618	1.836E-08
28	80.94	213.1	17	.99621	1.82E-08
29	89.59	215.8	18.2	.99587	1.981E-08
30	92.09	216	17.5	.99612	1.861E-08
31	98.46	211	19	.99552	2.151E-08
32	102.48	215	19	.99563	2.098E-08
33	113.76	215.1	15.5	.99673	1.571E-08
34	116.28	218	16.7	.99639	1.733E-08
35	118.51	215.8	16.7	.99634	1.758E-08
36	122.48	216	15.3	.99678	1.546E-08
37	127.76	215.7	14.6	.99699	1.445E-08
38	132.44	218	13.4	.99742	1.238E-08
39	137.64	219.3	13.3	.9975	1.201E-08
40	141.14	217.2	12.3	.99774	1.086E-08
41	145.23	217.3	12.2	.99779	1.06E-08
42	150.81	218.1	12.4	.99774	1.088E-08
43	162.31	216.7	14.2	.99715	1.367E-08

DATA FROM EXPERIMENT R37

MOLAR FLOW RATE 6.01E-06 MOLE/SEC
MASS OF CATALYST .3095 GRAMS

SAMPLE NUMBER	TIME HRS	HEIGHT FRACT CO (MM)	HEIGHT FRACT CO2 (MM)	MOLE FRACT CO	RATE (MOL/S G)
1	.5	214.3	25.5	.99383	2.379E-08
2	1	216	25.8	.99379	2.394E-08
3	2.16	215.7	26.2	.99365	2.45E-08
4	3.41	215.4	26.3	.99359	2.47E-08
5	5.46	217.3	26.1	.99374	2.412E-08
6	12.85	217.6	25.8	.99383	2.38E-08
7	15.33	216.1	25	.99405	2.293E-08
8	17.41	216.6	24.8	.99412	2.267E-08
9	19.08	215.9	23.6	.99446	2.137E-08
10	20.83	216.2	23.1	.99464	2.07E-08
11	28.58	216.6	20.6	.99541	1.771E-08
12	36.58	217.8	19.7	.99571	1.655E-08
13	42.79	215.6	19.9	.99561	1.694E-08
14	46.93	216	19.6	.99573	1.65E-08
15	49	214.9	19	.99588	1.589E-08
16	51.43	215.2	18.8	.99592	1.574E-08
17	60.91	217.2	19.6	.99575	1.641E-08
18	65.33	212.6	18.6	.99592	1.574E-08
19	69.36	214.3	18.1	.99613	1.495E-08
20	74.83	214.9	18.5	.99604	1.529E-08
21	84.83	212.9	19.3	.99571	1.655E-08
22	87.66	215.1	19.2	.99582	1.615E-08
23	90.41	215.4	19.2	.99584	1.608E-08
24	93.19	215.2	19.2	.99583	1.61E-08
25	98.53	215.8	20.2	.99552	1.728E-08
26	109.58	212.8	21.1	.99515	1.871E-08
27	112	213.3	21.3	.99508	1.898E-08
28	114.66	213.1	22.9	.99459	2.089E-08
29	115.66	212.8	23.7	.99433	2.186E-08
30	116.83	213.1	24.6	.99407	2.286E-08
31	119.58	213.8	25.3	.99386	2.366E-08
32	122.5	213	26.3	.99352	2.498E-08
33	126.25	213.7	27.8	.99306	2.676E-08
34	131.33	214.6	28.3	.99296	2.712E-08
35	134	212.2	27.7	.99306	2.675E-08
36	135.63	214.6	27.9	.99308	2.666E-08

Data From Experiment P37 Cont.

SAMPLE NUMBER	TIME HRS	HEIGHT FRACT CO (MM)	HEIGHT FRACT CO2 (MM)	MOLE FRACT CO	RATE (MOL/S G)
37	137.83	214	28	.99302	2.691E-08
38	140.66	211.7	29.7	.99239	2.931E-08
39	144.19	213	28.1	.99294	2.719E-08
40	147.93	213.3	29	.99269	2.815E-08
41	152.16	213.6	25.1	.99391	2.348E-08
42	156.91	213.4	24.9	.99398	2.323E-08
43	160.5	213.1	26.3	.9935	2.505E-08
44	163.33	212.3	26.2	.9935	2.504E-08
45	164.83	211.8	26.4	.99344	2.528E-08
46	168.14	211.8	25.2	.99381	2.387E-08
47	170.86	211.9	25.1	.99385	2.373E-08
48	180.83	212	25.4	.99375	2.408E-08
49	184.5	211.4	26.4	.99343	2.534E-08
50	186.25	213.6	24.2	.99418	2.243E-08
51	189.6	213.4	24.8	.99399	2.319E-08
52	192.83	212.7	24.8	.99397	2.325E-08
53	206.08	213.3	24.4	.99412	2.268E-08
54	208.5	213.8	25.1	.99393	2.342E-08
55	213.16	212.2	25	.99391	2.348E-08
56	218.66	212.5	25	.99391	2.349E-08
57	230.66	211.3	23	.99449	2.125E-08
58	235.83	212.1	23.4	.99439	2.164E-08
59	241.16	211.4	23.8	.99425	2.217E-08
60	252.83	210.1	22.7	.99455	2.102E-08

DATA FROM EXPERIMENT R39

MOLAR FLOW RATE 6.571E-06 MOLE/SEC
MASS OF CATALYST .24 GRAMS

SAMPLE NUMBER	TIME HRS	HEIGHT FRACT CO (MM)	HEIGHT FRACT CO2 (MM)	MOLE FRACT CO	RATE (MOL/S G)
1	.11	103.1	9.1	.99623	2.055E-08
2	.2	150	56	.97744	1.208E-07
3	.34	207	28	.99313	3.732E-08
4	.51	211.8	24.1	.99457	2.954E-08
5	.78	212.3	24.5	.99446	3.012E-08
6	1	213	25	.99433	3.084E-08
7	1.5	211.8	25	.99428	3.112E-08
8	3.08	212.5	26	.99399	3.27E-08
9	7.16	213.8	25.7	.99411	3.202E-08
10	9.8	213	24.9	.99434	3.077E-08
11	13.61	213.6	23.2	.99491	2.769E-08
12	17.83	214.1	22	.9953	2.557E-08
13	20.5	213.4	21.6	.99542	2.495E-08
14	24.16	214.2	21	.99561	2.391E-08
15	26.41	214.1	19.5	.9961	2.125E-08
16	29.78	213.6	17.6	.99666	1.819E-08
17	41.78	210.1	18	.99645	1.933E-08
18	44.16	211.4	19.7	.99595	2.207E-08
19	45.41	210.1	20.9	.99552	2.438E-08
20	46.83	212.1	21	.99555	2.42E-08
21	48.25	211.5	21.6	.99535	2.533E-08
22	50.41	211	22.3	.99511	2.664E-08
23	52.58	208.6	20.9	.99547	2.464E-08
24	55.66	211.8	21.4	.99541	2.5E-08
25	58.16	209.1	19.5	.99594	2.211E-08
26	65.83	222.1	17.6	.99689	1.693E-08
27	67.41	220.5	18.7	.99649	1.913E-08
28	69.25	217	18.9	.99634	1.991E-08
29	70.83	213.6	21	.99559	2.401E-08
30	72.83	212.5	21.1	.99554	2.431E-08
31	74	212	20.2	.9958	2.285E-08
32	76	213.3	19.8	.99596	2.201E-08
33	77.11	209.3	19.3	.99599	2.183E-08
34	78.25	210.8	18.3	.99638	1.974E-08
35	80.75	214.1	19.7	.99604	2.159E-08
36	87.66	213.4	19.8	.99597	2.193E-08

Data From Experiment P39 Cont.

SAMPLE NUMBER	TIME HRS	HEIGHT FRACT CO (MM)	HEIGHT FRACT CO2 (MM)	MOLE FRACT CO	RATE (MOL/S G)
37	91.08	211.9	20	.99585	2.258E-08
38	94.5	212.8	20	.9959	2.231E-08
39	96.58	212.3	20	.99587	2.252E-08
40	99.16	213	19.9	.99592	2.223E-08
41	101.91	212	20.1	.99585	2.261E-08
42	104.63	212.3	21.2	.9955	2.451E-08
43	108.88	213.3	21.8	.99533	2.542E-08
44	113.25	212.5	20.9	.9956	2.397E-08
45	117.41	211.6	20.6	.99565	2.366E-08
46	119.83	211.6	20.5	.99571	2.337E-08
47	122.08	212.7	20	.99588	2.245E-08
48	124.5	211.3	19.6	.99598	2.187E-08
49	127.5	212	18.7	.99628	2.026E-08
50	137.66	211.1	17.6	.9966	1.85E-08
51	145.16	210.1	18	.99646	1.928E-08
52	147.08	210.8	18.8	.99621	2.067E-08
53	153.08	211.6	18.8	.99622	2.061E-08
54	161.83	211.1	17.6	.99662	1.843E-08

DATA FROM EXPERIMENT R40

MOLAR FLOW RATE 6.358E-06 MOLE/SEC
MASS OF CATALYST .2489 GRAMS

SAMPLE NUMBER	TIME HRS	HEIGHT FRACT CO (MM)	HEIGHT FRACT CO2 (MM)	MOLE FRACT CO	RATE (MOL/S G)
1	.16	104.8	3.2	.99791	1.06E-08
2	.25	108.3	33	.97964	1.019E-07
3	.33	156.3	40	.98286	8.606E-08
4	.5	207.1	17	.99443	2.825E-08
5	.58	210	14.5	.99531	2.382E-08
6	.66	211.1	13.5	.99565	2.207E-08
7	2.08	214	10	.9968	1.628E-08
8	4.55	213	10.3	.99668	1.689E-08
9	11.5	213.9	10.3	.99672	1.666E-08
10	14.91	213.8	10.5	.99664	1.707E-08
11	18.33	213.8	10.3	.99669	1.683E-08
12	20.33	212.6	10.1	.99675	1.652E-08
13	22.96	212.6	10.2	.99672	1.668E-08
14	25.75	212.8	10.3	.99669	1.683E-08
15	28.41	213.1	11	.99649	1.785E-08
16	32.66	212.6	11	.99646	1.797E-08
17	37.03	212.1	10	.99677	1.64E-08
18	41.21	212.6	10.3	.9967	1.676E-08
19	43.61	214.1	10.8	.99654	1.76E-08
20	45.91	213.8	10.6	.99663	1.715E-08
21	48.29	212.8	10.1	.99675	1.651E-08
22	51.25	212.3	10.1	.99675	1.654E-08
23	61.5	213.3	9.8	.99686	1.598E-08
24	68.91	211.8	11	.99647	1.796E-08
25	70.91	211.8	10.8	.9965	1.779E-08
26	76.91	212.5	10.3	.99668	1.685E-08
27	85.66	212.9	9.8	.99687	1.593E-08
28	88.75	212.6	10.6	.99661	1.725E-08
29	91.75	211.5	10.8	.99653	1.766E-08
30	94.16	212	10.5	.99663	1.713E-08
31	98.08	212.7	9.9	.99682	1.619E-08
32	112.08	210.1	11.1	.99637	1.843E-08

Data From Experiment R40 Cont.

SAMPLE NUMBER	TIME HRS	HEIGHT FRACT CO (MM)	HEIGHT FRACT CO2 (MM)	MOLE FRACT CO	RATE (MOL/S G)
33	117.66	209.6	12	.99611	1.977E-08
34	120.08	209	12	.9961	1.983E-08
35	124.91	209.1	11.2	.99634	1.86E-08
36	133.66	208.5	12	.99609	1.989E-08
37	137.35	209	13.3	.99568	2.197E-08
38	141.3	208.4	12.9	.99578	2.145E-08
39	146.25	210.6	12.5	.99596	2.05E-08
40	149	212.6	12.6	.99594	2.063E-08
41	159.33	211.3	12.1	.99611	1.978E-08
42	161.38	209.8	13	.99579	2.139E-08
43	164.63	211.3	13	.9958	2.133E-08
44	167.83	211.1	13.1	.99575	2.158E-08
45	173.08	209.1	12.6	.99589	2.089E-08
46	183	210	12.3	.99599	2.039E-08
47	185.83	210.8	13.3	.99568	2.194E-08
48	191.66	211.5	13.1	.99577	2.147E-08
49	196.58	210.5	12.1	.99609	1.986E-08
50	207.41	212.7	10.9	.9965	1.78E-08
51	218.25	210.4	11	.99644	1.807E-08
52	228.66	211.1	10.8	.99649	1.786E-08
53	236.16	208.9	12	.99607	1.995E-08

DATA FROM EXPERIMENT R43

MOLAR FLOW RATE 6.501E-06 MOLE/SEC
MASS OF CATALYST .2546 GRAMS

SAMPLE NUMBER	TIME HRS	HEIGHT FRACT CO (MM)	HEIGHT FRACT CO2 (MM)	MOLE FRACT CO	RATE (MOL/S G)
1	.16	122.9	45.5	.97694	1.109E-07
2	.21	150.8	38	.98473	7.398E-08
3	.28	194.1	19	.99499	2.45E-08
4	.36	206.1	23	.99407	2.897E-08
5	.53	208.8	19.1	.99542	2.24E-08
6	.71	210	17.2	.99603	1.942E-08
7	1.28	209.3	15	.99675	1.593E-08
8	1.78	210.7	14.9	.99681	1.562E-08
9	2.28	210.3	14.3	.99698	1.478E-08
10	5.03	211.8	13.3	.99732	1.311E-08
11	8.11	210.3	12.7	.99751	1.221E-08
12	12.44	210.4	12.1	.99768	1.136E-08
13	17.78	209.8	12	.99772	1.116E-08
14	20.78	209.9	12.9	.99742	1.262E-08
15	23.7	207.8	13.2	.99728	1.33E-08
16	25.95	207.3	13.5	.99719	1.377E-08
17	29.45	207.8	12	.99768	1.134E-08
18	32.78	206.8	11.8	.99771	1.122E-08
19	41.7	205.5	12	.99763	1.161E-08
20	45.28	205.9	12.7	.99742	1.264E-08
21	49.86	206.2	13.1	.99728	1.33E-08
22	53.36	205.3	13.1	.99726	1.34E-08
23	59.03	208.3	13.6	.99718	1.382E-08
24	65.78	206.6	12.8	.99738	1.284E-08
25	68.69	206.7	13.8	.99706	1.437E-08
26	71.69	206.3	13.8	.99708	1.431E-08
27	74.19	207.3	14.7	.99679	1.573E-08
28	77.81	206.5	14.5	.99685	1.541E-08
29	81.03	206.6	13.7	.99711	1.417E-08
30	89.69	205.1	12.3	.99753	1.207E-08
31	92.19	206.4	13.6	.99715	1.398E-08
32	94.78	205.2	13.7	.99708	1.432E-08
33	99.44	206.1	13.7	.99708	1.427E-08
34	106.86	207.5	12	.99768	1.137E-08
35	116.28	207.1	12.4	.99753	1.21E-08
36	120.28	206.6	12.1	.99761	1.172E-08
37	124.8	207.5	12.3	.99757	1.188E-08
38	137.19	207.1	11.6	.99778	1.088E-08
39	146.53	203.9	11.6	.99772	1.117E-08
40	154.03	202.8	11.2	.99785	1.053E-08
41	164.69	206.2	11.3	.99786	1.046E-08

The following programs were written for a Commodore 64 computer equiped with a Simons Basic cartridge. The First program stores the information to the disk drive and the subsequent programs use this information. The programs are in Basic and will only work correctly if a Simons Basic cartridge is used in the computer.

This program stores the raw data and calculates the mole fractions of CO and CO$_2$ in the exit stream and the rate. It stores the results to disk.

```
10 DIM C(200),C2(200),T(200),HF(200),MF(200),RT(200),J(200)
20 GOSUB 420
22 INPUT "ENTER FIRST SAMPLE NUMBER";J(0)
23 J(0)=J(0)-1
25 I=0:
30 I=I+1
35 PRINT "{C/DN}{C/DN}{C/DN}"
40 INPUT"ENTER POINT NUMBER";J(I)
41 IF J(I)=999 THEN N=I-1:GOTO 82
42 IF J(I)=J(I-1)+1 OR J(I)=J(I-1) THEN GOTO 44
43 GOTO40
44 IF J(I)=J(I-1) THEN T(I)=T(I-1):GOTO 60
50 INPUT"ENTER TIME HRS,MIN";TT,MT%
55 GOSUB 460
60 INPUT "ENTER CO CONC";C(I)
70 INPUT "ENTER CO2 CONC";C2(I)
80 GOTO 30
82 INPUT "DO YOU WISH TO REVIEW THE DATA";AN$
84 IF AN$="Y" THEN GOSUB 600
85 IF AN$="N" THEN GOTO 90
86 GOTO 82
90 REM CALC HEIGHT FRACTION
95 REM CALC HEIGHT FRACTION
100 FOR I=1 TO N
110 HF(I)=C(I)/(C(I)+C2(I)/16.064)
120 NEXT I
130 REM CALC MOLE FRACTIONS
135 INPUT "ENTER BLANK CONC OF CO";XX
140 FOR I=1 TO N
150 MF(I)=(HF(I)-.0850222579)/.9149839376
155 MF(I)=MF(I)+(1-XX)
160 NEXT I
170 INPUT "ENTER MASS CAT. G";MC
180 INPUT "ENTER MOLAR FLOW OF GAS";WO
195 HR=0
200 FOR I=1 TO N
205 A=1*MF(I)
210 B=2-MF(I)
212 RT(I)=WO*(1-A/B)/MC
215 IF RT(I)>HR THEN HR=RT(I)
220 NEXT I
230 HIRES 0,1
260 FOR I=1 TO N
270 X=(T(I)/T(N))*250
280 Y=(RT(I)/HR)*199
```

```
285 PLOT X,Y,1
290 NEXT I
300 INPUT A$
305 NRM
306 FOR I=1 TO N
307 PRINT J(I),T(I),C(I),C2(I),MF(I),RT(I)
308 INPUT B$
309 NEXT I
310 INPUT "ENTER NUMBER OF RUN";QQ$
312 OPEN 2,8,2,"@0:R"+QQ$+",S,W"
314 PRINT#2,N
316 ZZ$=","
317 FOR I=1 TO N
318 PRINT#2,J(I)ZZ$T(I)ZZ$C(I)ZZ$C2(I)ZZ$MF(I)ZZ$RT(I)
320 NEXT I
330 CLOSE2
350 STOP
420 INPUT "ENTER STARTING TIME HRS.MIN";BT,MS%
430 INPUT "AM OR PM";X$
450 IF X$="PM" OR X$="P" THENBT=BT+12
455 RETURN
460 REM INPUT "ENTER NEXT TIME";TT,MT%
470 INPUT "AM OR PM";M$
480 IF TT=12 AND M$<>"P" THENTT=24:GOTO 510
490 IF M$="P" AND TT<>12 THENTT=TT+12
500 IF M$<>"P" AND X$="P" THENTT=TT+24
510 NS%=INT(BT):NT%=INT(TT)
520 NH%=ABS(NT%-NS%)
530 NM%=(MT%-MS%)
550 SM=NH%*60+NM%+SM
560 PRINT SM;" MIN OR ";SM/60;" HRS"
570 IF M$<>"P" AND X$="P" THENTT=TT-24
580 BT=TT:MS%=MT%:X$=M$
585 T(I)=SM/60
590 RETURN
600 FOR I=1 TO N
610 W3$="    "
620 PRINT J(I);W3$;T(I);W3$;C(I);W3$;C2(I)
630 INPUT "DO YOU WANT TO CHANGE THIS";W2$
640 IF W2$="Y" THEN GOSUB 660
650 NEXT I
655 RETURN
660 INPUT"ENTER POINT NUMBER";J(I)
710 INPUT"ENTER TIME HRS";T(I)
730 INPUT "ENTER CO CONC";C(I)
740 INPUT "ENTER CO2 CONC";C2(I)
750 RETURN
```

This program averages the data taken at a particular time and stores the average on disk.

```
10 INPUT "ENTER FILE TO BE AVERAGED";FL$
15 ZZ$=","
20 OPEN 2,8,2,"0:"+FL$+".S.R"
30 OPEN 3,8,3,"@0:"+FL$+" AVG,S,W"
40 INPUT#2,N
41 N=N+1
42 PRINT#3,N
45 K=1
50 SC=0:SM=0:I=0:S2=0:SR=0
60 IF I=N THEN GOTO 160
70 INPUT#2,J,T,C,C2,MF,RT:I=I+1
80 SC=SC+C:SM=SM+MF:SR=SR+RT:S2=S2+C2
90 IF I=N THEN GO TO 120
100 INPUT#2,JJ,TT,C,C2,MF,RT:I=I+1:PRINT I
110 IF JJ=J THEN K=K+1:GO TO 80
120 AC=SC/K:AM=SM/K:AR=SR/K:A2=S2/K
130 K=1
131 PRINT#3,J
132 PRINT#3,T
133 PRINT#3,AC
134 PRINT#3,A2
135 PRINT#3,AM
136 PRINT#3,AR
145 K=1:SC=0:S2=0:SM=0:SR=0:J=JJ:T=TT
147 IF I=N THEN GOTO 160
150 GO TO 80
160 CLOSE2
170 CLOSE3
180 STOP
```

This program calculates the carbon content of the catalyst.

```
2 INPUT "ENTER FLOW RATE MOL/SEC";FR
3 INPUT "ENTER MASS CAT G";MC
5 DIM J(100),T(100),C(100),C2(100),MF(100),RT(100),IT(100)
10 INPUT "ENTER FILE TO BE INTEGRATED";FL$
20 OPEN 2,8,2,"0:"+FL$+",S,R"
30 INPUT#2,NN
35 I=0
40 LOOP
50 I=I+1
60 INPUT#2,J(I),T(I),C(I),C2(I),MF(I),RT(I)
70 MF(I)=1-MF(I)
80 EXIT IF J(I-1)=J(I)
90 END LOOP
95 CLOSE2
100 I=I-1
110 REM INTEGRATE
130 IT(1)=(T(1)-.10)*3600*MF(1)*FR/MC
140 JJ=2
150 LOOP
160 TR=ABS(MF(JJ)-MF(JJ-1))*3600*.5*(T(JJ)-T(JJ-1))*FR/MC
170 IF MF(JJ)>MF(JJ-1) THEN RE=MF(JJ-1)*(T(JJ)-T(JJ-1))*3600*FR/MC
190 IF MF(JJ-1)>=MF(JJ) THEN RE=MF(JJ)*(T(JJ)-T(JJ-1))*3600*FR/MC
200 IT(JJ)=IT(JJ-1)+RE+TR
210 EXIT IF JJ>=I
220 JJ=JJ+1
230 END LOOP
235 K=1
240 LOOP
250 PRINT J(K),T(K),MF(K),IT(K)
260 K=K+1
270 EXIT IF K>=I
280 END LOOP
290 INPUT "DO YOU WANT TO GO OVER THESE AGAIN";A$
300 IF A$<>"N" THEN GOTO 235
310 INPUT "PRINT Y OR N";B$
320 IF B$="N" THEN STOP
330 OPEN 4,4,4
331 PRINT#4,"RUN ";FL$:PRINT#4,
332 PRINT#4,"FLOW RATE MOL/SEC";FR
333 PRINT#4,"MASS CATALYST";MC
335 K=1
337 LOOP
340 PRINT#4,J(K),T(K),MF(K),IT(K)
345 K=K+1
346 EXIT IF K>=I
347 END LOOP
360 CLOSE4
370 STOP
```

A STUDY OF THE DISPROPORTIONATION OF CARBON MONOXIDE ON ALUMINA

by

Lawrence J. Samson

B. S., Kansas State University, 1982

AN ABSTRACT OF A MASTER'S THESIS

Submitted in partial fulfillment of the

requirements for the degree

MASTER OF SCIENCE

Department of Chemical Engineering

KANSAS STATE UNIVERSITY
Manhattan, Kansas

1985

ABSTRACT

In this work carbon monoxide was found to disproportionate on eta and gamma alumina at temperatures between 450 and 700° C according to the following reaction. $2CO = CO_2 + C$. The rate of disproportionation and how it changed with time were studied using gamma alumina that was prepared by an amalgamation process. The rate was found to decrease initially, followed by a slight increase after which the rate continued to decrease for the remainder of the experiment. The reason for the increase was postulated to be from a phase change of the gamma alumina to theta alumina. However, this was disproved using x-ray diffraction to examine the structure before and after the alumina was used in an experiment. The initial decrease in the rate was then analyzed using a mehtod put forth by Froment and Bischoff dealing with changes in rates of reactions because of coking. Four different mechanisms were postulated for the reaction. Expressions for the rate were derived in the analysis and functions for the activity of the catalyst as a function of the carbon content were found.